University of Modena and Reggio Emilia

Department of Engineering "Enzo Ferrari"

International Doctorate in Information and Communication Technologies

XXXVII Cycle

Comprehensive EMI Filter design in EV On-Board Chargers: Modelling, Simulation, and Compliance with Automotive Standards

Tutor:

Prof. Ing. Luca Vincetti

Co-tutor:

Ing. Daniele Pedroni

Doctorate coordinator:

Prof. Ing. Luigi Rovati

PhD Candidate:

Stefano Righi

Academic Year 2023/2024

Desidero esprimere la mia profonda gratitudine alla mia famiglia e alla mia ragazza, Cristina, il cui amore incondizionato, supporto e incoraggiamento mi hanno accompagnato lungo tutto questo percorso. Senza la loro presenza costante e il loro affetto, questo traguardo non sarebbe stato possibile.

Un ringraziamento speciale va anche alla azienda, Meta System, che ha dimostrato grande supporto durante i miei studi, permettendomi di conciliare il lavoro con il percorso accademico. La fiducia e le opportunità ricevute sono state fondamentali per il raggiungimento di questo risultato.

A tutti voi, grazie di cuore.

Contents

Abstract

Effective management of Electromagnetic Interference (EMI) is crucial in Electric Vehicle (EV) charging systems, particularly for On-Board Chargers (OBCs) interfacing with high-voltage lithium-ion (Li-ion) batteries and the grid. EMI filters play an essential role in suppressing electromagnetic noise generated by switching-mode power supplies (SMPS). Key components of these filters include resistors, common mode chokes (CMCs) and film capacitors, which contribute to achieving low pass filtering behavior. Compliance with original equipment manufacturer (OEM) standards is of paramount importance, as stricter OEM requirements often impose more challenging limits than international norms such as CISPR25 and CISPR16. This necessitates a robust approach during the design and testing phases, to ensure effective electromagnetic noise mitigation. This study presents an overview of a typical OBC structure, detailing the regulations and standards that must be complied with. The focus then shifts to CMC, where a complex broadband model of this component has been developed. This model integrates various impedances: common mode impedance (Z_{CM}), differential mode impedance (Z_{DM}), inter-

winding impedance (Z_{IW}), and phase impedance (Z_{PH}). Data obtained from Vector Network Analyzer (VNA) and impedance analyzer measurements enable a comprehensive evaluation of CMC behavior and their models. The performance of an HVDC filter designed for a 22kW/800V OBC mounted in a high-end vehicle is investigated using 3D simulation tools Ansys HFSS. The study emphasizes the necessity of full 3D simulation over SPICE, proposing a step-by-step approach to component modeling. Additionally, the influence of the chassis enclosure on filter performance is highlighted, addressing challenges related to electromagnetic shielding and thermal management. Ultimately, the study demonstrates applicability as a predictive tool for engineers, improving high-quality simulations of EMI filter insertion losses. This research aims to enhance reliability and performance in EV sub-systems while ensuring compliance with imposed standards.

List of Tables

List of Figure

1. Introduction

Electromagnetic compatibility definition

Electromagnetic compatibility (EMC) is a critical field of study and engineering practice that addresses the interaction of electromagnetic fields with electronic devices and systems. It encompasses both the emission of EMI from devices and their immunity to such interference. The term emission refers to the unintentional radiation or conduction of electromagnetic energy from a device, addressed as aggressor; such energy emitted by a device can interfere with the operation of nearby equipment, addressed as victim. Much more the victim is surrounded by aggressors, higher immunity level is required to guarantee functionalities. Therefore, with immunity is described the ability of a device to withstand external electromagnetic interference without significant degradation of its performance. The role of an EMC engineer is to ensure that electronic systems can coexist without degradation of performance due to electromagnetic disturbances. From a design perspective, the EMC engineer faces a scenario composed by an aggressor, two possible electromagnetic noise propagation mechanism and a victim, as depicted in Figure 1.

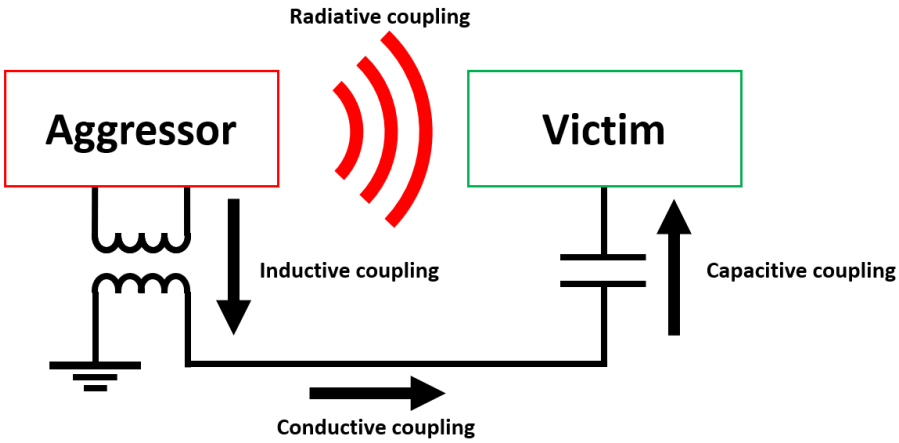

Figure 1: Aggressor/victim concept with electromagnetic noise coupling mechanism.

All electronic components are electromagnetic noise emitters and the knowledge on the physical mechanism behind the generation and propagation of the electromagnetic noise allows the design of effective countermeasures. Good design rules ensure that devices function harmoniously within their electromagnetic environments enhancing safety, reliability, and performance across various applications. Indeed, in some critical application like aerospace, medical, automotive… EMC play an important role to ensure minimal reliability and the safety of end-users. EMI are defined in terms of their propagation characteristics as common mode (CM) or differential mode (DM). CM EMI occurs whenever electromagnetic noise appears in phase on all input lines with respect to earth. Instead, DM EMI occurs when noise appears in opposite phase with respect to input lines and their returns. As a matter of fact, DM EMI propagates as a useful signal. Depending on the amount of CM and DM electromagnetic noise, different strategies can be adopted to mitigate their effects.

Problem background

To achieve EMC compliance, regulatory bodies such as the International Electrotechnical Commission (IEC), the International Organization for Standardization (ISO), and the Institute of Electrical and Electronics Engineers (IEEE) establish standards that define permissible emission and immunity levels for components installed in residential, industrial, and medical environments. Non-compliance with standards can result in product recalls, legal actions, and financial losses. Indeed, non-compliant devices could be classified as potentially harmful for end-users. To be compliant with standards systems should be accurately designed minimizing the emissions and increasing the immunity level. To fulfil those requirements, EMI filter design is crucial. EMI filter could be passive or active and specifically designed against conducted and radiated emissions at a specific frequency band as well as conducted and radiated immunity.

Objectives and scope of the thesis

The scope of this thesis is focused on passive EMI filter design from a SPICE to full 3D simulation, investigating the reason behind the necessities of FEM solutions applied on OBC. In particular, the objectives of this thesis can be splitted in two branches.

Scientific objectives: show how to build a SPICE model for Common Mode Choke (CMC) able to represent the real behavior of the electronic component in a

broadband way; showing how the full 3D simulation of a complete EMI filter is the best solution to represent and predict the CM and DM insertion losses.

Company objectives: optimization of the EMI filter design, building up a reliable approach to achieve system level compliance.

The study deals with the use of ANSYS platform for 3D simulation and schematic simulations. Component and filter characterization have been performed through VNA and LCR meter of a High Voltage DC EMI filter for an 800 V 22 kW OBC. Emphasis is put on dealing with chassis enclosure, necessary for cooling purposes as well as mechanical stresses, which might alter filter performances.

2. Company presentation

This thesis was developed during PhD high apprenticeship period in collaboration with Meta System. Meta System, founded in Reggio Emilia in 1973, has emerged as a leader in advanced electronic systems for the automotive sector. With over 50 years of experience, the company is defined by its commitment to innovation and technological advancement. Currently, Meta System holds more than 250 registered patents and employs over 300 professionals in Research and Development, collaborating with some of the world's foremost automobile manufacturers. In the automotive sector, E-Mobility represents a critical paradigm that encompasses the technical aspects of electric propulsion. The integration of in-vehicle communication, information technologies, and necessary infrastructure is essential for the optimal functioning of vehicles and fleets. Electric propulsion technologies, including hybrid vehicles, plug-in hybrids, and fully electric vehicles, have gained traction due to several key factors. The significant rise in emissions over recent decades has created an urgent need for cleaner alternatives. The rising costs associated with traditional fuel sources are becoming increasingly prohibitive. The finite

nature of natural fuel resources necessitates a strategic transition toward sustainable energy solutions. Meta System has been instrumental in advancing the E-Mobility movement, employing state-of-the-art methodologies to provide tailored assistance to global Original Equipment Manufacturers (OEMs). A major focus of Meta System is OBC, with several innovations designed to enhance electric vehicle (EV) performance: This compact unit, integrated into EVs, dynamically converting alternating current (AC) from public grids into variable direct current (DC) to efficiently charge the high voltage battery pack. Combining the functionalities of the OBC and the DC/DC converter is possible to enhance performance and efficiency, thereby reducing weight and costs. Meta System is also a pioneer in the application of advanced semiconductor technologies, in particular Silicon Carbide (SiC) Technology. Meta System, in fact, introduced the world's first 22kW SiC OBC. This technology enhances efficiency and performance compared to traditional silicon devices. As well as SiC technology, other wide bandgap technologies, like GaN, devices are under evaluation. Coupled with proprietary magnetic designs, this advancement positions Meta System at the forefront of technological innovation in E-Mobility. Safety remains a fundamental component of Meta System's product development. All offerings comply with rigorous automotive safety requirements, adhering to high voltage safety standards (ISO17409, ISO6469-3) and functional safety standards for road vehicles (ISO26262). Additionally, the Meta System Battery Charger is engineered to ensure the complete separation of electrical and cooling systems, while maintaining optimal thermal connections for electrical components. This design approach achieves high power density

within minimal volume, reinforcing Meta System's commitment to efficiency and reliability in E-Mobility solutions.

3. On Board Charger an overview

The OBC is a device integrated inside the vehicle that allows, by connecting to an alternating current (AC) power supply outlet, to convert energy to direct current (DC) and perform charging of a high-voltage HVDC battery while the vehicle is stationary. The OBC can be found in both BEVs (Battery Electric Vehicle - 100% Full Electric) and PHEVs (Plug-in Hybrid Electric Vehicle). An OBC must meet mainly two important requirements: high efficiency and scalability. An important requirement that on-board charging systems must meet is to have high energy efficiency (usually greater than 94%). The more efficient the conversion, the less heat is generated in the system, simplifying thermal management, increasing power density, and reducing the volume and weight of the solution. To achieve this, liquid cooling is used, which can keep the OBC in the optimal temperature range and minimize losses, maximizing efficiency. Another important requirement that any on-board charging system must meet is scalability, that is, the ability to handle the different power classes and different types of charging methods found in different countries [1]. The OBC communicates continuously with the vehicle's Battery Management System

(BMS) and other Electronic Control Units (ECUs) mounted on the vehicle through different standards.

OBC architecture

The typical architecture of an OBC can be synthetized as a logic part and a power part. Furthermore, the power part can be divided into four blocks, as depicted in Figure 2. Moreover, the image shows an example of a mechanical structure of an OBC where the HVAC, HVDC and Signal connector are highlighted nevertheless also the cooling ports.

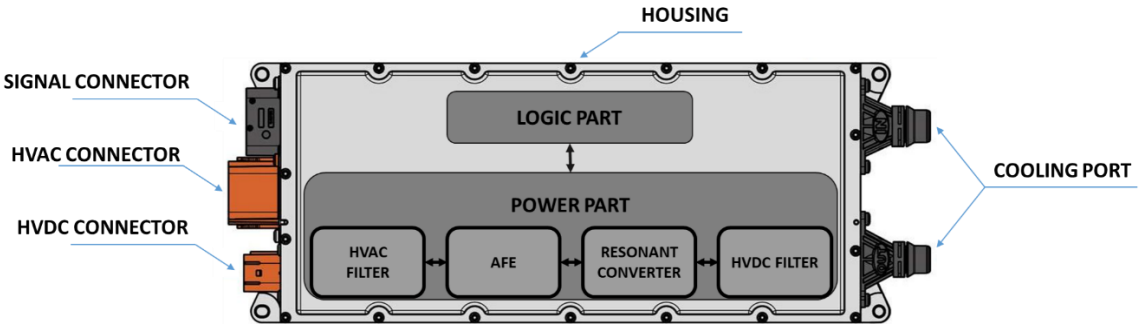

Figure 2: Block scheme of an OBC with main mechanical parts: cooling port, HVAC/HVDC/SIGNAL connector.

Logic Part

Focusing on an EV, the OBC often serves as the primary interface between the vehicle and the electrical grid, or in some cases, another vehicle. To ensure seamless operation, the OBC must manage various communication protocols through a central system board. In certain applications, communication between external sources, such as charging stations, and the EV is handled by a dedicated unit, known as the Electric Vehicle Charge Controller (EVCC). The EVCC

functions as an intermediary, gathering information from the grid or external source and relaying it to the relevant ECUs within the EV, but also OBC can handle it. This enables efficient data exchange across the vehicle's subsystems during charging or vehicle-to-grid operations. Various communication standards are employed, depending on the needs of real-time control, data exchange and diagnostic. From the slowest to the fastest one there are: Local Interconnect Network (LIN), Controller Area Network (CAN), Flex Ray, Media Oriented Systems Transport (MOST) and Automotive Ethernet. LIN, operating at low speeds (20 kbps), is used for non-critical subsystems like climate control and window regulation. One of the most adopted protocols is the CAN, supporting robust, real-time data transfer between ECUs at rates higher than 1 Mbps (CAN 2.0) in CAN FD. CAN is extensively adopted due to its high fault tolerance and suitability for critical operations, as in the OBCs or motor. A faster protocol up to 10 Mbps is the Flex Ray. Flex Ray is used in systems requiring precise synchronization and very high fault tolerance, such as advanced driver assistance. For multimedia and infotainment systems, MOST support high-speed data transfer (up to 150 Mbps), for advanced audio and video applications. Automotive Ethernet, thanks to its scalability and low latency, is increasingly employed for high-bandwidth applications, like autonomous driving and the infotainment, with data rates up to 1 Gbps. Operating over CAN or Ethernet networks, diagnostic protocols like Unified Diagnostic Services (UDS) and On-Board Diagnostics (OBD-II) are suited for vehicle monitoring and maintenance. Additionally, ISO 15118 facilitates communication between EVs and charging stations, enabling features like Plug and Charge and Vehicle-to-Grid (V2G),

which are essential for smart grid integration. These communication standards are designed to ensure real-time, reliable, and efficient data exchange across various subsystems, optimizing performance, safety, and energy management in electric vehicles.

Four different charging modes are reported by regulation and described in literature [2], [3], [4], [5], [6]. According to [6], derived from SAE J1772, there are Mode 1, Mode 2, Mode 3, and Mode 4, [3], [7]. In Mode 1-2-3 EV is connected directly or through fixed/portable charging stations to the 1-phase/3-phase grid to provide energy to the OBC, where the power conversion occurs, then to the battery. Mode 4 instead describes DC charging mode of the EV battery that is directly provided by the charging station without AC-DC power conversion. In Mode 2-3-4, safety is ensured by Proxy Pilot (PP) line that is terminated by vehicle inlet at socket side through a resistor which resistive value specify the maximum vehicle harness current capability. Signaling among the vehicle (typically the OBC) and charging station (fixed or portable, AC or DC) are managed through Control Pilot (CP) line that could work in Pulse Width Modulation (PWM) or Power Line Communication (PLC). According to Annex A of [6], CP wire could carry a PWM signal of 1 kHz. The duty cycle of the PWM signal defines the maximum current to be drawn from the grid. In Table 1 duty cycle range and corresponding current value are reported.

Table 1: Control Pilot Duty Cycle value and correspondent maximum charging current according to [6].

Duty Cycle (DC) [%]	Maximum Current [A]
DC<3	
7<DC<8	Values not allowed
97<DC<100	
3<DC<7	IEC 15118/IEC 61851 allowed
8≤DC<10	6
10≤DC≤85	DC × 0.6
85<DC≤96	(DC-64) × 2.5
96<DC≤98	80

Mode 1 may be prohibited in some areas due to safety lacks; on the contrary, Mode 2 and Mode 3 are extensively adopted. However, Annex 13 and Annex 19 of the regulation do not specify the use of auxiliary equipment (AE), referred to Electrical Vehicle Supply Equipment (EVSE) as indicated instead in Annex 4 for radiated narrowband and broadband electromagnetic emission.

From an EMC point of view, increasing the number of communications protocols means an increasing chance to have electromagnetic emissions nevertheless to increase the vulnerability of the system in terms of electromagnetic immunity. Dedicated protection circuitry composed of Common Mode Chokes (CMCs), capacitors and voltage suppressors (like TVS) are extensively used to limit the

amount of emission and improve immunity levels. Several standards are applied to test them, as reported in [8].

High Voltage EMI Filter boards

To be compliant with respect to standards, in the OBC considered, two main filter parts are designed, one at the HVAC side and one at the HVDC side. Depending on the volume availability, EMI filters can be placed on a dedicated board or in the same PCB as for power converter components. Those boards contain all the electrical components, in order to ensure low electromagnetic emission and high immunity level for the OBC. Typically, HVAC board present higher complexity due to the integration of high and low voltage components, like CMC, capacitors, MOV, relays, voltage detection circuitry… In this thesis passive HVDC filter and its components are extensively analyzed and described.

Power converter stages

Focusing on power conversion stages, the voltage conversion is managed by two blocks: Power Factor Correction (PFC) circuit and the resonant converter. The PFC stage typically adopts a boost converter topology, such as the Totem Pole or Vienna rectifier, which converts the AC input voltage into a regulated DC voltage. The specific DC voltage level is determined by the requirements of the high-voltage (HV) battery in the EV/PHEV. Common HV battery nominal voltages range from 400 V to 800 V, depending on the traction system of the vehicle. Thus, the PFC stage serves a dual function: it not only corrects the power factor to optimize energy efficiency but also boosts and regulates the input AC voltage

to a stable DC output suitable for the battery. The resonant converter, on the other hand, is responsible for fine-tuning the OBC's output voltage according to the HV battery's specifications, particularly in terms of its current/voltage profile. Additionally, the resonant converter provides galvanic isolation between the PFC stage and the battery by means of a transformer, ensuring safety and preventing direct electrical contact between the AC input and the vehicle's electrical system. This isolation is crucial for maintaining safety of power conversion process in the OBC.

Active Front End

In conventional PFC circuits, the AC input first passes through a diode bridge rectifier to convert the alternating current (AC) to direct current (DC). However, the use of diodes in this rectification process introduces significant power losses due to the forward voltage drop across the diodes, particularly in high-power applications. The bridgeless PFC topology solves this problem by eliminating the diode bridge, significantly improving stage efficiency. Instead of relying on diodes for rectification, the current is controlled by active switching components such as SiC MOSFETs or GaN FETs, which exhibit much lower conduction losses compared to conventional diodes,[9]. These active components, exhibiting lower forward voltage drops, are dynamically switched to perform rectification and power factor correction. In a PFC the totem-pole topology is commonly adopted,[10], [11], [12], [13], [14]. During the positive half-cycle of the AC input waveform, the low-side MOSFET conducts, allowing current to flow from the AC source to the bus capacitor. Conversely, during the negative half-cycle, the high-

side MOSFET conducts allowing the current to flow. This alternating switching ensures that current flows in both directions, providing efficient rectification without relying on the body diodes of the MOSFETs, thus minimizing losses associated with diode reverse recovery,[15]. A significant aspect of the totem-pole bridgeless PFC converter is its operation in continuous conduction mode (CCM). In CCM, the current through the inductor never falls to zero, ensuring that energy transfer to the output is continuous,[13]. CCM helps to reduce the current ripple, improving power quality, and enhances efficiency by reducing the need for larger filtering components since it reduces EMI. Moreover, it allows the converter to maintain a high-power factor, usually above 0.9, meaning that the input current is nearly in phase with the input voltage, which in turn reduces reactive power consumption and improves the system's energy efficiency,[13].

Whenever target efficiency becomes very high, interleaving technique can be adopted. The interleaved totem-pole bridgeless PFC converter is an advanced topology designed to enhance the efficiency and performance of AC/DC power conversion, particularly in high-power and high-efficiency applications such as OBCs. This topology addresses the limitations of traditional single stage PFC circuits by reducing conduction losses, current ripple, improving switching efficiency, and managing thermal stresses more effectively,[13], [14], [16]. Example of a three-phase totem-pole bridgeless interleaved PFC is reported in Figure 3.

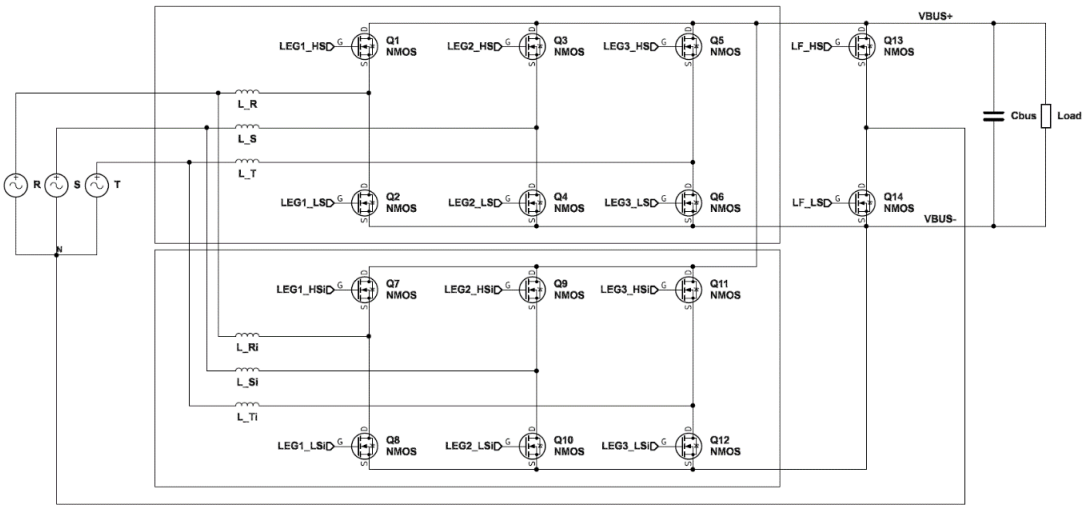

Figure 3: Structure of a three-phase Totem-pole bridgeless interleaved PFC

Interleaving involves the use of two or more converter stages operating in parallel, with each stage operating out of phase with the others. In a typical two-phase interleaved design, for instance, the switching operations of the two parallel converters are 180 degrees out of phase. This phase-shifted operation offers several benefits: the main one is the reduction of input current ripple. In single-phase PFC designs, the current ripple can be significant, requiring larger and more expensive filtering components to smooth the waveform. However, by interleaving the phases, the ripple currents generated by the individual converters cancel each other out to some extent, resulting in a much lower overall ripple. This reduces the size and cost of the input filter and enhances the overall power quality by lowering harmonic distortion. Reduced current ripple also improves the system's efficiency, as less energy is dissipated.

Beyond ripple reduction, interleaving provides critical thermal management benefits distributing power across multiple converter stages. This reduces the

thermal stress on individual components. This design allows for more compact, high-density power supplies, as thermal stress is better distributed, which helps in meeting the increasing demand for high power density. The parallel operation of interleaved phases further enables better performance under varying load conditions by sharing the workload, which also enhances the reliability and life of the components.

Resonant converter stage (LLC resonant converter)

An LLC resonant converter is a type of soft-switching DC-DC converter that utilizes a resonant tank composed of an inductor and capacitor to achieve high efficiency, particularly under varying load and input conditions. The LLC resonant converter is widely used in applications requiring high efficiency, high power density, and low EMI, such as in power supplies for servers, telecommunications, and industrial equipment,[17], [18]. The LLC resonant converter operates based on the principle of resonance between inductive and capacitive components, which allows it to switch by achieving zero-voltage switching (ZVS) turn-on and zero-current switching (ZCS) turn-off. This reduces switching losses in the power semiconductors and allows for higher-frequency operation, leading to smaller passive components helping in improve power density. At its core, the LLC resonant converter topology consists of five main components: a half-bridge or full bridge switching network, a resonant tank, a transformer, a rectifier and the output capacitor. An example of an LLC converter is shown in Figure 4, from [19].

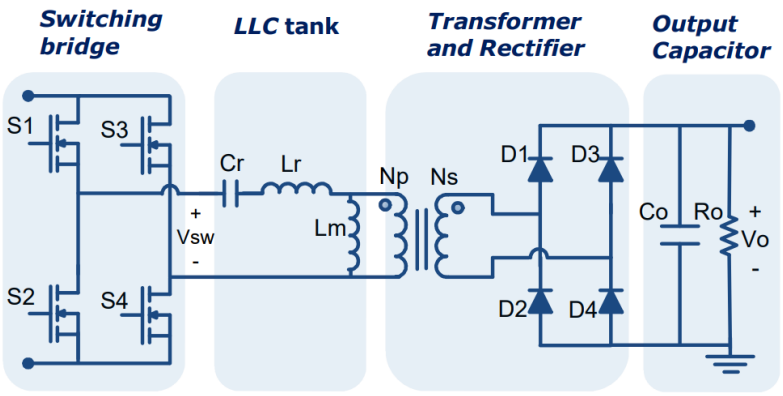

Figure 4: LLC resonant converter circuit,[19]

The resonant tank includes two inductors and one capacitor: one of the inductors is the transformer's magnetizing inductance, while the other is typically an external series inductor. The transformer guarantees the galvanic isolation between the input part to the output part of the converter, moreover its turn ratio defines the maximum and minimum voltage that the resonant convert can manage. The operation of the LLC resonant converter begins with the switching network, where power MOSFETs (or IGBTs) in a half-bridge or full-bridge configuration are switched at a variable frequency in order to convert DC to AC exciting the resonant tank. Variable frequency allows to manage a wide operating voltage range with high efficiency. Switching frequency is crucial in controlling the operation of the resonant converter and depending on its value the LLC converter can operate in different regions of resonance, to achieve various modes of operation. As depicted in Figure 5, the resonant converter could work at resonance frequency f_R, above and below it exploiting inductive ($f_{SW} > f_R$) or capacitive region ($f_{SW} < f_R$).

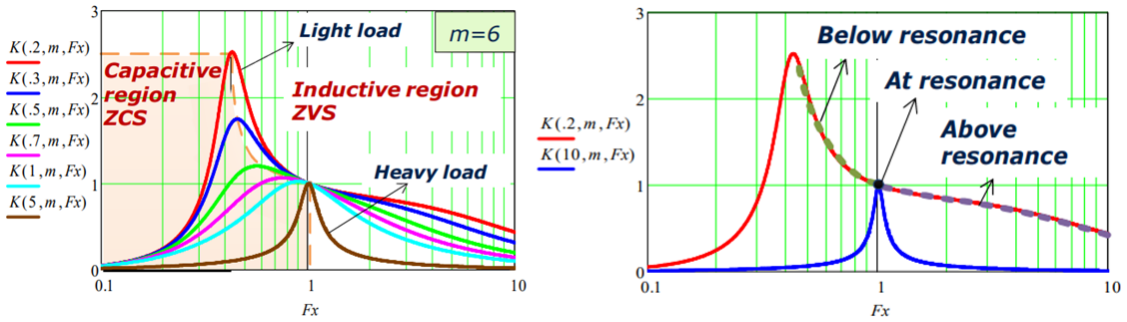

Figure 5: Operative region of LLC resonant converter,[19]

ZVS is achieved only in the inductive region and is preferred to avoid hard switching commutation of the body diode when the other MOSFET in the bridge turns on, reducing voltage spikes (so the EMI noise emitted by the converter) nevertheless reducing overall losses. At the resonance, the tank exhibits lowest impedance: this leads to the lowest losses since the energy is balanced between capacitive and inductive components, the converter operates at its nominal input and output voltage. When the converter operates, instead, above resonance or below resonance, it works as a buck and a boost converter respectively.

Power converter stages: an EMI perspective

EMI presents a critical challenge in power electronics, particularly in Power Factor Correction (PFC) converters and LLC resonant converters, both of which are extensively used in modern power conversion systems. These converters are designed to operate at high switching frequencies, managing significant amounts of power. While these high frequency switching operations improve power density and efficiency, they simultaneously introduce unwanted electromagnetic noise that can degrade system performance, violate standards, and interfere with nearby electronic devices. Understanding the sources, mechanisms, and characteristics of EMI in both PFC and LLC converters is essential for effective suppression techniques ensuring reliable system performance.

EMI in PFC

Power Factor Correction (PFC) circuits are crucial to obtain high efficiency of power systems by ensuring that the current drawn from the AC mains is in phase with the voltage. This is achieved by reshaping the input current waveform, minimizing low order harmonics content, and improving the power factor. However, the switching behavior in PFC converters introduces EMI due to the nature of high-frequency switching, which results in rapid changes in current and voltage. These changes, combined with non-idealities such as parasitic inductance and capacitance in the circuit, generate both DM and CM electromagnetic noise. In a boost-type PFC converter operating in Continuous Conduction Mode (CCM), a semiconductor switch turns on and off at high

frequencies, typically between 20 kHz and 150 kHz. These rapid di/dt (current change) transitions generate high-frequency current ripples, which manifest as EMI across the input lines which is mainly DM one, [20], [21], [22]. In Figure 6 L1, L2, L3 and N current waveforms collected from a 22 kW OBC with a Totem-pole bridgeless PFC converter are shown.

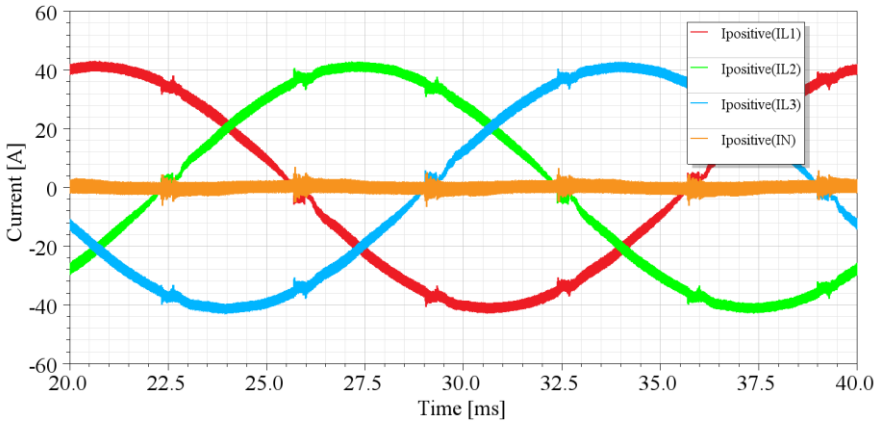

Figure 6: Typical current waveform of a three-phase with neutral Totem-pole bridgeless PFC converter

In addition to DM noise, CM EMI is also present in PFC converters. This form of electromagnetic noise is often generated by high-speed switching transients at the switching node, where rapid dv/dt (voltage change) transitions occur. These high-voltage spikes are coupled to the ground through parasitic capacitances between the switching node and the chassis or ground plane, creating a common-mode current,[23], [24]. Parasitic capacitance value depends heavily on the surrounding system and is also strictly correlated to MOSFET cooling technology. Indeed, if the MOSFET is dissipated through an Insulated Metal Substrate (IMS) or through a dedicated Thermal Interface Material (TIM), both of them in contact to cooling system, the total parasitic capacitance to ground change according to the dielectric permittivity of the interface in between the two

conductive parts reaching hundreds of pF. In Figure 7, electromagnetic noise collected at L1 has been numerically decomposed in CM and DM showing how, for the PFC, DM electromagnetic noise is predominant at lower frequencies reaching values above 140 dBµV.

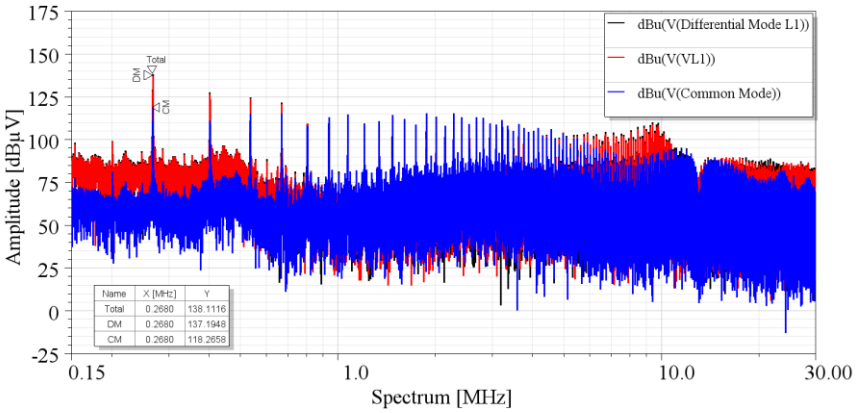

Figure 7: Electromagnetic noise collected from the LISN at L1 numerically splitted in CM and DM contribution

Also, reverse recovery behavior of diodes used in the PFC converter's rectification stage can also contribute to EMI. During switching transitions, particularly when the diodes switch off, the charge stored in the diodes causes a reverse recovery current. This reverse recovery current introduces sharp transients, increasing the generation of high-frequency electromagnetic noise.

EMI in LLC Resonant Converters

As reported before, LLC achieve soft-switching, which reduces switching losses and electromagnetic emission compared to hard-switching topologies. LLC converters typically operate at higher frequencies, often in the range of hundreds of kilohertz, and they achieve zero-voltage switching (ZVS) or zero-current switching (ZCS), particularly at or near the resonant frequency. This leads to a

reduced EMI generation whenever the soft-switching behavior is achieved but is not completely quiet. As for all the power converters, EMI in LLC converters primarily arises from dV/dt transition that excites the non-linearities of the system, depending again on parasitic elements in the circuit and on the high-frequency oscillations within the resonant tank. This high-frequency electromagnetic noise contributes to both DM and CM EMI, although DM noise tends to be less severe compared to the noise emitted by PFC stage. Since the EMI noise is prevalently common mode, it propagates throughout parasitic both at the input and output side of the converter. The electromagnetic noise resulting from high switching frequency of the primary side can capacitively couple to the secondary side through the parasitic capacitances between the transformer's windings [25], [26], [27], [28]. The magnitude of the EMI propagated by the transformer increases with switching frequency and is boosted by the parasitic capacitances. Additionally, rectifier stages in LLC converters can also generate significant EMI, particularly if fast-recovery diodes or synchronous rectifiers are employed. As reported previously, fast recovery diodes, which are often used for their efficiency in high-frequency converters, exhibit a sharp reverse recovery current when switching off, causing high-frequency oscillations. These oscillations are a source of both DM and CM electromagnetic noise, which can propagate through the converter and into the surrounding environment. Synchronous rectification, while more efficient than diode-based rectification, introduces its own switching electromagnetic noise due to the fast transitions in MOSFETs used for synchronous rectification.

EMI Mitigation Techniques

Mitigating EMI in PFC and LLC converters requires a combination of circuit design, filtering, layout optimization and control strategies leading on a strict collaboration between different departments (Power dept., Mechanical dept., PCB dept. and FW dept.) in order to fulfil all different requirements.

Primally, the best control strategy and electromagnetic noise mitigation techniques must be adopted. Acting at FW level is the most flexible and cost impacting solution to reduce the electromagnetic noise emitted by the device. Techniques like spread spectrum modulation are effective in terms of EMI noise reduction. This technique aims to distribute the electromagnetic noise applying a variable switching frequency to converter stages like PFC. Varying the frequency the harmonic content spreads on a bandwidth, that depends on the frequency span adopted, thus reducing the amplitude of the electromagnetic noise. Several different modulating waveforms can be adopted like sinusoidal, triangular, Hershey-Kiss and pseudorandom. Adopting pseudorandom sequences is possible to obtain the lower EMI but at cost of high computational complexity that is not always available. The best compromise in terms of complexity and effectiveness is the usage of triangular waveform that can helps to achieve from 10 to 12 dB of reduction of the electromagnetic noise, depending on adopted modulation index [29], [30], [31].

Whenever FW countermeasures are adopted, electromagnetic noise usually persists at an unacceptable level. This is the main reason why the use of EMI filters is mandatory. EMI filter is designed to tremendously reduce the

electromagnetic noise exploiting low-pass filter topologies. Both DM and CM filters are employed to attenuate high-frequency electromagnetic noise before it can propagate through the power lines. These filters typically consist of passive components such as resistors, inductors and capacitors. EMI Filter can also be active. In these years several active EMI filter solutions has been studied and analyzed, [32], [33], [34], [35], [36], [37], [38],[39] and some solutions to mitigate CM electromagnetic noise are available on the market [40]. Snubber circuits are another technique commonly used to reduce high-frequency oscillations and voltage spikes caused by parasitic inductances and capacitances close to power stages. Snubbers, typically consisting of a series of resistors and capacitors, are placed across switching devices to dampen ringing and reduce the amplitude of high-frequency transients. Minimizing parasitic inductances and capacitances in the circuit, particularly at the switching nodes, reduces the generation of electromagnetic noise. Indeed, whenever proper layout is no more effective to limit the parasitic inductance, ringing appears, due to the interaction between inductance and parasitic capacitance of the MOSFETs, and dampening technique become crucial to manage it [41], [42], [43],[44], [45], [46].

Shielding, especially around component like power inductor, transformers and other high-frequency components, can prevent radiated EMI from interfering with nearby systems or components, filters included,[25], [28], [47], [48], [49], [50], [51]. An example of an application of a shielding technique against uncontrolled electromagnetic coupling due to high power density is described in [52]. In [52] to reach compliance, in terms of conducted emission on the main lines, a particular shield composed by stainless steel and a nickel coating has

been placed to reduce the coupling between a LV board and power stages. In the last section of this thesis, more results on the case studied by Camarda et. Al. are reported, showing how to reduce the electromagnetic noise collected at the main lines studying its coupling path.

4. EMI compliance of an OBC

In the automotive field, EMC plays a key role in terms of safety and reliability, being a blocking point for the release of the Type Approval (TA). TA is a critical step in the automotive manufacturing process, ensuring that vehicles (or component) meet necessary safety, environmental, and performance standards before they reach end-users. TA is typically mandated by regulatory bodies or government authorities and can differs by country or regions. For EMC compliance, several tests must be performed according to regulations and technical standards characterizing the behavior in terms of emission and immunity. Nevertheless, car maker typically asks to their supplier to satisfy customized requirements based on technical standards. With the transition from combustion engine to electric one, aimed supporting the green transition, Electric Vehicles (EV) represent some of the most complex systems to manage EMI. Various electronic components, including the Engine Control Unit (ECU), Battery Management System, radio and OBC, must operate in harmony to ensure the proper functioning of the vehicle. In [2], the OBC shall pass up to ten different

tests divided into immunity related tests and emission related tests to obtain the TA.

UNECE R10 Revision 6

One of the harmonized standards for automotive sector is the United Nations Economic Commission for Europe (UNECE) R10 Revision 6. Revision 6, published by United Nations Economic Commission for Europe (UNECE) is a regulation for automotive industry that address EMC issues in motor vehicles, divided into seven different classes (L, M, N, O, T, R, S) that includes also EV. The regulation is part of a series of regulations that harmonize vehicle standards across different countries and regions. Its purpose is to ensure safety and reliability of vehicles, testing the conducted and radiated emissions of all electronic and electrical equipment nevertheless the conducted and radiated immunity to different disturbances that could cause harmful situation for road users (passengers, pedestrians, other vehicles, …). Test methods and pass/fail criteria at which EV and Electrical Sub-Assemblies (ESA), like OBC, must comply are described from Annex 4 to Annex 22. Main goal of carmaker and their Original Equipment Manufacturers (OEMs) is to guarantee compliance with respect to all regulation parts, obtaining vehicle or ESA TA. All the tests regard EV and ESA in configuration “REESS charging mode couple to the power grid”, the normal charging mode operation. The acronym REESS stands for REchargeable Energy Storage System and refers to the powertrain part of the EV, [2].

The test that must be comply with to obtain the TA are summarized in Table 2.

Table 2: Summary of the applicable test divided into immunity and emission test according to [2].

Immunity Tests	Emission Tests
Immunity against Transient disturbances (Annex 10)	Broadband Radiated Emission (Annex 7)
Immunity against Electromagnetic Radiation (Annex 9)	Narrowband Radiated Emission (Annex 8)
Immunity against Electrical Fast Transient/Burst events (Annex 21)	Conducted Emission on AC or DC power lines (Annex 19)
Immunity against Surge events (Annex 22)	Conducted Emission on network and telecommunication access (Annex 20)
	Transient Emission (Annex 10)
	Harmonic Emission (Annex 17)
	Voltage Changes, Voltage fluctuations and Flicker Emission (Annex 18)

Customer compliance

To be compliant at vehicle level, carmakers ask suppliers to fulfil customized requirements based on technical standards. Those requirements change from carmaker to carmaker, depending on type of vehicle and collecting past issues experienced by engineers (that creates constraints in the design and the severity of the test) and the type of units that shall be integrated into vehicles. Moreover, requirements reported by carmakers are typically more stringent with respect to legal ones. The idea behind this request is simple: if a system shall be integrated into a more complex system, it is better to have most stringent requirements to easily reach system type approval. This is especially true for OBCs that are the first interface between the vehicle and grid, vehicle, loads, ... OBCs are mostly critical in terms of conducted emissions and radiated emissions due to their high-power density. An example of customized requirement base on CISPR 25 classes is reported in Figure 8.

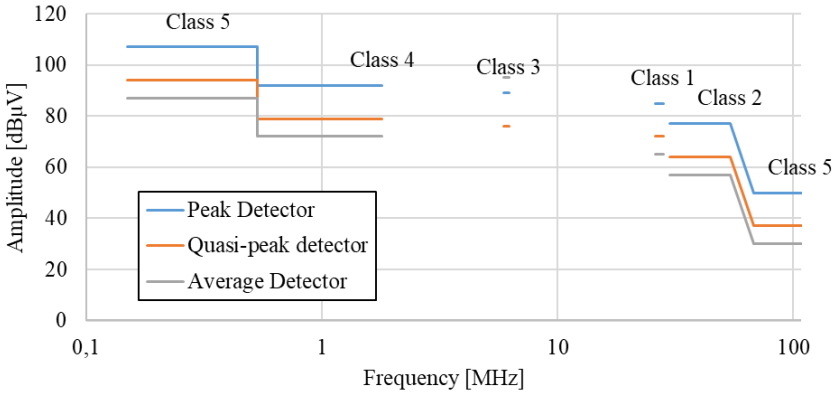

Figure 8: Example of customized limits applied on HV lines. For each band diffrent CISPR25 class are applied from 150 kHz to 108 MHz.

Conducted Emission characterization of an On-Board Charger

From a conducted emission point of view an OBC can be represented as a 3-port system composed of a low voltage part, high voltage DC part and high voltage AC part. Focusing on the content of this thesis, conducted emission on HVDC lines are considered. Customer requirements regarding emission on HVDC lines are based on CISPR25 standard.

Measuring set-up for Conducted Emission on HV lines: CISPR overview

The Comité International Spécial des Perturbations Radioélectriques (CISPR), is a part of the International Electrotechnical Commission (IEC) and is responsible for developing international standards to control and measure radio frequency interference (RFI). CISPR ensures electromagnetic compatibility (EMC) of electrical and electronic equipment. The organization plays a crucial role in maintaining the reliability and functionality of devices in environments where electromagnetic interference is a concern. CISPR is structured into seven subcommittees, each focused on specific aspects of electromagnetic interference and immunity. The first subcommittee is concerned with the protection of radio reception from interference caused by electrical and electronic devices operating in the frequency range of 9 kHz to 400 GHz. Its primary goal is to ensure that devices do not interfere with radio communication in their surrounding

environment. Another subcommittee focuses on the development of measurement instrumentation, facilities, methods, and analysis techniques to ensure the accuracy of EMI assessments. Another subcommittee establishes limits for radio disturbances emitted by electrical and electronic systems to protect communication systems and ensure electromagnetic compatibility. Additionally, CISPR addresses the immunity of electrical appliances, multimedia equipment, information technology devices, and broadcasting systems from external electromagnetic interference. This guarantees the reliable operation of such systems despite the presence of electromagnetic disturbances. CISPR collaborates with other IEC technical committees to apply standardized methods for immunity measurement and set appropriate test levels in product standards. Furthermore, it works jointly with other IEC and ISO committees to ensure that the EMC requirements in their respective standards align with those established by CISPR. CISPR also considers the impact of safety on disturbance suppression and the immunity of electrical equipment. This ensures that safety issues are integrated with the electromagnetic compatibility requirements of devices. CISPR includes not only Participating National Committees of the IEC, but also several international organizations such as the International Council on Large Electric Systems (CIGRE), the European Broadcasting Union (EBU), the European Telecommunications Standards Institute (ETSI), the International Amateur Radio Union (IARU), and the International Telecommunication Union's Radiocommunication (ITU-R) and Telecommunication Standardization (ITU-T) sectors.

CISPR 25 is particularly relevant to this thesis. CISPR 25 defines limits and measurement methods for radio disturbances in automotive environments, ensuring that vehicles onboard and external systems are protected from electromagnetic interference caused by electronic components within the vehicle. In the latest release of the CISPR25 Plug-in electric vehicle and electric vehicle are explicitly reported as device under test as well as their single units. Several test set-ups are reported to evaluate conducted and radiated emissions that are divided into several sub bands from 0.15 kHz up to 6 GHz. Limits are also reported in five different classes; Class 5 is the less restrictive one up to Class 1 that is more restrictive (in some bands the difference between limits could reach 40 dBμV). CISPR25 proposes test methods and requirements for LV components as well as HV components and depending on the nature of the system different annexes focus on each case. Annex H describes test set-up, methods and limits for components/modules used in PHEV and BEV such as inverters, OBCs, DC/DC converters, electrical heaters, and high voltage battery that presents both LV and HV connection. In particular, the Annex explicit its application on components with shielding HV cables. Conducted electromagnetic noise can be measured with two equivalent methods, current and voltage method, depending on the applied method different limits are applied. In voltage method, the electromagnetic noise is collected through dedicated line impedance stabilization network (LISN) that decouples the electromagnetic noise with respect to supplies voltage. In the case of current method, the electromagnetic noise is instead collected through a current probe placed at a specific distance with respect to the device under test, but the line

must be stabilized through the LISN as for the voltage method. LISNs are passive circuits composed by inductors, capacitors and resistors which values are different depending on the line that must be measured. Example of CISPR25 LISN for HV lines are reported in Figure 9 were also the equivalent impedance is shown. Thanks to the LISN, the electromagnetic noise can be collected in a reliable way, ensuring that the DUT is completely decouple with respect to the load.

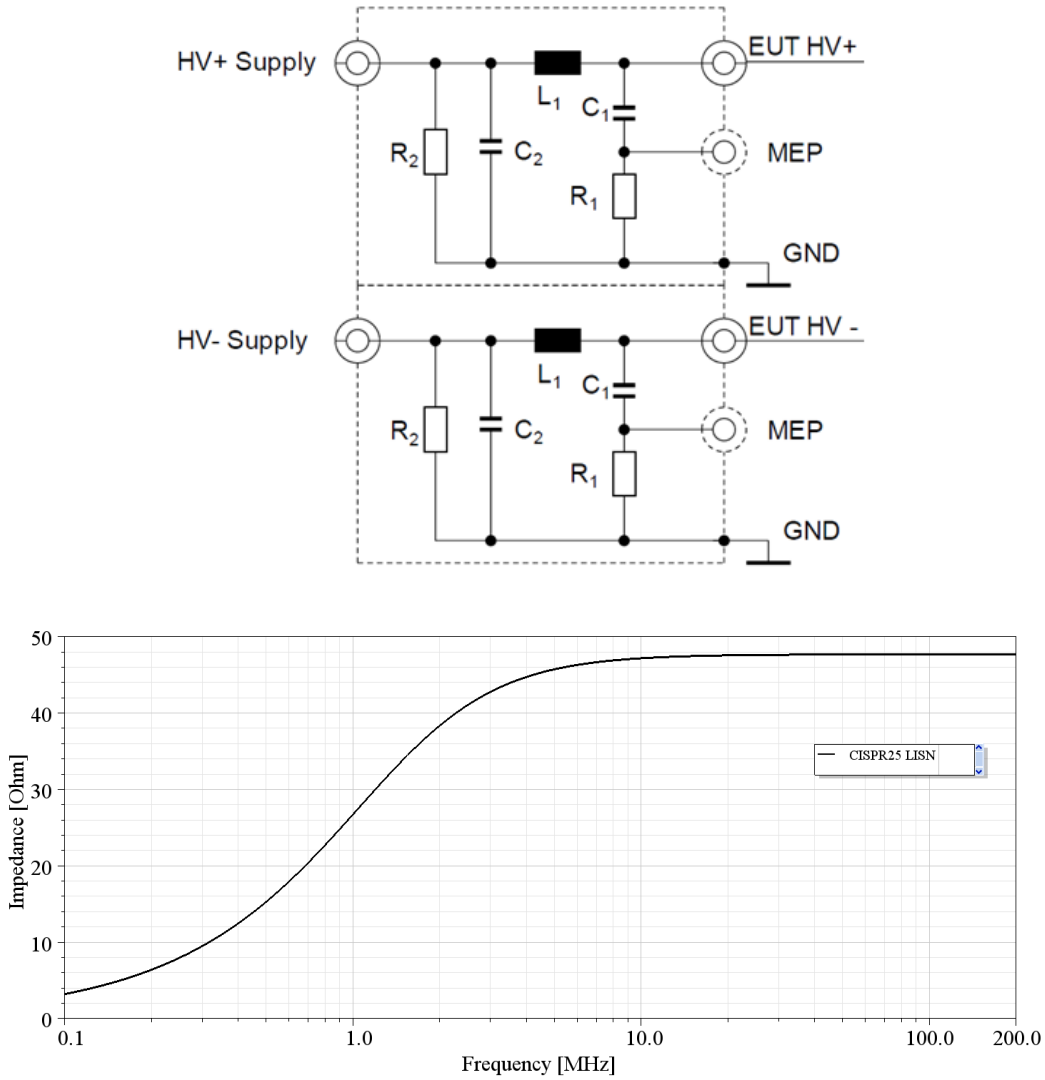

Figure 9: Electric scheme and impedance of CISPR25 HV LISNs, [53].

The set-up proposed by CISPR 25 used to characterize an EV component is reported in Figure 10.

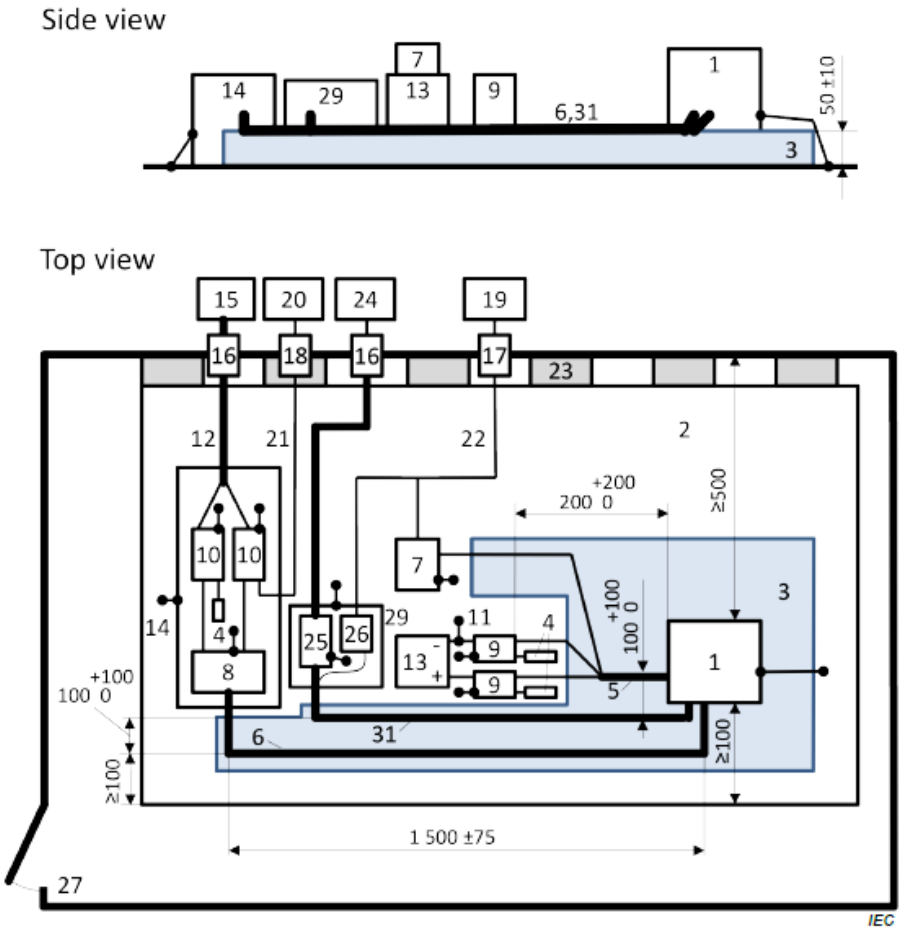

Key

1	EUT
2	Ground plane
3	Low relative permittivity support ($\varepsilon_r \leq 1{,}4$) thickness 50 mm
4	50 Ω load
5	LV harness
6	HV lines (HV+, HV−)
7	LV load simulator
8	Impedance matching network (optional)
9	LV AN
10	HV AN
11	LV supply lines
12	HV supply lines
13	LV power supply 12 V / 24 V / 48 V (should be placed on the reference ground plane
14	Additional shielded box
15	HV power supply (should be shielded if placed inside shielded enclosure)
16	Power line filter
17	Fibre optic feed through
18	Bulk head connector
19	Stimulating and monitoring system
20	Measuring instrument
21	High quality coaxial cable e.g. double shielded (50 Ω)
22	Optical fibre
23	Ground straps (see 6.2.1)
24	AC power mains
25	AMN for AC power mains
26	AC charging load simulator
27	Shielded enclosure
29	Additional shielded box (optional)
31	AC lines

Figure 10: Conducted Emission Set-up for HV lines, proposed by [53].

5. EMI Filter design

Characterization method for passive component

High quality EMI filter modelling requires accurate measures. A correct measure of the impedances of resistors, capacitors and CMCs facilitate understanding their performance evaluation and behavioral modeling, contributing to accurate EMI filter design and optimization. Whenever RF components are taken into consideration, the main useful instrument to obtain frequency dependent information is the Vector Network Analyzer (VNA). Despite low frequency behavior, where in principle impedance can be evaluated applying a sinusoidal excitation and calculating its value as ratio between the voltage and the current, at high frequencies passive components stops to behave as lumped elements becoming distributed elements. VNA allows the extraction of the scattering parameters, necessary to represent accurately the high frequency behavior of a system.

The simplest VNA presents two ports at which the component could be attached to extract four S-parameters: two reflection factors and two transmission factors. In Figure 11, is reported the analogy of the S-parameter with light, [54].

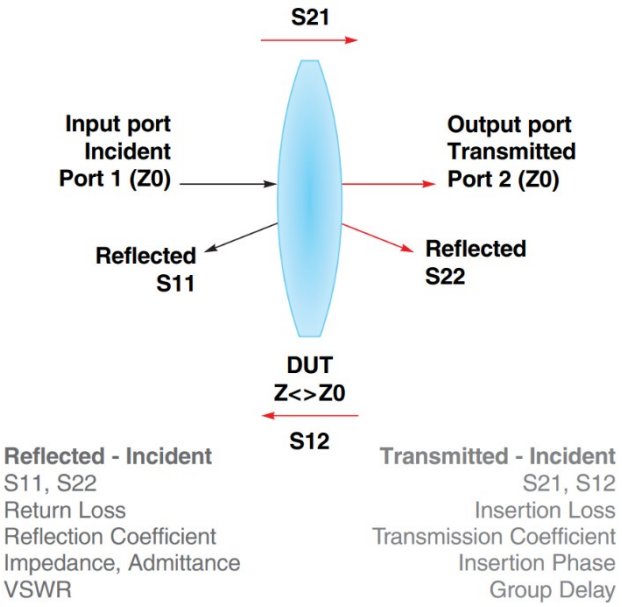

Figure 11: Light wave analogy for S-parameter,[54].

The resulting scattering parameters can be arranged in the matrix format as reported:

$$S = \begin{pmatrix} S_{11} & S_{12} \\ S_{21} & S_{22} \end{pmatrix}$$

$$S_{11} = \frac{b_1}{a_1} = \frac{V_1^-}{V_1^+}$$

$$S_{12} = \frac{b_2}{a_1} = \frac{V_2^+}{V_1^-}$$

$$S_{21} = \frac{b_1}{a_2} = \frac{V_1^-}{V_2^+}$$

$$S_{22} = \frac{b_2}{a_2} = \frac{V_2^-}{V_2^+}$$

Where S11 is the input port voltage reflection coefficient, S12 is the reverse voltage gain, S21 is the forward voltage gain and S22 is the output port voltage reflection coefficient.

S-parameters provide a complete insight into the linear behavior of RF components. Since high frequency measures are performed, accurate set-up, measuring technique and calibration must be considered in order to minimize as much as possible systematic errors. The impact of the test port cable on the incident and reflected wave are reported in the following equations, where emphasized the resulting delay effects on the incident wave.

$$a_i = e^{-j2\pi f\tau} a$$

$$b = e^{-j2\pi f\tau} b_i$$

Moreover, test cables present losses that in some cases can be reasonably neglected, especially when the length is short (e.g. 10 cm) and the frequency range is limited. Thus, S-parameters are an extremely accurate representation of the linear behavior of the component under test, describing how it behaves and how it could interact with other devices when it is embedded in a system. The obtained S-parameters are arranged in the so-called Touchstone file [55] that can be imported inside EDA to simulate complex systems. Nowadays VNA can directly calculate Z and Y matrices by exporting them as well as S-parameter as Touchstone files.

About passive component characterization, several methods are extensively reported in literature exploring the analysis of the parasitic introduced by measuring harnesses and how to overcome them through calibration, [56], [57]. In fact, the main question that arises whenever a component is characterized in RF falls on the reliability of the measurand. 2-port shunt-through and series connections are the most used providing, in a few seconds, touchstone file of the two-port network. Despite capacitors, inductors and resistors, CMCs are characterized in terms of several different impedances and present at least four ports. Typically, CMC are characterized in terms of mixed-mode S-parameters that takes into account the DM and the CM contributions when excited with CM or DM stimulus. In the Table 3 is reported the 4-port mixed-mode S-parameters.

Table 3: Mixed-mode S-parameters matrix composition and meaning for 4-port system.

			Stimulus			
			Differential Mode		**Common Mode**	
			Port 1	**Port 2**	**Port 1**	**Port 2**
Response	**Differential Mode**	**Port 1**	S_{DD11}	S_{DD11}	S_{DC11}	S_{DC12}
		Port 2	S_{DD21}	S_{DD22}	S_{DC21}	S_{DC22}
	Common Mode	**Port 1**	S_{CD11}	S_{CD12}	S_{CC11}	S_{CC12}
		Port 2	S_{CD21}	S_{CC22}	S_{CC22}	S_{CC22}

This leads to a dedicated arrangement of the input or output pin of the component to evaluate such values. In the Figure 12 it is reported the connection of a single-phase CMC useful to determine four different impedances: inter-winding impedance, DM impedance, CM impedance and phase impedance through single-port measurement.

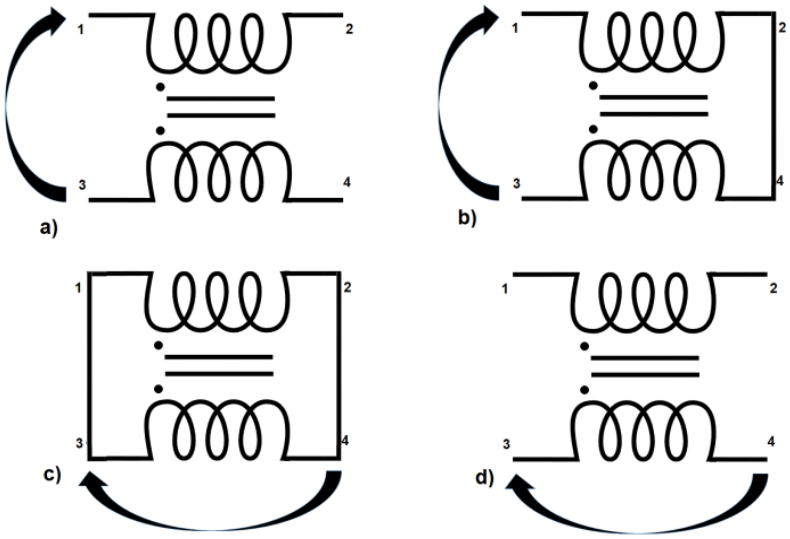

Figure 12: How to measure a) Interwinding Impedance, b) DM Impedance, c) Common Mode Impedance and d) Phase Impedance.

In high voltage applications, due to the bulky nature of the CMC, is easy to introduce unwanted parasitic trying to characterize it; however, thanks to the high order of magnitude of the impedance parasitic that are not properly cancelled out during calibration/de-embedding phase doesn't have appreciable effects for most of the measurand.

As well as components, also EMI filters can be characterized through VNA. Figure of merit for EMI filters is the so-called insertion loss, which is evaluated

in terms of DM and common mode insertion loss, defined as the reciprocal of the magnitude of the S21 parameter, so

$$IL = 10\,log_{10}\left|\frac{1}{S_{21}^2}\right| = -20\,log_{10}|S_{21}|\ \ [dB].$$

Evaluation of the DM insertion loss is typically done using an isolation transformer capable to inject pure DM signal. However, transformer parasitic affects the useful measurement bandwidth, reducing it.

State of the art of EMI filter

Whenever electromagnetic noise mitigation techniques are applied and still at an unacceptable level, proper EMI filters must be implemented to reach compliance. Depending on the application, EMI filters could be fully passive or also active and their topologies depend on several factors. As a prior step, EMI filters shall be designed according to the amount of electromagnetic noise that shall be managed. Indeed, since the EMI noise can be evaluated in terms of CM and DM noise, their amplitude and frequency will determine the insertion loss and the cut-off frequency that the filter must exhibit to manage both. Discrimination of CM and DM noise amplitude can be reached in different ways. Several electromagnetic noise splitters are available on the market or developed by researcher and the most advanced one apply modal analysis integrating LISN and EMI receiver [58]. After that, the topology must be evaluated in terms of the input and output impedance seen by the filter itself. Indeed, according to the nature of those impedances, high or low, the filter must ensure maximum impedance mismatch to reject the electromagnetic noise without instead propagating it. The rule of thumb of filter design, is resumed in Figure 13. For example, whenever the input and output impedance seen by the filter is low (capacitive), the impedance that the filter must exhibit must be high, to ensure maximum mismatch (inductive), and vice-versa.

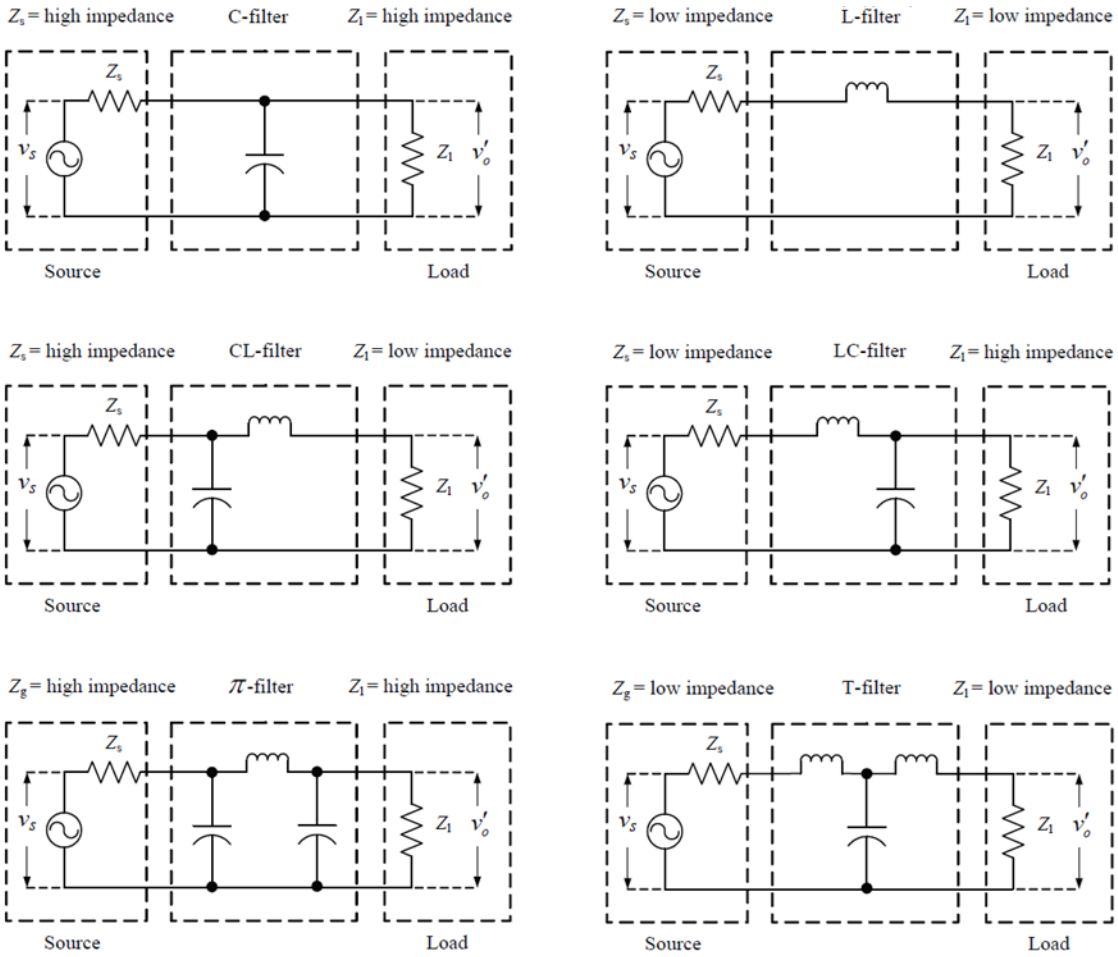

Figure 13: Basic filter configurations (C-filter; L-filter; CL-filter; LC-filter; π-filter; T-filter),[59].

In Figure 13, the main passive filter topologies are also reported, showing which topology can be adopted depending on the load and source impedances and on which attenuation is necessary (from 20 dB/dec. to 60 dB/dec.). Load and source impedances that can be extracted as shown in [59], [60], [61], [62], [63]. Design passive filters could be challenging. Depending on the application and besides impedances of the system, several constraints must be considered. Firstly, in high power applications, bulky components are necessary to manage the high amount of current, leading on a compromise and a challenge to ensure high power density and low EMI. Moreover, the performance of the filter decreases at

high frequency, due to parasitic of the passive components. Depending on the nature of the electromagnetic noise, high attenuation level is necessary. Since parasitic components detrimentally reduce filter attenuation at high frequency, components with lower parasitic can be used, thus affecting the overall cost of the system. In addition, component choice is limited by several constraints. As an example, total Y capacitors value is limited by touch current [64] values which increase as the total capacitance to ground increases. Thus, if high CM electromagnetic noise rejection is needed, large CMC are mandatory to achieve this performance. Additionally, depending on the requirements, different safety class of capacitor are available,[65]. Indeed, an EMI filter applied on AC or HVDC side must comply with safety requirements. As a result, a heavy and bulky filter is designed. As mentioned before, active EMI filters can be used in order to manage the EMI. Active components and networks can be designed to reduce EMI, sensing the CM and DM disturbances and injecting opposite signal providing active electromagnetic noise cancellation. This solution allows to reduce magnetic components size and number of filter component in general, thus reducing the overall volume occupancy of the filter [37], [39], [40]. However, several disadvantages are present. Firstly, the complexity of the system increases due to an increased amount of component; secondary, integrated solutions available on the market for automotive application are few and nowadays can only bring CM EMI filtering [39], [40]. Since in automotive field components must be properly qualified, AECQ mark, and integrated solutions are not fully available on the market; therefore, passive EMI filtering is nowadays the most adopted one. Indeed, using passive components is still a robust

solution, improving reliability of the system. Filters must also be robust enough against events that could destroy the components, like surges.

SPICE filter simulation of passive EMI filters

The simplest way to simulate an EMI filter is through SPICE models. For a passive EMI filter, three main components are present: capacitor, resistor and inductor. Frequency dependent models of components like resistor and capacitor are simple and extensively studied; describing how they are extracted is not one of the aims of this thesis. Thanks to simple geometry and approximations, both capacitors and resistors can be modelled as an RLC circuit, fitting well real impedance performances. In passive topologies, inductive components are typically Common Mode Choke (CMC), preferred to their advantages in terms of electromagnetic noise rejection. A CMC is an electromagnetic component used to suppress EMI by filtering CM and DM electromagnetic noise in electrical circuits. It consists of a core with two or more windings wrapped around it in the same direction. Depending on the application, the core could be constituted by a ferrite material or a nanocrystalline one, exhibiting very high magnetic permeability values and saturation characteristics. From a theoretical point of view when CM electromagnetic noise currents, which are in phase and identical in magnitude, flow through the windings, they produce magnetic flux inside the core that sum up with each other, generating high impedance and effectively dissipating electromagnetic noise. Instead, the CMC allows DM signals to pass exhibiting a very low impedance. Indeed, DM currents, which are equal in

magnitude but flow in opposite directions, produce magnetic flux inside the core that cancel each other. This concept is shown in Figure 14. In practice, the CMC exhibit a leakage inductance that helps to counteract DM electromagnetic noise, relies on a double benefit from the usage of this component. As a result, the CMC can be used to design filters able to manage both CM and DM electromagnetic noise, reducing the number of components and the total costs of the system.

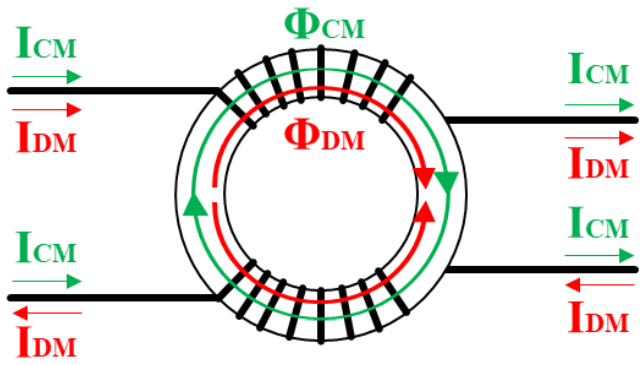

Figure 14: CM and DM current path and injected magnetic flux inside the core of a 2-wire CMC

CMC are widely utilized in applications such as power supplies, data transmission lines, electric vehicles, and audio systems to reduce EMI, ensure compliance. In electric vehicles, for example, CMCs play a critical role in filtering electromagnetic noise from power electronics components like inverters, BMSs, and OBCs.

In the next subsections, a novel SPICE model of a CMC used inside the HVDC filter of a 22 kW OBC are presented, showing the complexity of the models and how reliable is. The model was developed in collaboration with ANSYS and

presented during the IEEE International Symposium on Electromagnetic Compatibility, [66].

SPICE models of Common Mode Choke

As described before, CMC EMI performance is generally described by two main parameters: Z_{DM} and Z_{CM} throughout which manage both CM and DM electromagnetic noise. Both impedances depend on the geometry of the system, nevertheless the number of wires and the magnetic properties of the core. Several models, geometry dependent, can be developed, to represent the Z_{DM} and Z_{CM}. Most of them assume the CMC as a symmetric structure. Thanks to symmetry approximation, the estimation of a parameter such as stray capacitance becomes easier. From the estimation of the parasitic it is possible to build up a SPICE model able to represent the CMC in a broadband way. Those models should consider as much as possible all component characteristics and possible side effects caused, for example, by chassis, thermal interface materials, etc. On the other hand, the model must be simple and user-friendly.

In literature most of the proposed models present lack in terms of impedances representation and few degrees of freedom. Kovacic et. Al, present an analytical broadband model of a CMC for mono-phase and three-phase applications able to extract the CM impedance starting from complex magnetic permeability information [67]. The proposed model considers each turn-to-turn and turn-to-core parasitic capacitance, each self and mutual inductance between turns showing good matching between model and measures up to 30 MHz. As stated

by Kovacic et. Al, this approach allows to manage each single parameter and can be useful if a fine tuning occurs but lacks due to the necessity of complex magnetic permeability up to hundreds of MHz. Additionally, only CM impedance is evaluated: no additional information on other impedances has been provided. In [68] and [69], a complete model of CMC is reported where not only Z_{CM} and Z_{DM} has been considered, but also Z_{IW} and Z_{PH}. Besides the rigorous approach, the circuit model is not clearly described and presents an important issue: when CM impedance is evaluated, the Z_{DM} effects are not considered which sum-up with Z_{CM} affecting its estimation. Also, in [68] equivalent model of CMC applied on an EMI filter is proposed but the validity of the model is limited to 30 MHz. In [70], a behavioral model of CMC has been addresses through impedance fitting. Besides good matching from 100 Hz to 100 MHz, the model presents a cascade of a CM and DM stage which one is furthermore divided in cascaded impedance blocks detrimentally increasing the complexity of the model.

In this thesis a broadband circuit model, validated up to 200 MHz, of a CMC useful at project early-stages is presented. A CMC used inside the output filter for an OBC with 22kW of maximum output power at 800V on battery side has been considered. To model the CMC correctly, it is necessary the knowledge of some parameters like Z_{CM}, Z_{DM}, Z_{IW} and Z_{PH} to build up the model. In Figure 15, those impedances are represented.

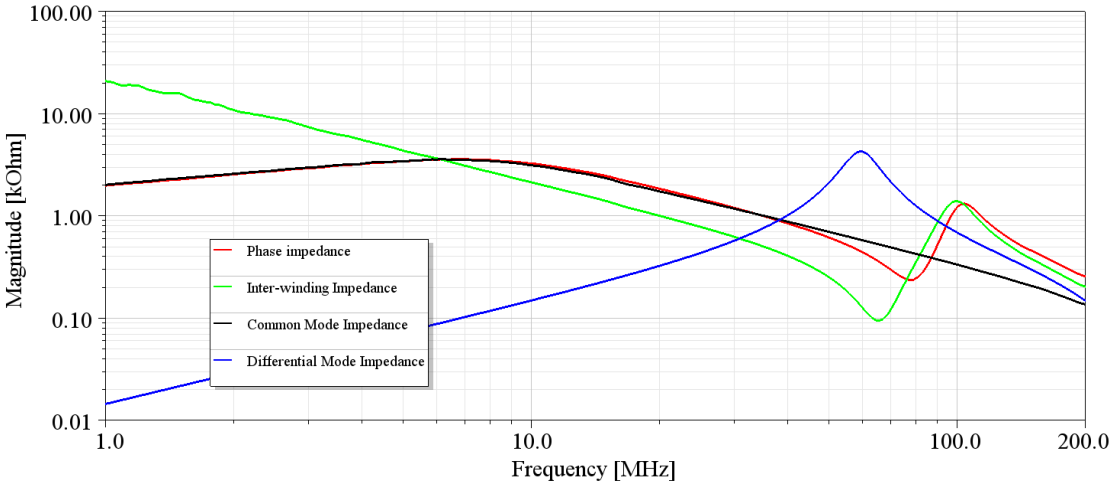

Figure 15: VNA measured values of Interwinding Impedance, Differential Mode Impedance, Common Mode Impedance and Phase Impedance according to the schemes reported in Figure 12.

Since Z_{DM} can be easily represented by an RLC equivalent circuit, for Z_{IW} the admittance circle method is suitable thanks to its similar behavior of a quartz crystal. In this way Z_{IW} can be represented as a Butterworth – Van Dyke (BVD) network like the one showed in Figure 16, where the resistive and inductive component has been splitted for symmetry purposes.

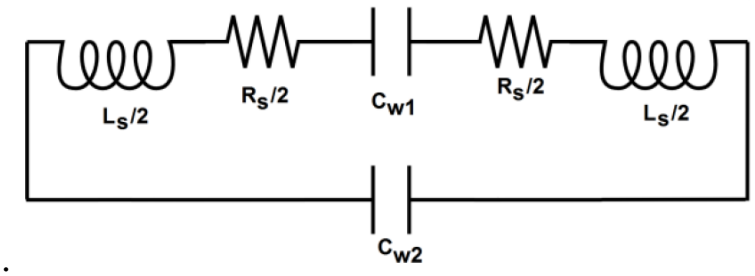

Figure 16: Resulting Butterworth - Van Dyke network to represent Interwinding Impedance, resistive and inductive parts are splitted to have a symmetric structure,[66].

Capacitive part of BVD network can be extracted from the Z_{IW} as

$$C_{par} = \frac{1}{2\pi f \cdot Z_{IW}}$$

In this case $C_{par} = 6.88\ [pF]$; according to the method the network presents a series and a parallel resonance that occurs at $f_S = 72.2\ [MHz]$ and $f_p = 96.9\ [MHz]$ frequencies respectively. Knowing the frequency values, it is possible to extract C_{w1} and C_{w2} as

$$C_{w1} = \frac{f_s^2}{f_p^2} \cdot C_{par}$$

$$C_{w2} = C_{par} - C_{w1}$$

Since $C_{w1} \approx \frac{C_{par}}{2}$, the circuit can be seen as fully symmetric.

The resistive part can be extracted as follows:

$$R_s = \frac{1}{Y_{IW}(f_z)}$$

where f_z is the frequency where $\arctan\{phase[Y_{IW}(f)]\} \to 0$, obtaining $R_s = 110\ [\Omega]$.

The inductive part can be extracted from the resonant frequency of LC tank

$$L_s = \frac{1}{(2\pi f_s)^2 C_{w1}}$$

obtaining $L_s = 1.5\ [\mu H]$.

Once obtained all the values, a series-to-parallel conversion of the RL tank has been applied since it helps to build the overall model, reported in Figure 17: Equivalent circuit for the extraction of the Common Mode Impedance of the CMC without and with DM residual impedance compensation network. When the CMC is connected in CM the Z_{DM} must be compensated otherwise would contribute to Z_{CM} value; indeed, a residual $L_{DM}/4$ inductance still in series with the CM impedance affecting its value. Adding an RL network composed by negative values, as shown in Figure 17, allows to cancel out the residual Z_{DM} when the ports are shorted in CM. As reported in Figure 18, the impact of the residual Z_{DM} is compared with the measure and the resulting Z_{CM}, obtained with compensation circuit. The Z_{DM} residual affects the Z_{CM} at high frequency, from 20 MHz above.

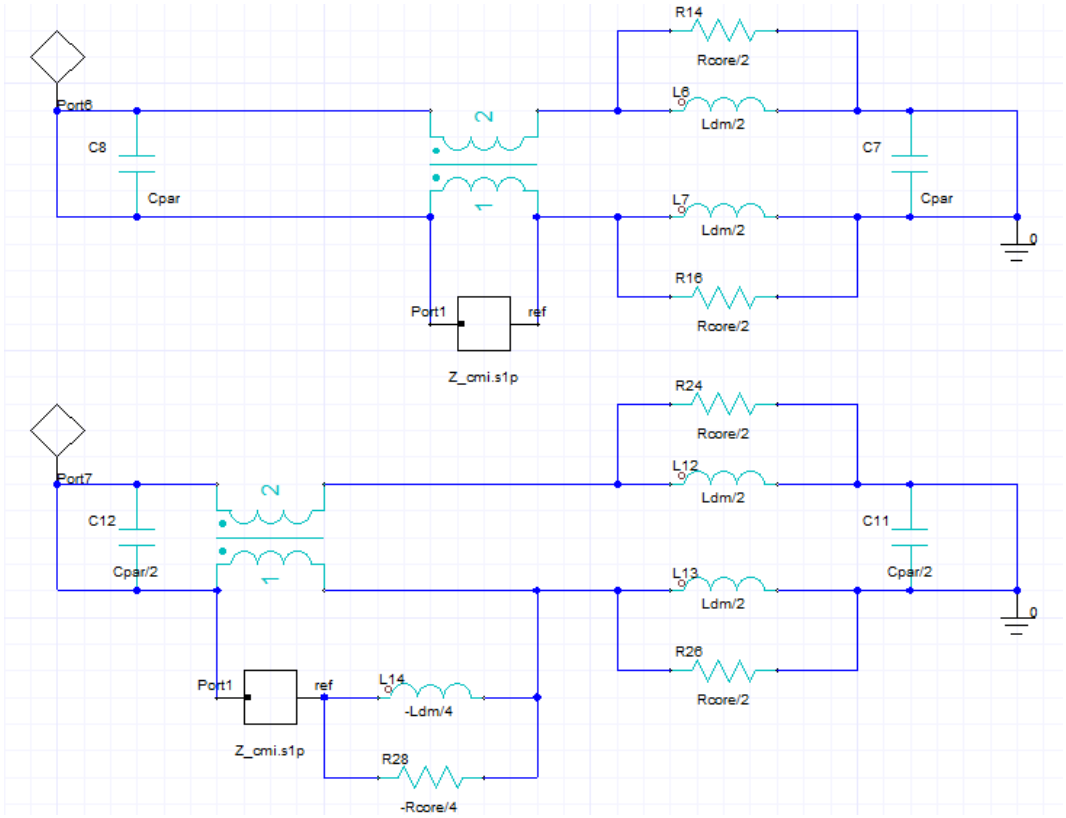

Figure 17: Equivalent circuit for the extraction of the Common Mode Impedance of the CMC without and with DM residual impedance compensation network.

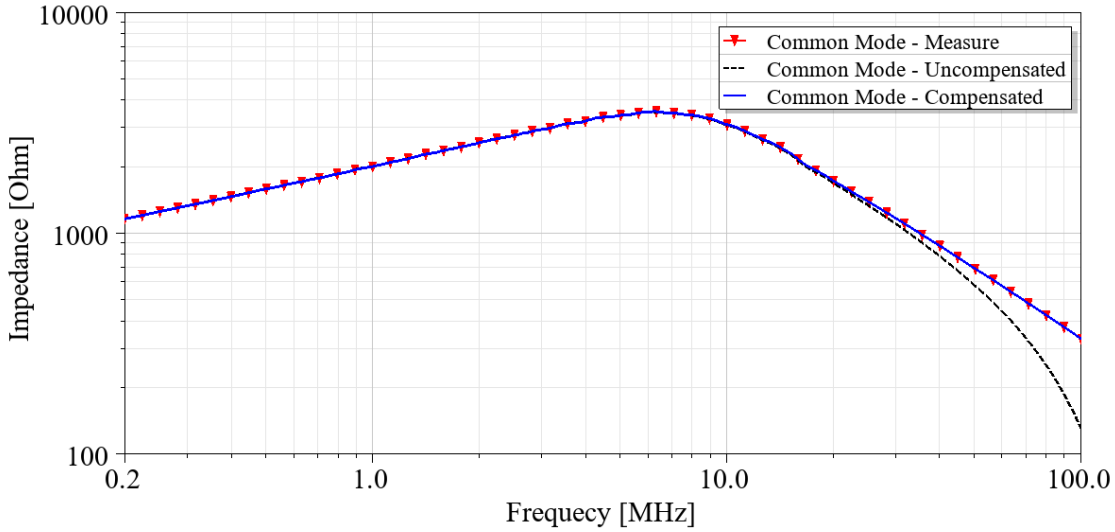

Figure 18: CM Impedance, $Z_{CM,}$ comparison between VNA measure and the uncompensated and compensated network.

The proposed model is able to match Z_{CM} and Z_{IW}; however, it is not able to fully represent the Z_{DM} since $L_p \approx 1.5\ [\mu H]$ respect $L_{DM} \approx 2.3\ [\mu H]$, as shown in Figure 19. This lack of impedance can be overcome by increasing the complexity of the model.

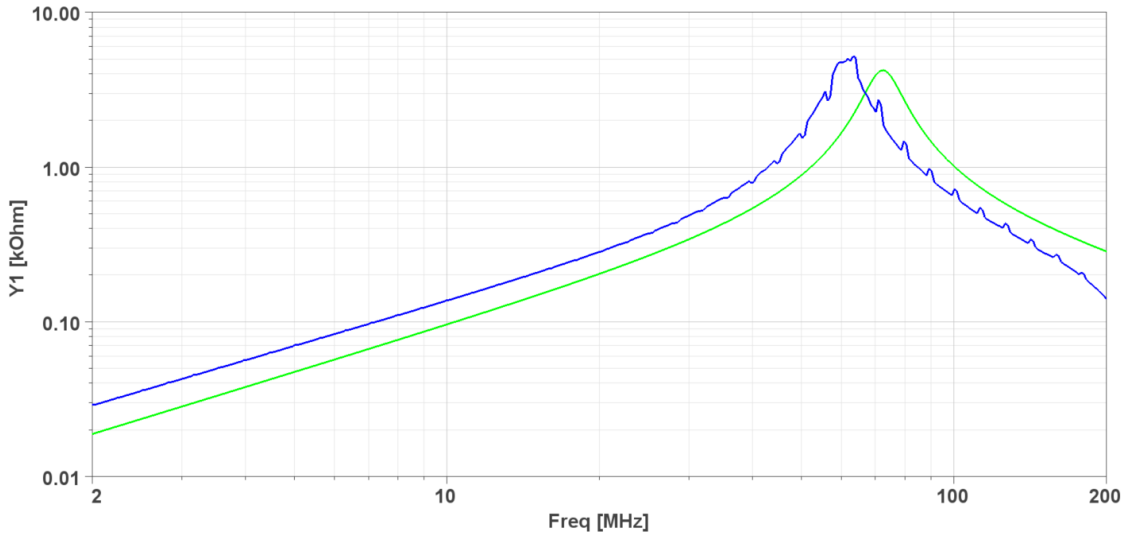

Figure 19: Mismatch between DM Impedance, Z_{DM}, measured through VNA (blue line) and simulated (green line) through equivalent circuit of the CMC,[66].

SPICE model of Common Mode Choke with L_{DM} compensation

As shown in [66], the CMC model has been furthermore improved, increasing the complexity of the system. Since DM inductance and phase inductance are different, lacks on Z_{DM} representation has been highlighted with the circuit in Figure 17. The reason behind this mismatch can be related to a different current path: when the CMC is closed in DM, the current is forced to flow along each winding; instead, when the Z_{IW} is evaluated the current return path length presents a lower average value, due to the distributed parasitic capacitance between each wire, then forming loop inductance which results to be lower with respect to the case at of DM measure. Starting from that information, the model has been improved adding the effect of an external leakage inductance which value is defined as the difference between L_{DM} and L_P and determined through fitting parameters by Optimetrics analysis (ANSYS Circuit design). The final complex model of the CMC is the one reported in Figure 20. As well as for the L_P, also the additional networks must be compensated to obtain matching in Z_{PH}, see Figure 21.

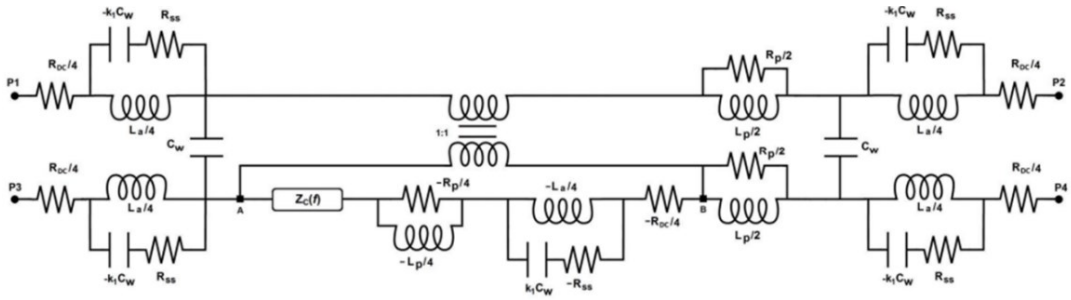

Figure 20: Equivalent final circuit model for the CMC,[66].

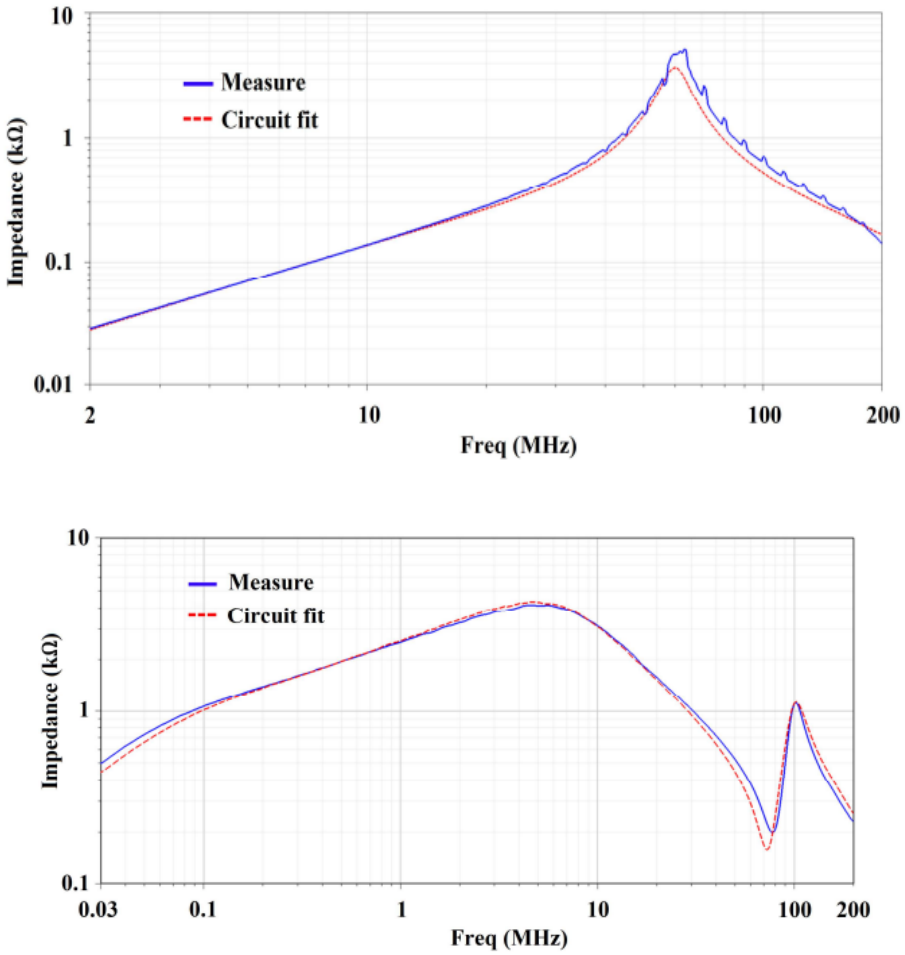

Figure 21: Impedance fitting for Z_{DM} and Z_{PH},[52].

In this model, the Z_{CM} is a touchstone file containing the measured impedance through VNA and LCR meter. In [66] has been also shown a method to model Z_{CM} as a SPICE circuit as well. Good Z_{CM} can be obtained through accurate extraction of complex magnetic permeability, measured based on [71]. Complex magnetic permeability depends on geometrical parameter of the core: inner and external diameter (D_{int} and D_{ext}) and core height (H_C). Real part and imaginary part of complex permeability can be extracted from the following formulas, where $k(f)$ embrace the geometrical properties of the core.

$$k(f) = \frac{|Z(f)|}{\mu_0 \cdot f \cdot H_c \cdot \ln\left(\frac{D_{ext}}{D_{int}}\right)}$$

$$\mu_r = k(f) \cdot \sin\{arg\{Z(f)\}\}$$

$$\mu_{im} = k(f) \cdot \cos\{arg\{Z(f)\}\}$$

Real part and imaginary part of the complex magnetic permeability can be fitted separately through weighted poles and zeros, based on conventional Lorentz/Debye resonator model. The real part and imaginary part have been fitted by applying the following equations:

$$\mu_r(f) = 1 + \mu_s \left(\frac{\omega_{s1}^2}{\omega^2 + \omega_{s1}^2}\right)^a \cdot \left(\frac{\omega_{s2}^2}{\omega^2 + \omega_{s2}^2}\right)^b \cdot \left(\frac{\omega_{s3}^2}{\omega^2 + \omega_{s3}^2}\right)^c \cdot \left(\frac{\omega^2 + \omega_{s4}^2}{\omega_{s4}^2}\right)^d \cdot \left(\frac{\omega_{s5}^2}{\omega^2 + \omega_{s5}^2}\right)^e$$

$$\mu_{im}(f) = k_0 \cdot \frac{(\omega \cdot \omega_{sa})^{\alpha 1}}{(\omega^2 + \omega_{sa}^2)^{\alpha 2}} \cdot \left(\frac{\omega_{sb}^2}{\omega^2 + \omega_{sb}^2}\right)^\beta \cdot \left(\frac{\omega^2 + \omega_{sc}^2}{\omega_{sc}^2}\right)^\gamma \cdot \left(\frac{\omega_{sd}^2}{\omega^2 + \omega_{sd}^2}\right)^\delta$$

$$k_0 = 2^{\alpha_2} \cdot \mu_{im|MAX} \cdot (\omega_{sa}^2)^{\alpha_2 - \alpha_1}$$

Some of the parameters can be extracted by the shape of the complex permeability, like $\mu_{im|MAX}$.

In this way the Z_{CM} can be represented as an RLC circuit, frequency dependent, that considers geometrical and magnetic parameters of the core. The fitting has been obtained through mathematical models with the help of Ansys tool (NDE). As reported in [66], an example of the application of the model fitting is reported in Figure 22, where through fitting the real part and imaginary part of the magnetic permeability the matching of the CM impedance has been reached as shown in Figure 23.

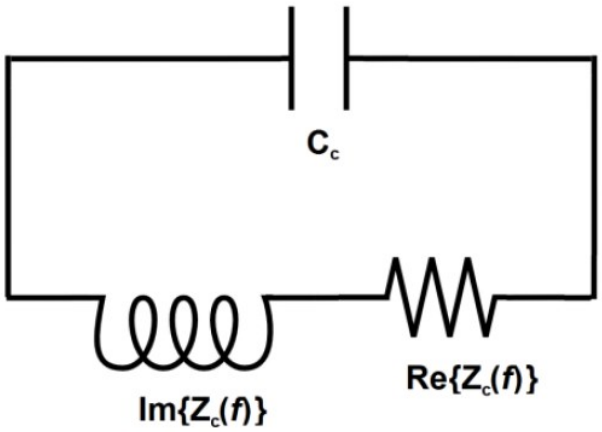

Figure 22: Equivalent network for the representation of the CM impedance of the choke through frequency dependent component,[66].

The parameter used for fitting real part and imaginary part of the complex permeability are reported in Table 4 and Table 5 respectively.

Once the whole circuit model is found, a touchstone file can be created and used among all simulators able to exploit such format.

Table 4: Fitting parameter for real part of complex permeability of the core, [66].

Parameter (Real Part)	**Units**	**Value**
ω_{s1}	Rad/s	$2.85 \cdot 10^5$
ω_{s2}		$9.42 \cdot 10^7$
ω_{s3}		$6.28 \cdot 10^6$
ω_{s4}		$1.88 \cdot 10^6$
ω_{s5}		$1.26 \cdot 10^9$
μ_s		58300
a		0.45
b		0.29
c		0.055
d		0.1
e		0.15

Table 5: Fitting parameter for imaginary part of complex permeability of the core, [59].

Parameter (Imaginary Part)	**Units**	**Value**
ω_{sa}	Rad/s	$4.02 \cdot 10^5$
ω_{sb}		$3.17 \cdot 10^7$
ω_{sc}		$6.28 \cdot 10^8$
ω_{sd}		$1.88 \cdot 10^6$
α_1		0.93
α_2		0.81
β		0.12
γ		0.2
δ		0.061
k_0		$1.901 \cdot 10^3$

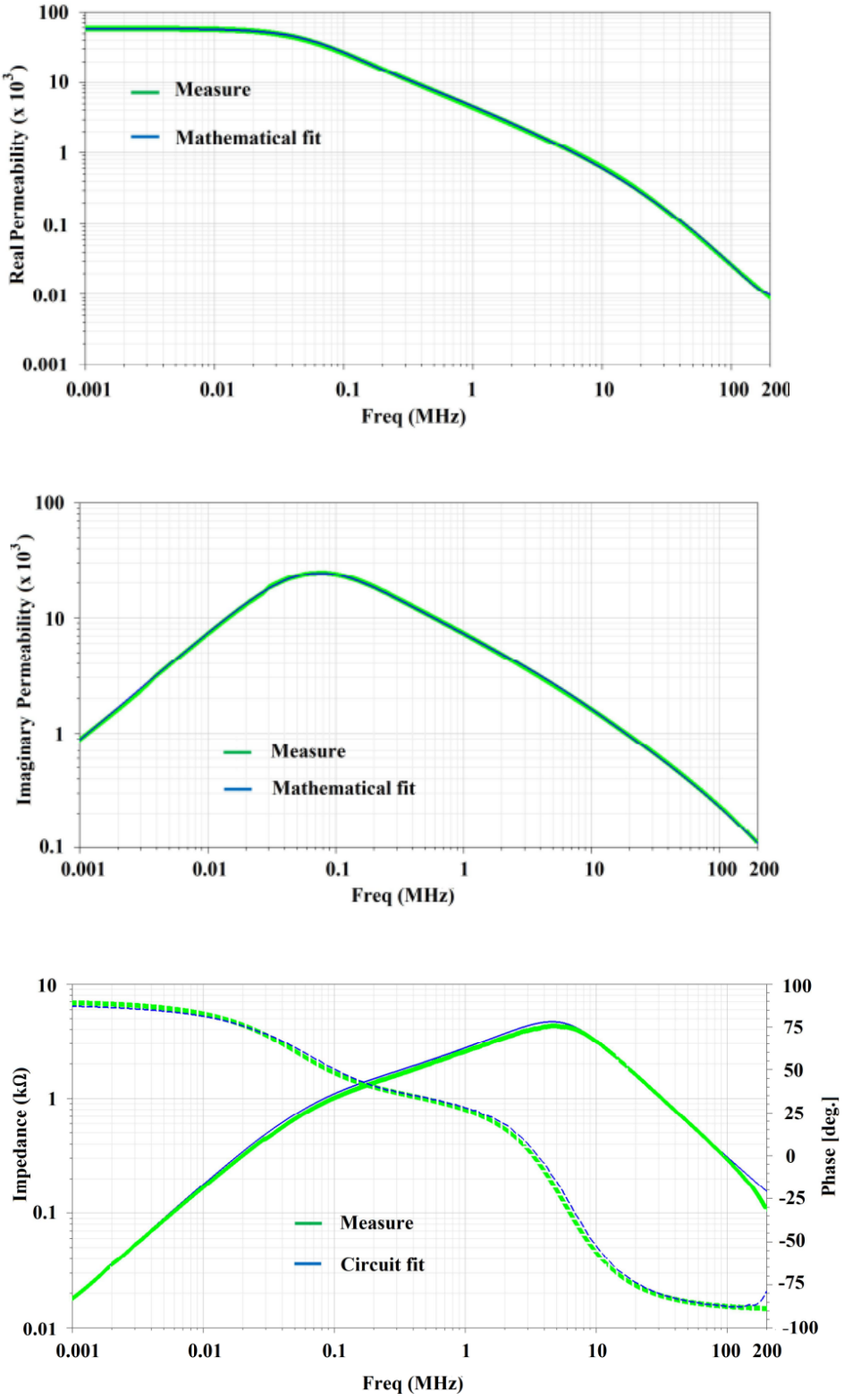

Figure 23: Obtained results from the pole-zero representation of the complex magnetic permeability and the resulting $Z_{CM,}$ [66].

6. Full 3D simulation of a passive HVDC EMI filter

FEM analysis of passive EMI filter component

Needs of Finite Element Method analysis

Differently from a capacitor or a resistor, the CMC is geometrically complex and when the frequency increases much more the geometry plays an important role in the EMI filter performance estimation. In fact, the influence of parasitic becomes dominant at high frequencies.

The EMI filter considered in this thesis is the one illustrated in Figure 24, where a simplified block scheme of the OBC is also reported. Despite the advancements in active EMI filter topologies, in most of the automotive applications, passive filtering still the state of the art. The HVDC filter present a double pi-filter topology composed by two CMCs (custom components), two 3 [μF] and one 4 [μF] X-Capacitors, from MKP1848 Vishay series [72], and six 3.3 [nF] Y-

Capacitors MKP338 6 Y2 series [73], which main characteristics are summarized in Table 6 and Table 7.

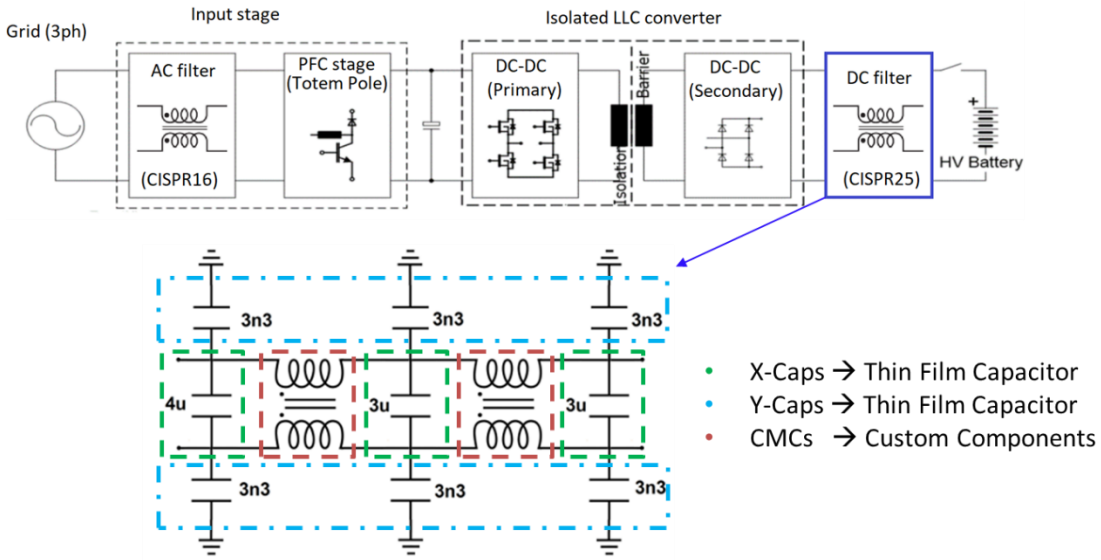

Figure 24: Block scheme of the OBC and equivalent circuit of the HVDC EMI filter.

As reported in previous chapter, HVDC filter is necessary since CISPR25 requirements must be fulfilled to lay down the electromagnetic noise couples on the powertrain of the vehicle or emitted by the cable itself. The output power stage of the OBC is an LLC converter that is well known to be mainly source of CM electromagnetic noise, [25], [26], [28], reaching more than 100 dBµV. This justifies the choice of this topology composed of two cascaded π-filter topologies, for both CM and DM, composed by CMCs and thin-film capacitors.

Table 6: Main electrical and mechanical characteristic of Y-Capacitor, collected from datasheet,[73].

Y-Capacitor	
Capacitance [nF]	3.3
Dimension [mm] (w x h x l)	5 x 10.5 x 10
Rated Voltage [V]	300 AC 1000 DC
Type	Class Y2
Rated Temperature [°C]	85
Capacitance Tolerance [%]	5
Dielectric Type	Polypropylene film
Tanδ (at 10 kHz)	$20 \cdot 10^{-4}$

Table 7: Main electrical and mechanical characteristic of X-Capacitor, collected from datasheet, [72].

X-Capacitor	
Capacitance [µF]	4 3
Dimension [mm]	18 x 28 x 32
(w x h x l)	21 x 31 x 32
Rated Voltage [V]	1200
Type	DC-Link
Rated Temperature [°C]	85
Capacitance Tolerance [%]	5
Dielectric Type	Polypropylene film
Self-inductance	< 1 nH per mm of lead spacing
ESR [mΩ]	14.5
(from 10 kHz to 100 kHz)	11
Tanδ	$40 \cdot 10^{-4}$
(at 10 kHz)	

The realized filter has been characterized through VNA measure and then compared with the schematic simulation. The schematic of the filter is reported in Figure 25, where each block is the broadband model of the component as.s4p or SPICE. From the reported schematic DM and CM attenuation curves are reported in Figure 26 and Figure 27 respectively.

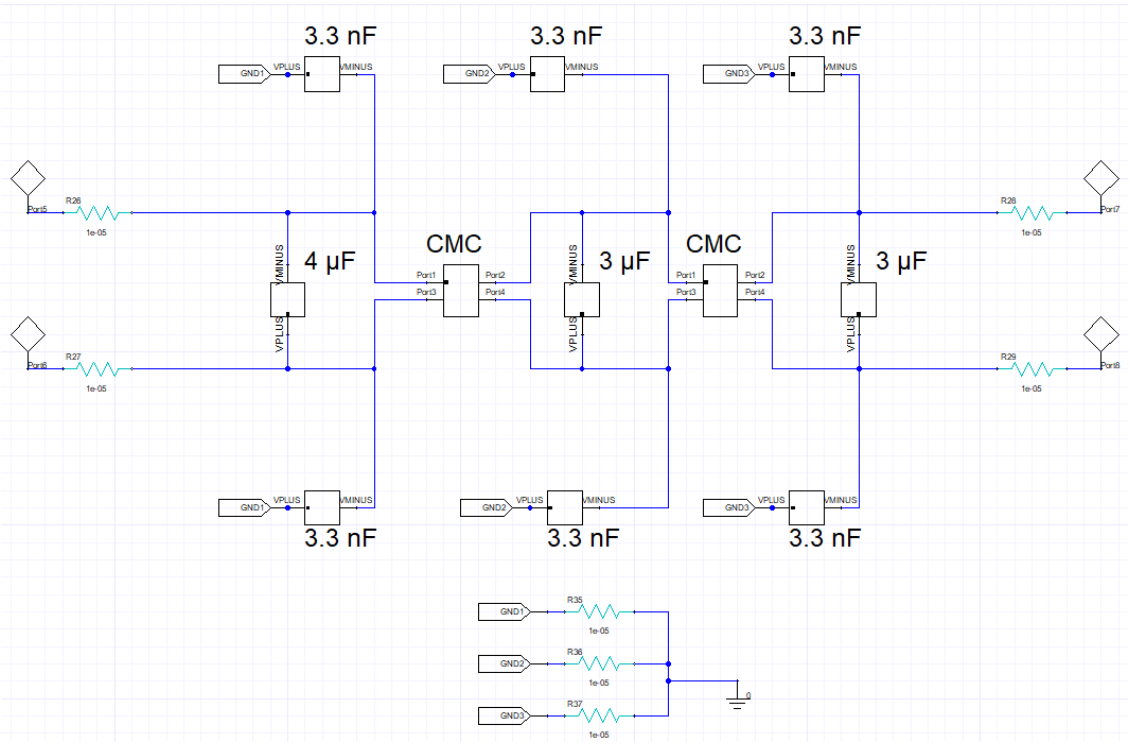

Figure 25: HVDC EMI filter scheme composed by SPICE model of capacitor and .s4p file of the CMC obtained by the model from [66].

From the comparison it is possible to see how schematic simulation predicts the behavior of the filter in terms of CM and DM attenuation up to 300 kHz and 2 MHz respectively. Noticeable the mismatch from 20 MHz above is due to the non-idealities of the isolation transformer used for DM connection of the filter

board to the VNA and the “noisy” measure due to dynamic limitation of the instrument itself.

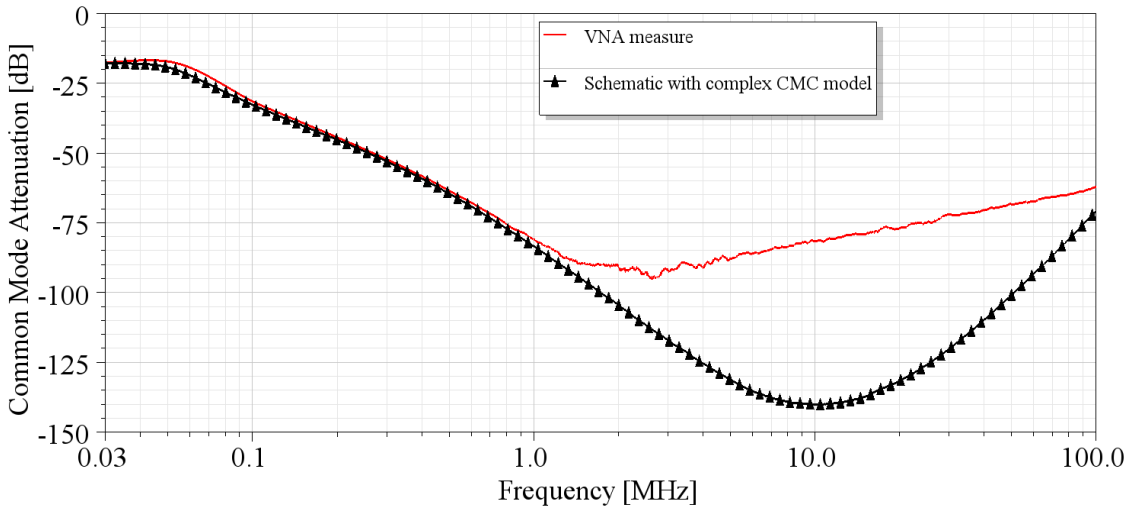

Figure 26: Comparison between VNA measured and simulated CM Attenuation. Matching between schematic and real filter can be achieved up to 2 MHz.

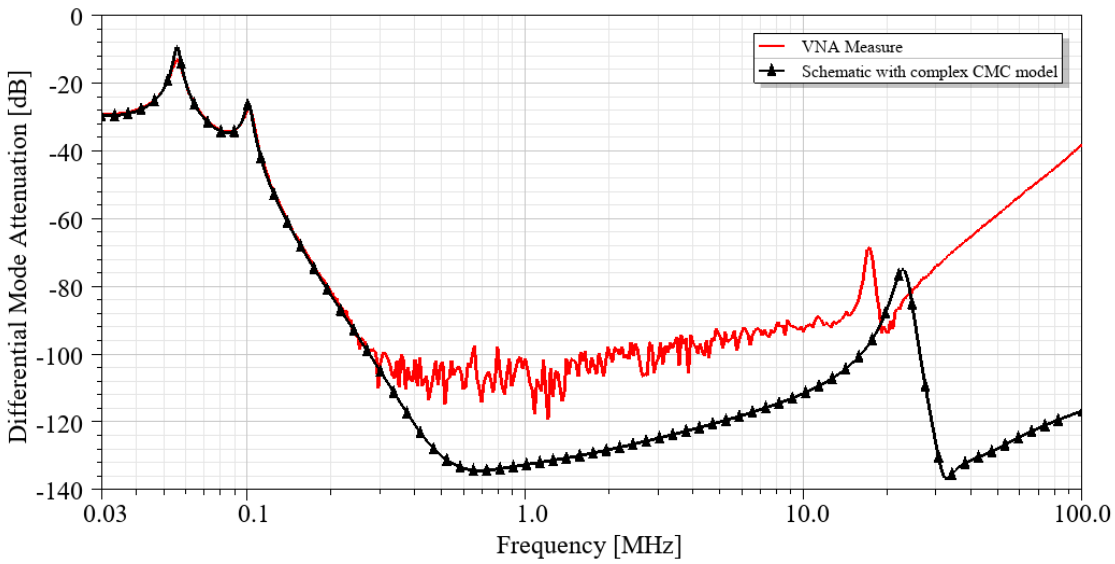

Figure 27: Comparison between VNA measured and simulated DM attenuation. Matching between schematic and real filter can be achieved up to 300 kHz.

Thin-film capacitor model

As well as for the CMC, also the capacitors must be modeled in a 3D way. Capacitors present a simpler structure with respect to CMCs and several models has been developed in [74], [75] literature. But why the capacitor needs to be represented in a 3D way? In Figure 28, the comparison between 3D and RLC model of a 4 µF thin-film capacitor is reported; it can be noticed how they behave in a same way from an impedance point of view.

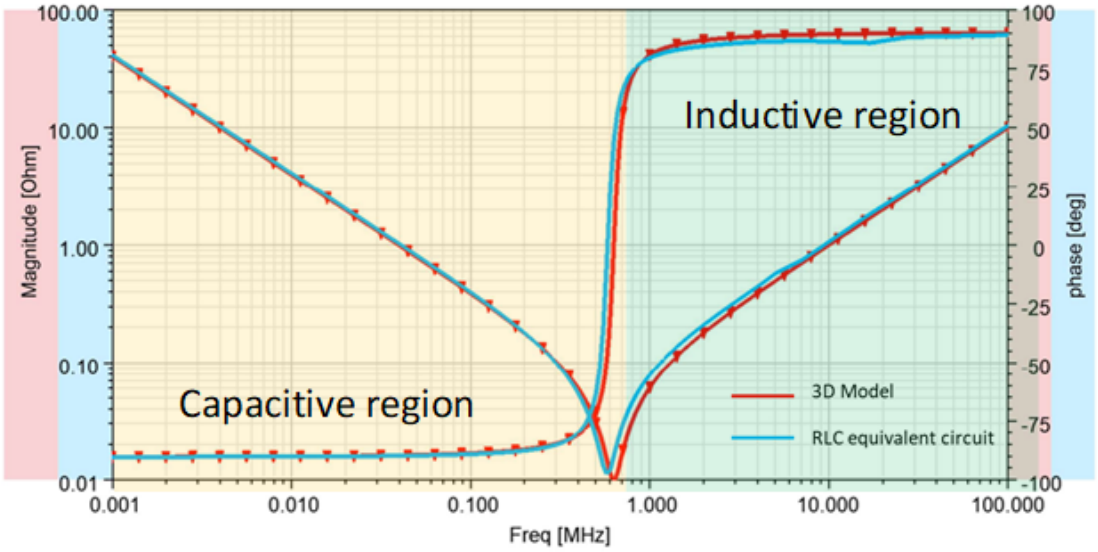

Figure 28: Impedance comparison between RLC and 3D model of 4 µF Thin-film capacitor.

The reason behind the choice of a 3D model is behind the inductive behavior of the capacitor above the resonant frequency. Indeed, the current that pass through the capacitor form a loop inductance; this stray inductance emits magnetic fields that could be coupled on adjacent components becoming a possible issue for the EMI electromagnetic noise rejection. To include near field

effects and represent a real situation, the model reported in Figure 29 has been developed, PEEC based [74], [75], [76], [77], [78], [79], [80].

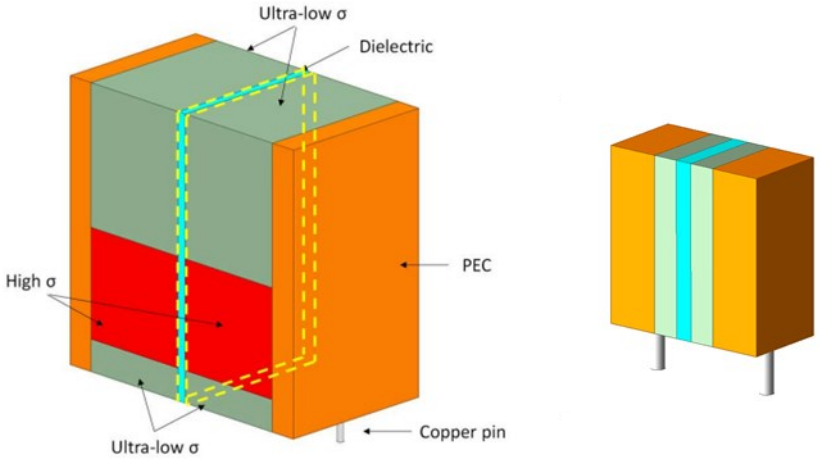

Figure 29: 3D model for HFSS of the X-Capacitor (left) and Y-Capacitor (right).

X-Capacitor model is constituted by a parallel plate structure (constituted by PEC) with a dielectric material placed between them, representing the nominal capacitance value. Between the PEC and the dielectric, two different conductive materials have been added. The difference in terms of conductivity allows to represent the current path inside the capacitor and tuning the position at which the high conductivity material is placed tunes the stray inductance values increasing or decreasing the total current loop area. This model is able to represent the interaction between adjacent components thanks to the stray magnetic field induced by itself. In Figure 30 the magnetic field of the modeled capacitor at 100 kHz and 1 MHz is reported as an example. From the image it is possible to observe how the magnetic field is higher close to the pin, meaning that the usage of more complex structures is not necessary and will slow down simulation speed.

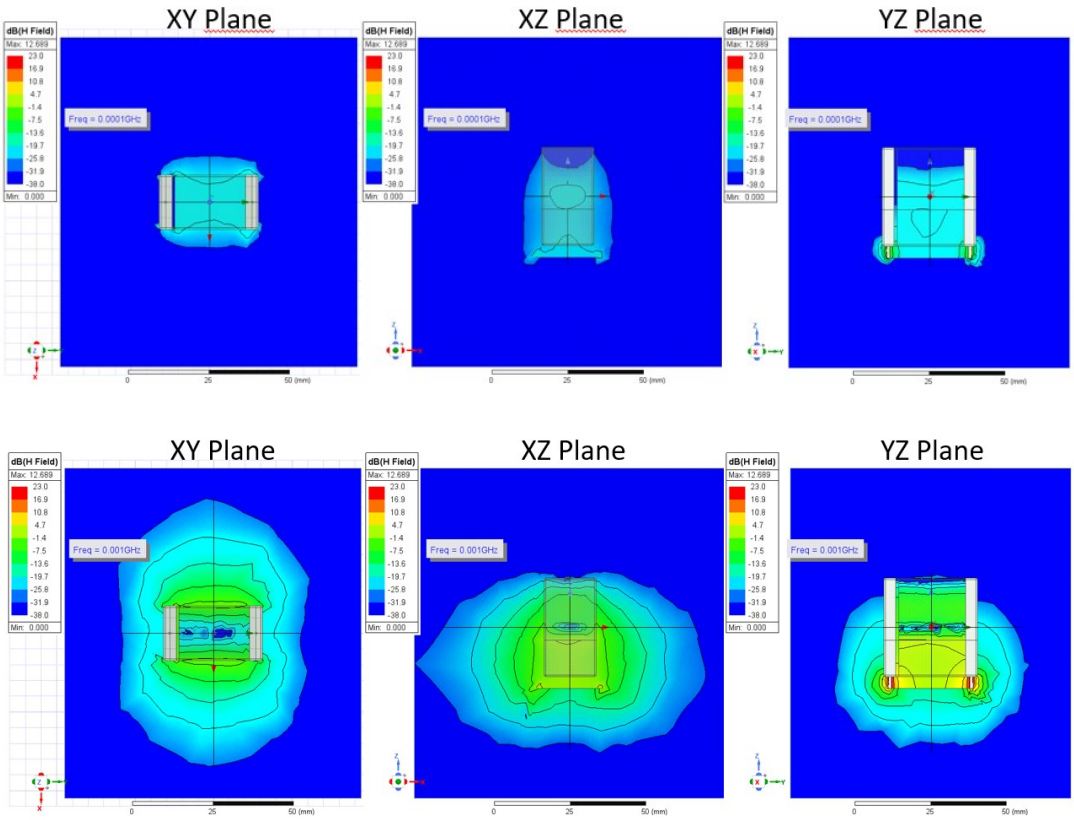

Figure 30: H-Field emission from the 3D model of the X-Capacitor at 100 kHz (top) and 1 MHz (bottom) on XY, XZ and YZ plane.

For Y-Capacitor, the model differs with respect to X-Capacitor one since the representation of the parasitic inductance can be achieved easily without the usage of the conductive blocks, mainly due to smaller physical dimensions.

SMD damping resistor model

Resistors are the easiest component to be modelled on. Impedance of SMD resistors can be obtained through RLC equivalent circuit but in some cases, it could be necessary to evaluate their performance through 3D analysis. The structure is very simple and is constituted by two metallic terminals and a bulk

body at which the conductivity of the material is applied. An example of a SMD resistor structure is reported in Figure 31.

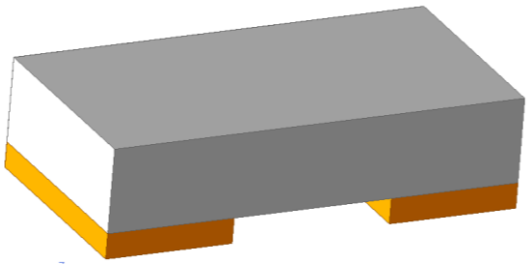

Figure 31: 3D model of a SMD resistor.

Due to their small dimensions' SMD resistors can also be represented in full wave simulators, like HFSS, as a simple 2D structure at which an RLC boundary condition is applied. In practice, at the sheet all the properties of the resistor are applied in terms of its own resistance, parasitic inductance and parasitic capacitance indicating also the current flow direction. From a geometrical point of view, its own dimension can be neglected, reducing it as a 2D structure, as shown in Figure 32, where also the "Lumped RLC Boundary" panel is reported.

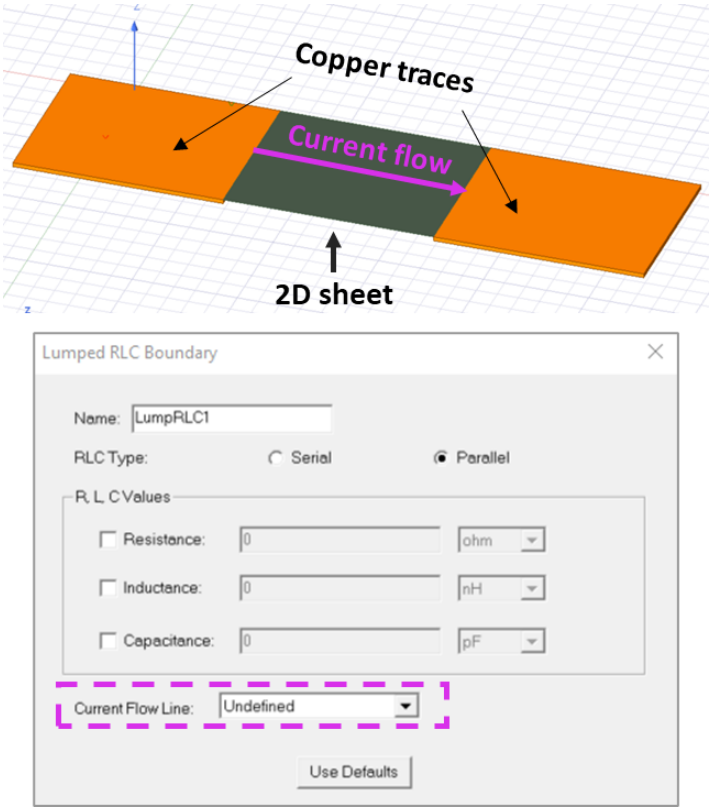

Figure 32: Alternative model for SMD resistor through RLC boundary condition applied on a 2D structure and HFSS dedicated panel.

Common Mode Choke 3D model

To accurately reproduce the performances of the CMC in the surrounding environment, it is necessary to pass through a full 3D simulation. The starting point for the modelling is the knowledge of the core complex magnetic permeability characteristic that determines the CM performance of the component. The complex magnetic permeability, if not reported into datasheets, can be extracted through measurement using a VNA or an LCR meter whenever a physical sample of the core in available. Several extraction methods can be found in literature. By wounding a single turn on the core, it is possible to extract the frequency dependent impedance, from which imaginary and real part of the complex magnetic permeability can be calculated as:

$$\mu_r(f) = \mathrm{Im}\{Z_c(f)\} \cdot \frac{\Re_0}{2\pi f}$$

$$\mu_{im}(f) = \mathrm{Re}\{Z_c(f)\} \cdot \frac{\Re_0}{2\pi f}.$$

Z_C is the single turn impedance whereas $\Re_0$ is the normalized reluctance with respect to permeability and for a toroidal core can be expressed as:

$$\Re_0 = \frac{l_M}{A_c}$$

l_M is the average magnetic path length instead A_C is the magnetic core cross-section. Magnetic path length can be expressed in terms of the geometry of the core due to its dependencies on the external and internal diameter, without

considering the plastic case that protects the magnetic material. Details are illustrated in Figure 33.

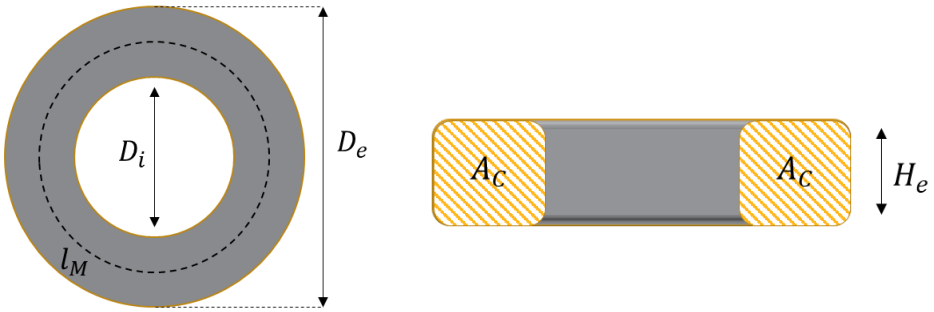

Figure 33: CMC magnetic core geometry and main parameter: external diameter (D_e), internal diameter (D_i), core height (H_e), mean magnetic path length (l_M) and cross-section (A_C).

Magnetic path length can be expressed as:

$$l_M = \frac{\pi(D_e - D_i)}{\ln\left(\frac{D_e}{D_i}\right)}$$

Instead, the magnetic cross section is expressed as:

$$A_C = H_e \cdot \frac{D_e - D_i}{2}$$

So, the reluctance can be rewritten as:

$$\Re = \frac{l_M}{\mu_0 \mu_r A_C} = \frac{2\pi}{\ln\left(\frac{D_e}{D_i}\right)\mu_0 \mu_r H_e}$$

And knowing that $L = N^2/\Re$ and $Z_L = j\omega L$

$$Z_L = \frac{j\omega \cdot N^2 \cdot \mu_o \mu_r H_e \cdot \ln\left(\frac{D_e}{D_i}\right)}{2\pi}$$

$$Z_L \xrightarrow{\mu_r(f)=\mu_{RE}(f)-j\mu_{IM}(f)} \begin{cases} \text{Real}\{Z_L(f)\} = \dfrac{\omega\mu_0 N^2 \mu_{IM}(f) \cdot H_e \cdot \ln\left(\frac{D_e}{D_i}\right)}{2\pi} \\ \text{Imag}\{Z_L(f)\} = \dfrac{\omega\mu_0 N^2 \mu_{RE}(f) \cdot H_e \cdot \ln\left(\frac{D_e}{D_i}\right)}{2\pi} \end{cases}$$

From which

$$\mu_{RE}(f) = \frac{2\pi \cdot \text{Imag}\{Z_L(f)\}}{\omega\mu_0 N^2 \cdot H_e \cdot \ln\left(\frac{D_e}{D_i}\right)} = \frac{2\pi \cdot |Z_L(f)| \cdot cos\{phase\{Z_L(f)\}\}}{\omega\mu_0 N^2 \cdot H_e \cdot ln\left(\frac{D_e}{D_i}\right)}$$

$$\mu_{IM}(f) = \frac{2\pi \cdot \text{Real}\{Z_L(f)\}}{\omega\mu_0 N^2 \cdot H_e \cdot \ln\left(\frac{D_e}{D_i}\right)} = \frac{2\pi \cdot |Z_L(f)| \cdot sin\{phase\{Z_L(f)\}\}}{\omega\mu_0 N^2 \cdot H_e \cdot ln\left(\frac{D_e}{D_i}\right)}$$

From the two formulas it is possible to see how *N* affects the estimation of the impedance for magnetic permeability extraction. In fact, if *N* is equal to 1 the measurement bandwidth extends at the maximum with the minimal parasitic effect due to turn-to-core capacitance.

Defining *k(f)* as:

$$k(f) = \frac{2\pi \cdot |Z_L(f)|}{\omega\mu_0 N^2 \cdot H_e \cdot \ln\left(\frac{D_e}{D_i}\right)}$$

Real and imaginary part of the complex magnetic permeability could be simplified as follows:

$$\mu_{RE}(f) = k(f) \cdot \sin\{phase\{Z_L(f)\}\}$$

$$\mu_{IM}(f) = k(f) \cdot \cos\{phase\{Z_L(f)\}\}$$

As stated before, if the value of *N* increases higher the effects would be introduced by parasitic capacitances. The system would behave as an RLC circuit with a typical resonance frequency. In Figure 34 it is possible to observe these effects. Increasing the number of turns, parasitic capacitance increases and the resonant frequency shifts at lower frequencies.

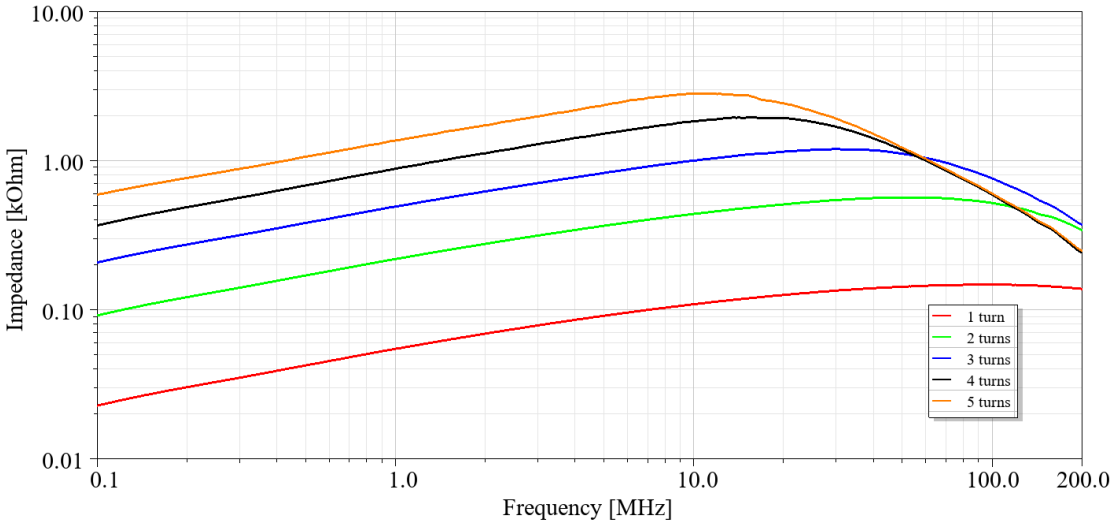

Figure 34: VNA measure of impedance change in terms of number of turns, N. Increasing N resonant frequency shift at lower frequency due to parasitic capacitance, affecting the core parameter extraction.

An example of a complex magnetic permeability extraction, through the method described before, is reported in Figure 35.

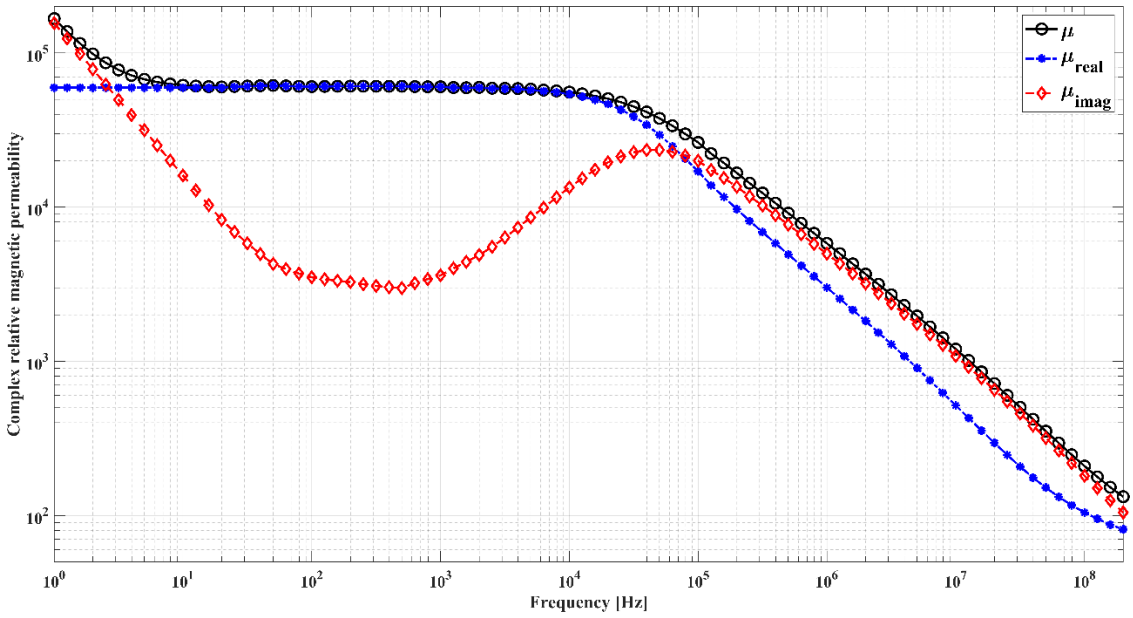

Figure 35: Example of complex magnetic permeability extracted by 1-turn measure of a nanocrystalline core material.

As soon as the complex magnetic permeability has been extracted, the value of the magnetic loss tangent can be calculated as the ratio between the imaginary part and the real part of the magnetic complex permeability. Magnetic loss tangent figure of merit is important to evaluate core losses. Traditionally, the contributions to the losses on magnetic materials are classified as: eddy current loss, hysteresis loss and residual loss. In CMC core typically soft-magnetic material such as nanocrystalline alloys are used which have high coercivity, low remanence magnetization, high flux capabilities enabling manufacture of smaller and more broadband devices. Nanocrystalline cores are wounded as a "toilet paper" and its layer is composed by approximately ¾ of nanocrystalline material and ¼ by dielectric material that behaves like an insulator between adjacent layers. The core has been characterized obtaining the real part and the imaginary part of the complex magnetic permeability; the real part of the

complex permeability and the magnetic loss tangent from 30 kHz to 200 MHz has shown in Figure 36.

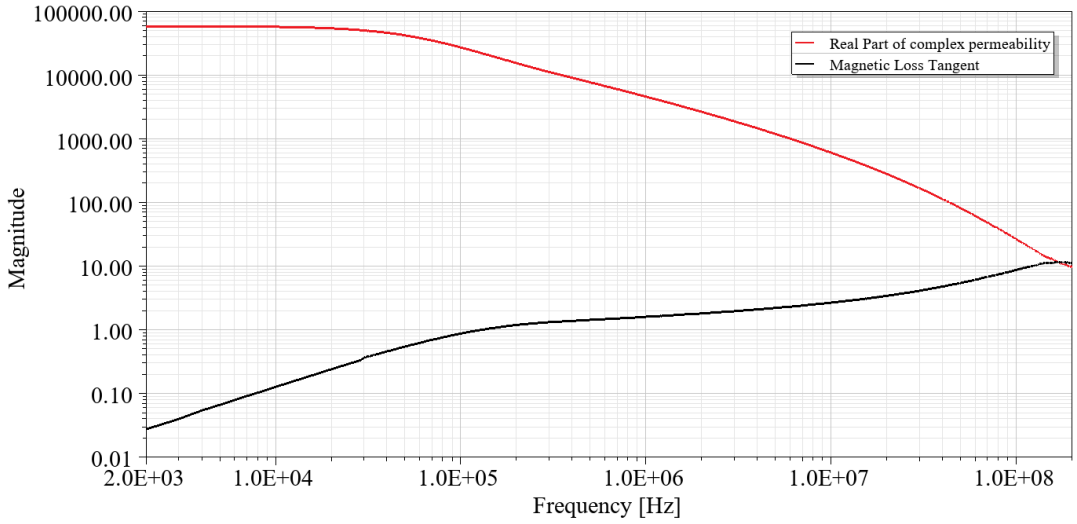

Figure 36: Real part of magnetic permeability and calculated Magnetic Loss Tangent of the CMC core.

From [81] and looking at some datasheets, the conductivity of the material is roughly 1 μΩ·m and the dielectric permittivity is around 3.3. Since dielectric permittivity and conductivity are not negligible, it must be included in simulations and added inside the parameter of the core.

Despite the strong dependencies of the core material, another important aspect is the geometry of the CMC and the surrounding environment. How the CMC is wounded determines the parasitic capacitance in both CM and DM impedances; nevertheless, the usage of thermal interface material (TIM) and the vicinity of metallic structure or other component influence the behavior of the CMC. The influence of the metallic enclosure on components has been evaluated at EMI filter level and reported in the next sections.

Once the characteristics of the core are available, the structure of the CMC has been modeled accurately trying to consider as much as possible the real geometries of the component. The 3D structure is composed of the core (considered as a bulk ferrite, according to [71] and [82]) and its plastic case, two coils each one composed by six turns and the FR4 support used to keep in place the pins of the component, as shown in Figure 37.

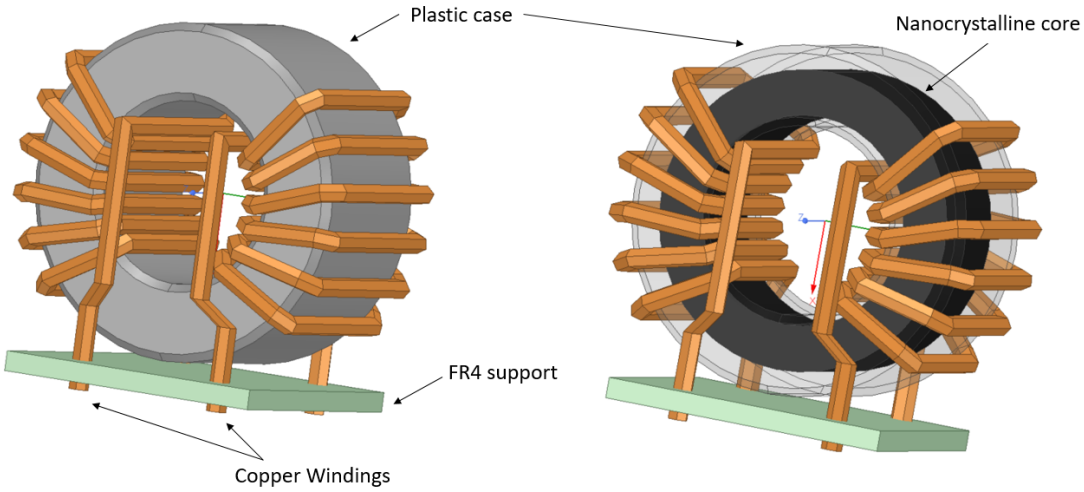

PART		VALUE
External plastic case diameter	$D_{ext,pl}$ [mm]	33.5
Internal plastic case diameter	$D_{int,pl}$ [mm]	18.5
Plastic case depth	w_{pl} [mm]	18
External core diameter	$D_{ext,core}$ [mm]	29.2
Internal core diameter	$D_{int,core}$ [mm]	20.4
Core depth	w_{core} [mm]	14
Wire diameter	d_{wire} [mm]	2
Number of copper wire turns	*N [turns]*	6×2

Figure 37: 3D model of the 2-wire CMC with main mechanical characteristic. The structure presents the two windings, the core with plastic case and FR4 support,[76].

For each 3D object, the material properties have been assigned through the library present in HFSS. After that excitation ports, reference plane with infinite conductivity and a box with radiation boundary have been applied, in order to confine the solving region speeding up the simulation. As a result of the simulation a touchstone file of the four-port network is obtained, from which Z_{CM} and Z_{DM} can be extracted following the connection scheme reported in previous chapter. Another way to obtain impedance values is to add the connection directly on the 3D model, achieving same results.

Simulation results are reported in the Figure 38 for Z_{CM}, where the comparison between simulations and measure can be appreciated. The figure shows the necessity to tune the total parasitic capacitance seen in CM configuration by acting on the turn-to-turn distance.

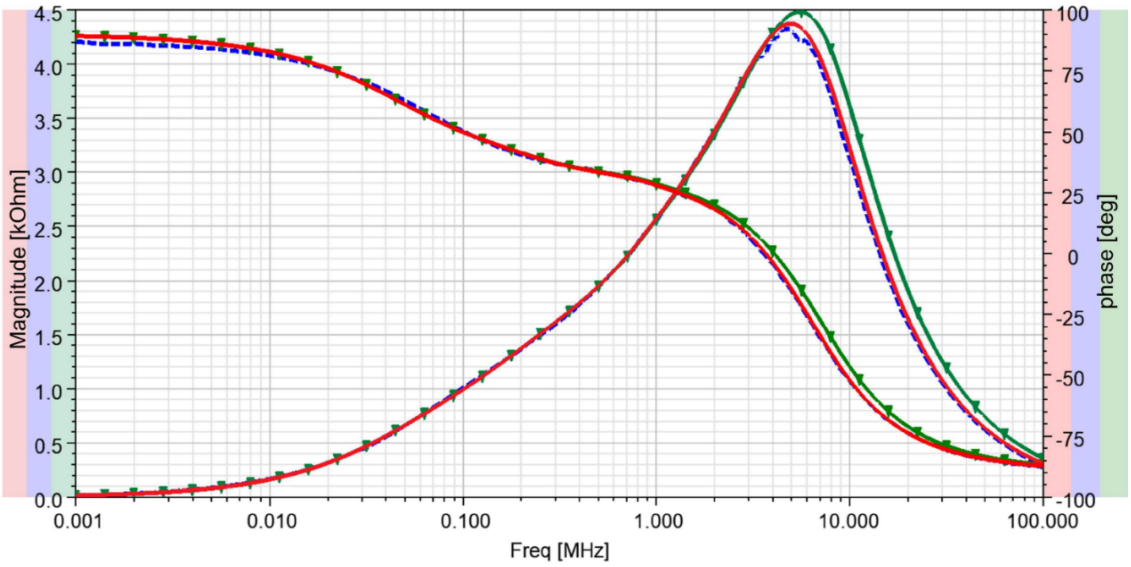

Figure 38: Comparison between VNA measure (blue dashed line), HFSS simulation without parasitic capacitance fine-tuning (green solid line) and the matched one (red solid line),[76].

In figure, Z_{CM} has been matched by modifying the winding distance. Winding distance affects directly parasitic capacitance: increasing it, relies on a shift of the resonance frequency of 500 kHz. Since Z_{CM} has been matched also Z_{DM} has been evaluated and reported in Figure 39.

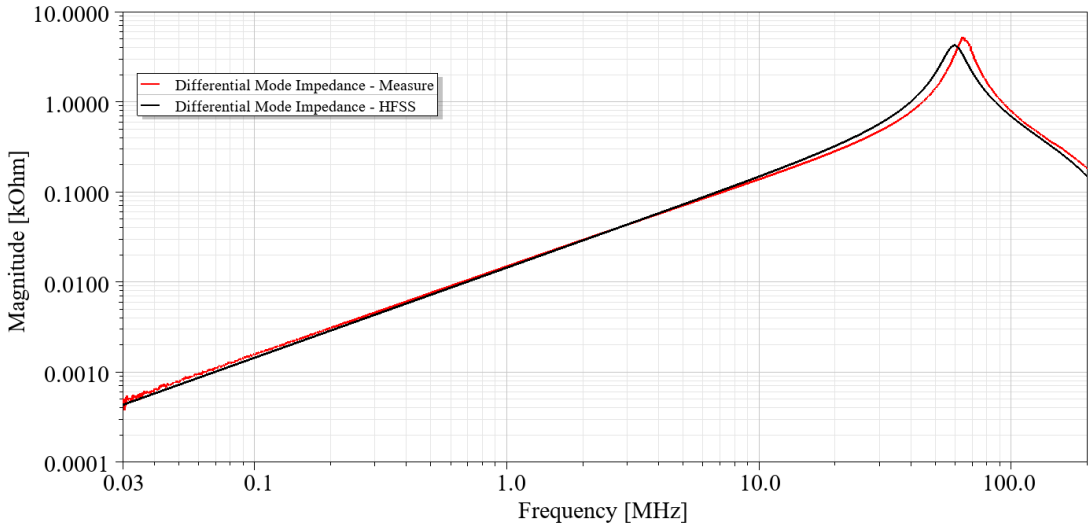

Figure 39: Comparison between VNA measure and HFSS simulation of Z_{DM}.

EMI filter characteristics and model

Since all the passive components are modelled and properly matched, the next step is to import the PCB layout inside HFSS. In order to improve the accuracy of the simulation, PCB layout is as important as components since it can cause unwanted bypass of the filter board or too high parasitic affecting a lot the performance of the filter board. In this case, power supply terminals are designed for the propagation of 800 VDC power. Hence, they are not designed to assure balance at high frequencies and may introduce a significant impedance imbalance leading on electromagnetic noise mode-conversion. Different tools

from Ansys are available to manage PCBs such as HFSS, SIwave and Q3D. The Layout Component (HFSS 3D Layout project inside HFSS 3D) for the PCB has been merged with all the components exploiting ANSYS Mesh Fusion Technology [83]. Thanks to the properties of the tool, is it possible to assign the layout stack-up to the PCB and pour the geometries to speed up the simulation of the filter itself. Vias are also considered due to their impacts in terms of parasitic inductance, especially when are used to connect Y-capacitors to earth.

The integration of the PCB with the passive components is reported in Figure 40.

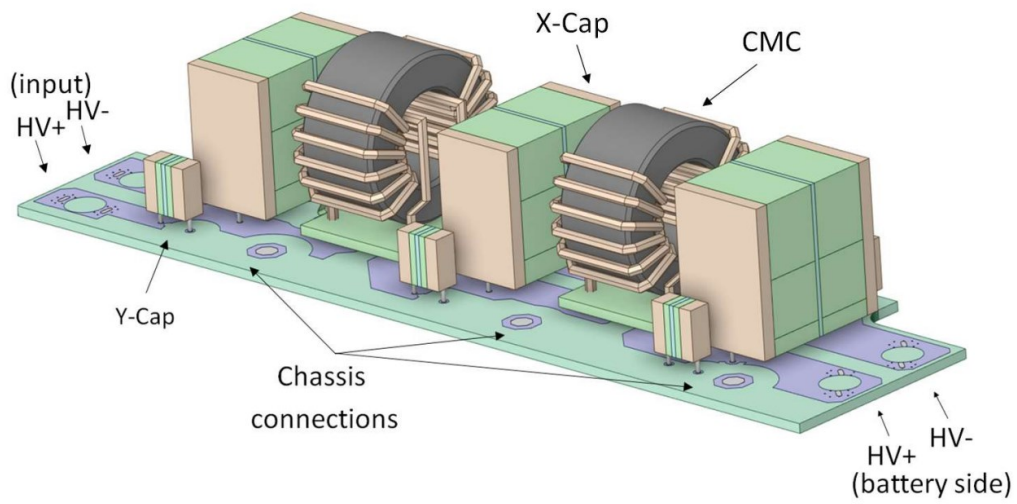

Figure 40: Complete 3D model of the HVDC EMI filter,[76].

Validation of the model

Since all the components and the PCB of the HVDC filter is modelled, the full 3D analysis can be executed in order to extract the DM and CM attenuation curves.

In Figure 41 it is reported the result in terms of CM attenuation compared with VNA measurement.

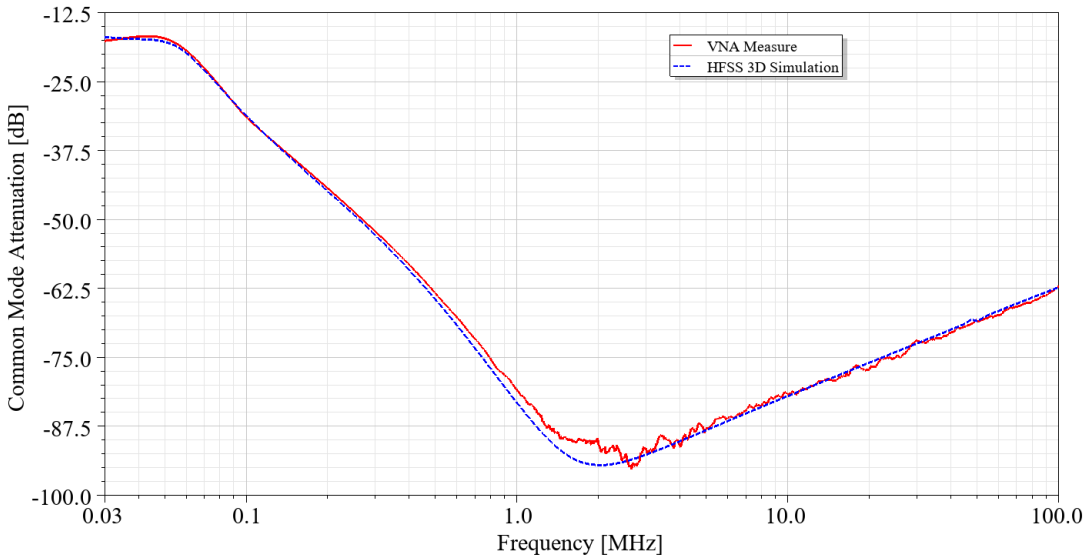

Figure 41: CM Attenuation comparison between HFSS simulation and VNA measure.

Result show a good matching all over the bandwidth with small discrepances around 1-2 MHz due to the instrument dynamic.

In Figure 42 instead the DM insertion loss result is reported compared with VNA measure outside the chassis.

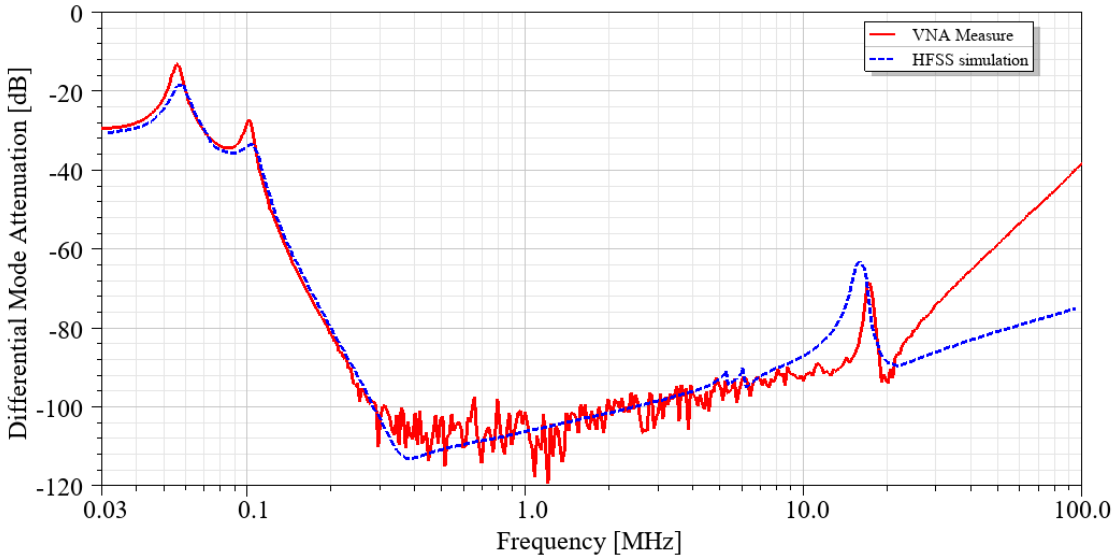

Figure 42: DM Attenuation comparison between HFSS simulation and VNA measure.

In this case the 3D simulation 3 dB mismatch respect measurement from 30 to 300 kHz. Low frequency mismatch can be related to component tolerances, since X-capacitor present ±10% of tolerance instead CMC ±20% due to fabrication. Instead, the mismatch from 20 Mhz above can be related to the non-idealities of the isolation transformer used to inject DM signal. From the Figure, it is also highlighted a resonance at 17 MHz. Resonances can be dumped through resistor placed in series with the Y-cap; for this fiter a damping resistor of 4.7 Ohm was choosen after a parametric analysis, firstly executed at schematic level and reported in Figure 43.

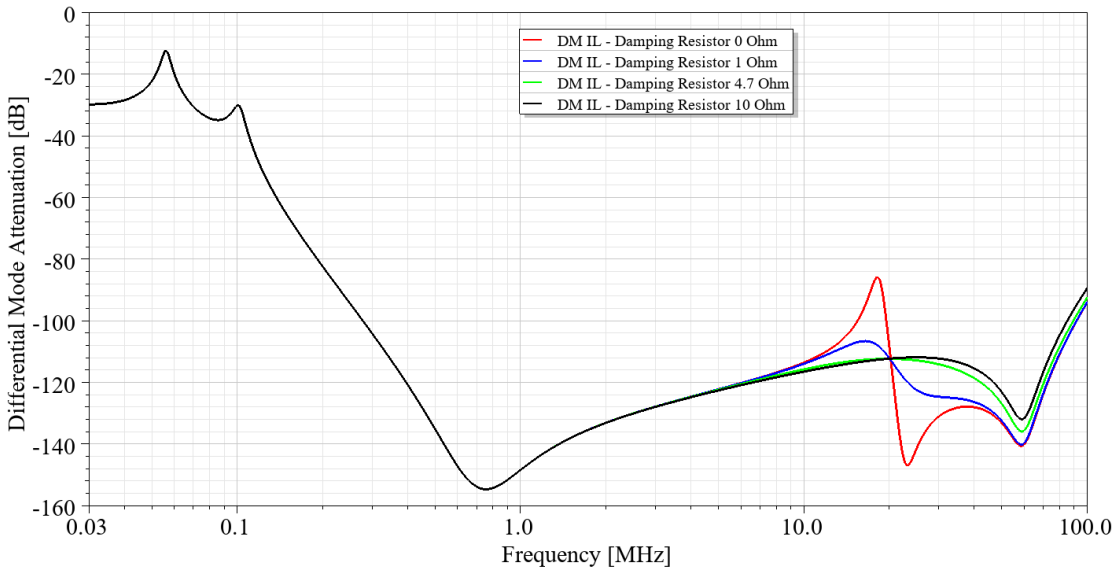

Figure 43: Effect of dumping resistor on DM Attenuation evaluated at schematic level.

Metal chassis impact on filter Insertion Loss

Besides the effect of the chassis on the CM insertion loss, chassis or in general metallic parts shall be considered during the analysis also for DM insertion loss evaluation. Nevertheless, it is better to consider the overall structure of the filter including the Y-capacitor since the lack of symmetry in the circuit can cause mode conversion and affect DM behavior. The structure of the chassis is reported in Figure 44.

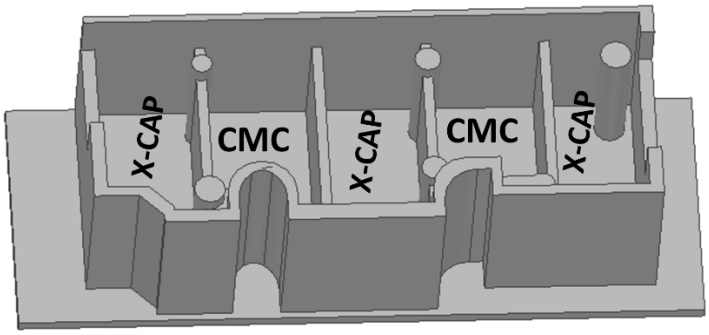

Figure 44: Aluminum housing of the filter. Each component is placed in between two "walls" to contain TIM,[76].

From the mechanical structure it can be notice how, for each passive component, some “wall” has been added in between them for thermal management, mechanical stresses and to enhance component decoupling. Since the filter is rated for a maximum output power of 22kW with current value up to 40 A, a component like CMCs dissipates power due to coils resistance; therefore, the surrounding walls helps to dissipate them as an heatsink through a Thermal Interface Material (TIM). The choice of TIM must be carefully studied. Low dielectric constant materials must be preferred instead of high ones, due to their

strict relation to CMC performance. Since the turn-to-turn parasitic capacitance is an air stray capacitance, TIM would act as a dielectric with a constant different from one. Boosted parasitic capacitance moves the resonance frequency of the CMC both in terms of CM and DM impedance, affecting filter insertion losses. On the other ends lower dielectric constant materials are typically characterized by lower thermal conductivity. TIM density serves as a fixation point for components during mechanical stresses like vibrational and thermal cycles. Summarizing: smaller the dielectric constant lowers the impact from an EMI perspective, reducing thermal performances. From an EMC perspective, the aluminum chassis with walls behaves like a cage for the near field emission. Impinging the aluminum walls, H-field emitted by the nearby component can be reduced by the opposing magnetic field. Since aluminum is not magnetic, its shielding effectiveness is not high. However, it constitutes a good compromise, thinking also about mechanical and thermal management. In Figure 45, the image of the filter inside the housing is reported.

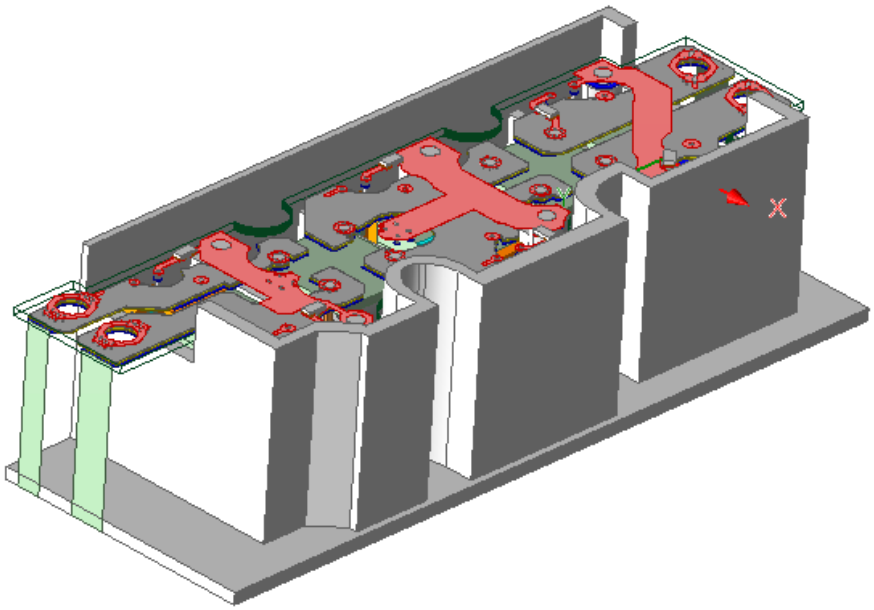

Figure 45: Complete 3D model of the HVDC EMI filter including the aluminum housing,[76].

Interestingly, the DM insertion loss is highly dependent of the surroundig environment. Repeating the measure considering the filter inside the chassis the result shown in Figure 46 has been obtained. As one can observe a rigid shift of the insertion loss is evident. This shift of 25-26 kHz can be related to the effects of the metallic proximity with respect to the CMCs. The obtained results confirm that the presence of the surrounding aluminium chassis affects negatively the DM behavior of the filter, presenting a rigid shift at higher frequencies of the filter attenuation.

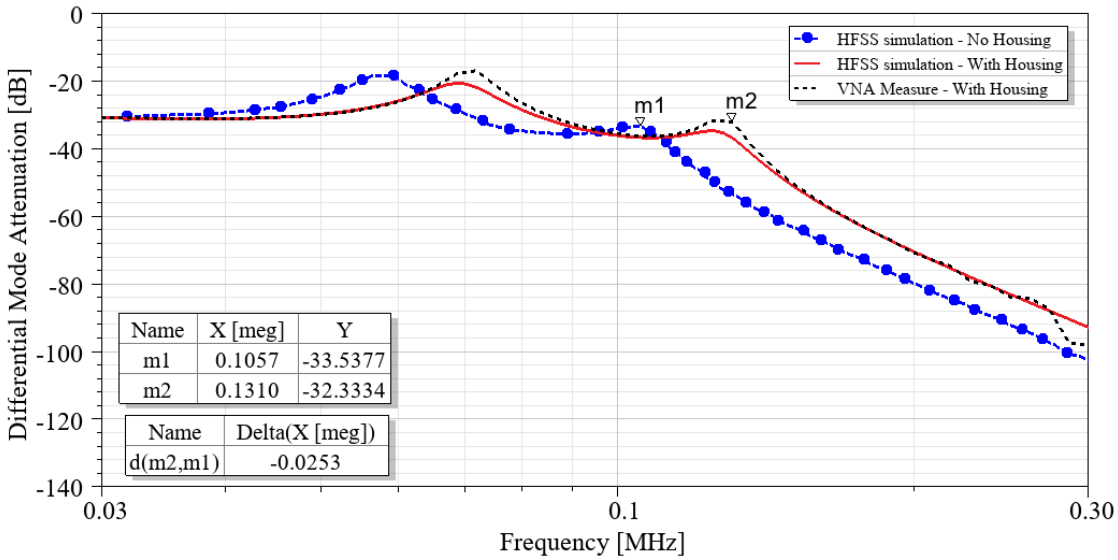

Figure 46: Effect of the housing on DM Attenuation of HVDC EMI filter. Pole-shift of 25 kHz is highlighted.

The obtained result has been validated through a measurement campaign on the CMC. Indeed, since the insertion loss has been obtained through small signal measurements a link between CMC and the filter behavior exists. DM impedance has been taken as measurand, and three different measurements have been conducted changing the surroundings. Firstly, CMC has been measured in air to minimize its interaction with external factors. Then, the CMC has been placed close to a metal surface facing the top of it. Finally, the CMC has been placed inside the aluminum chassis. The results are reported in Figure 47, where the shift of the resonant frequency of DM impedance is clearly proved.

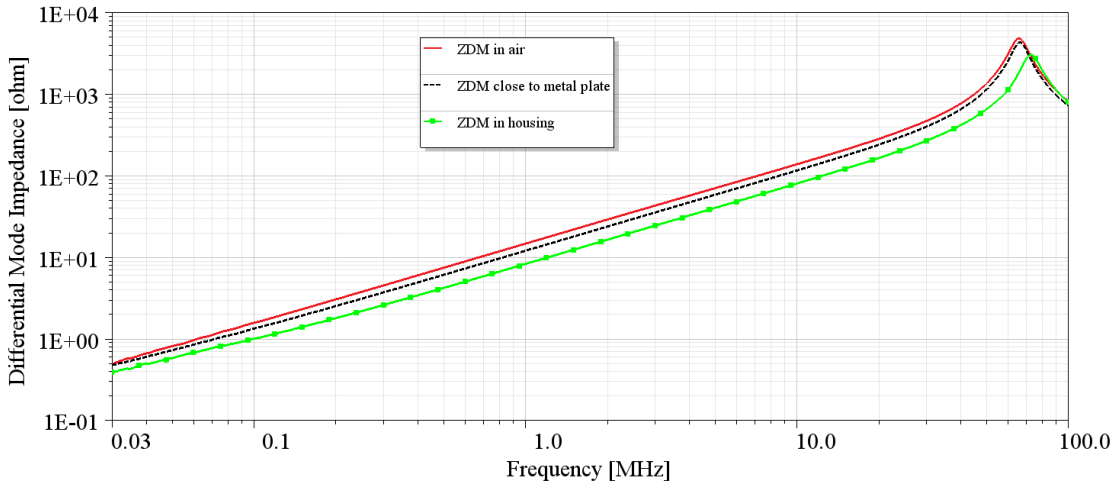

Figure 47: Effect of the proximity of metallic surface on the DM impedance of the CMC.

Additionally, to appreciate the low frequency effects on DM excitation, the induced current on the chassis has been extracted and illustrated in Figure 48. As reported before, the induced current on the chassis interacts with the stray field emitted by the CMC, resulting in a sensible reduction of the total leakage inductance, hence the Z_{DM}.

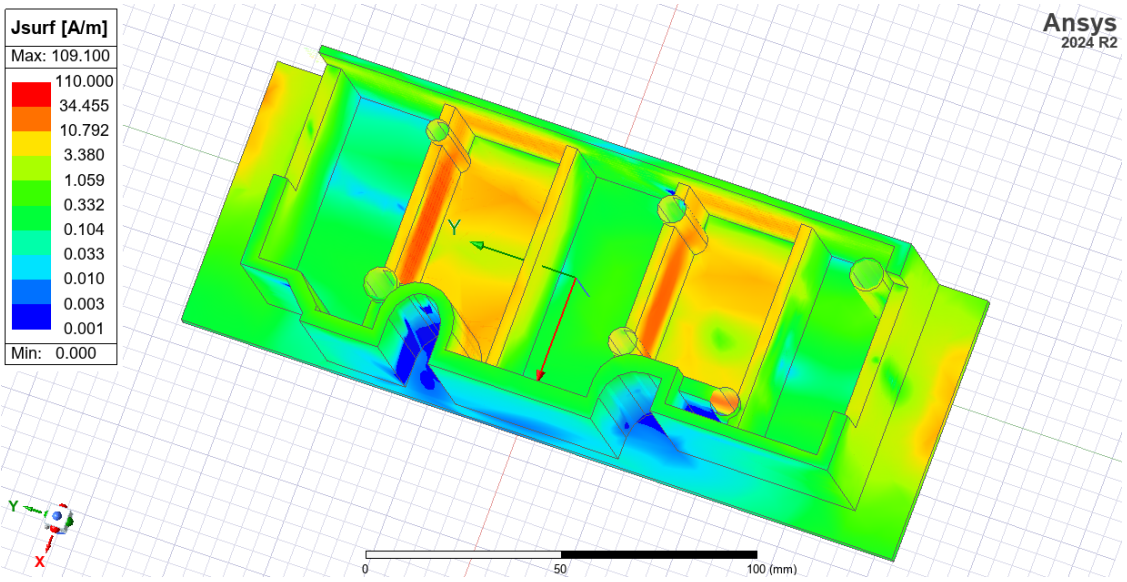

Figure 48: Resulting induced current density on the chassis by DM excitation of the filter. Higher amplitude corresponds to the surface impinged by CMC stray field.

Furthermore, from the electromagnetic simulation of the filter the H-field distribution has been extracted exciting the system with a CM and DM current to understand the behavior including PCB and chassis. The H-field distribution has been obtained by exciting the system with a sinusoidal current source with 100 mA AC amplitude thanks to the link between Ansys Circuit Design and HFSS. Figure 49 shows the resulting H-field distribution at 30 kHz, cutting the filter with a plane along XY, 15 mm above the PCB. In Figure 49 (a) is reported the results from DM excitation and in (b) the results from CM excitation. As expected, the higher amount of stray field is generated by the CMCs, since they are inductive components and dominate at that frequency. When the system is excited by CM currents a lower H-field emission is highlighted. In Figure 50 H-field emission is reported instead along YZ plane, cutting through the filter at its center. It's possible to notice how chassis helps to contain the H-field reducing the electromagnetic interaction among nearby components, and again how the DM excitation results in a higher emission of magnetic field with respect to CM excitation. In Figure 51 H-field variation with respect to frequency is reported; this figure shows how the fields tend to concentrate at the input side of the filter increasing the frequency.

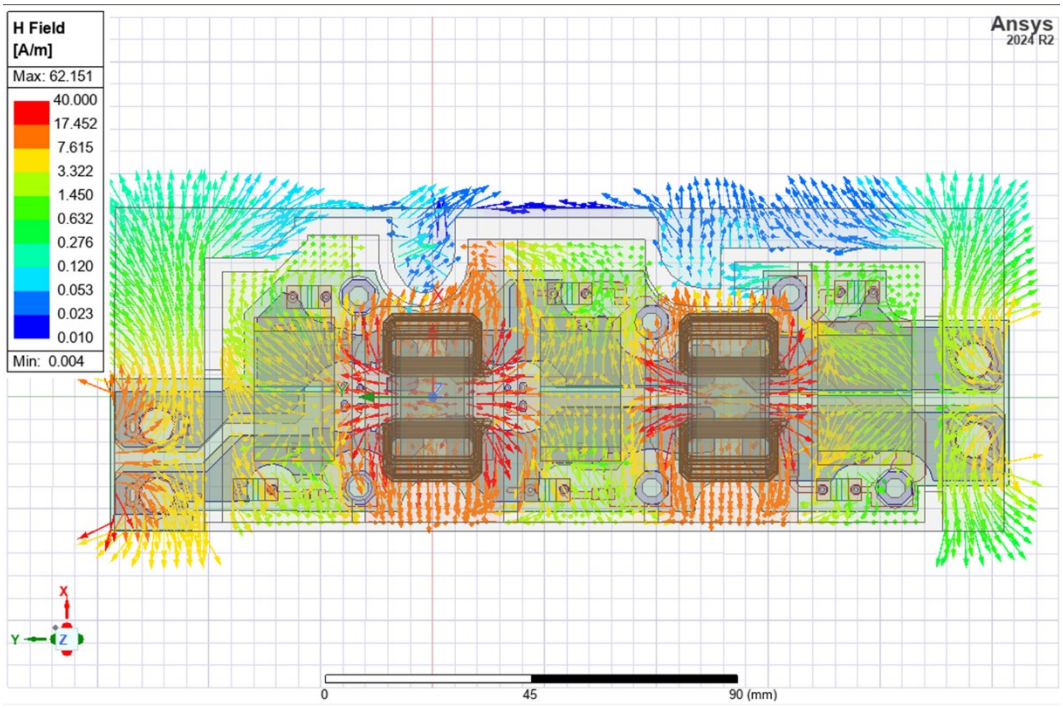

(a)

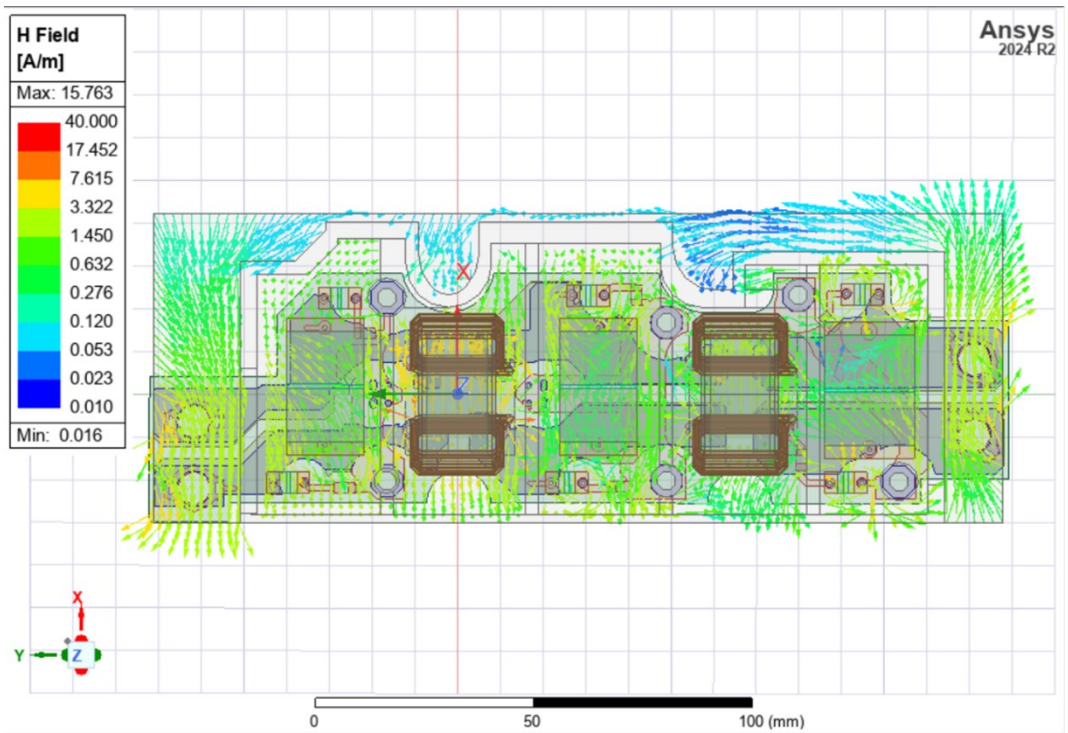

(b)

Figure 49: H field distribution along XY plane: a) DM excitation b) CM excitation.

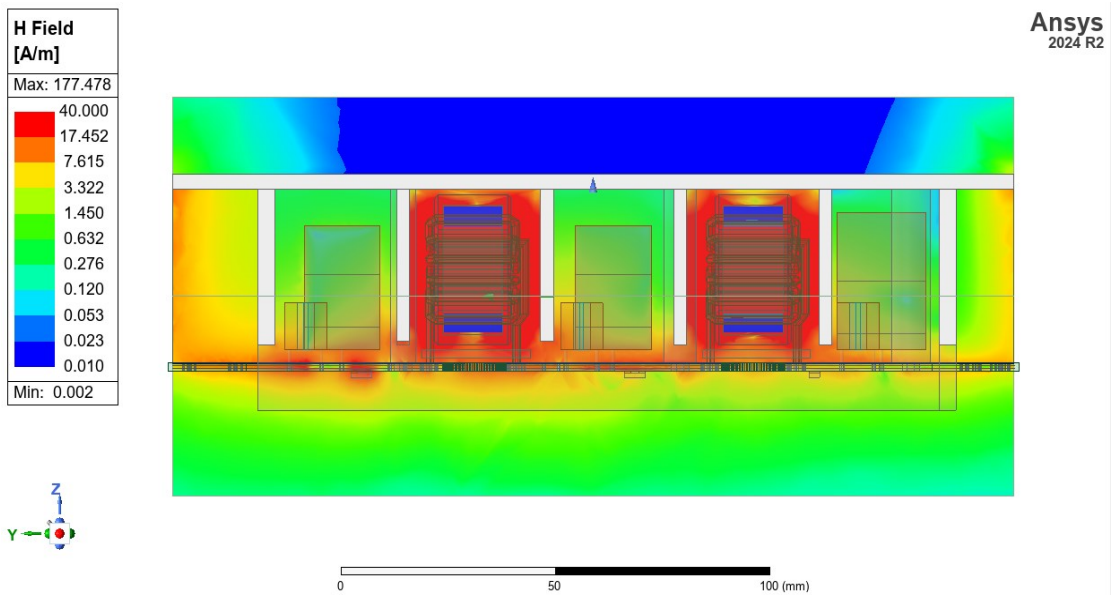

(a)

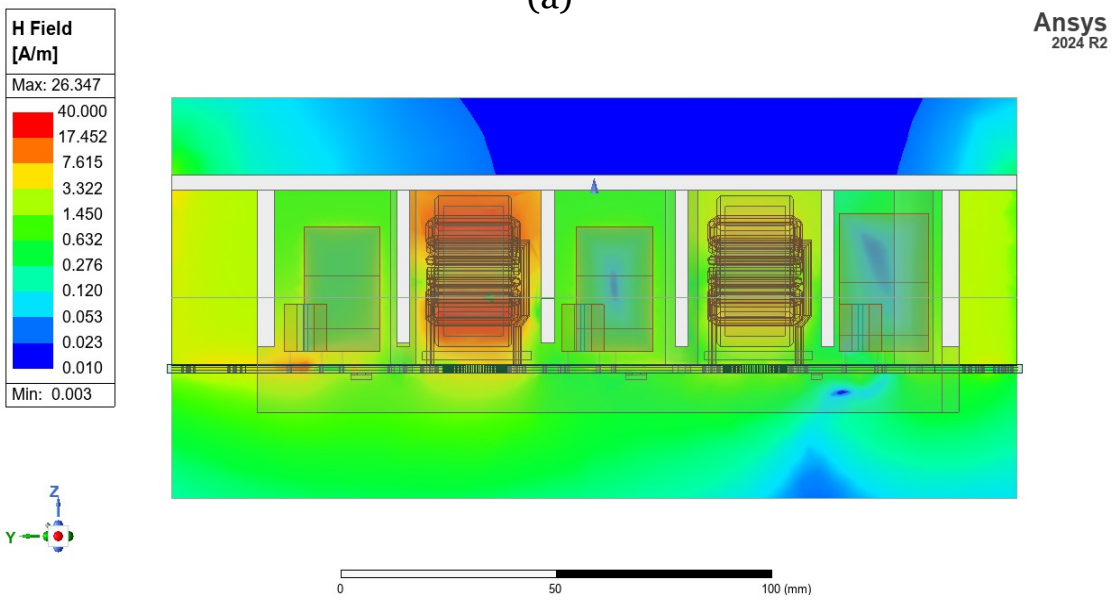

(b)

Figure 50 H-field distribution along YZ direction: a) DM excitation b) CM excitation.

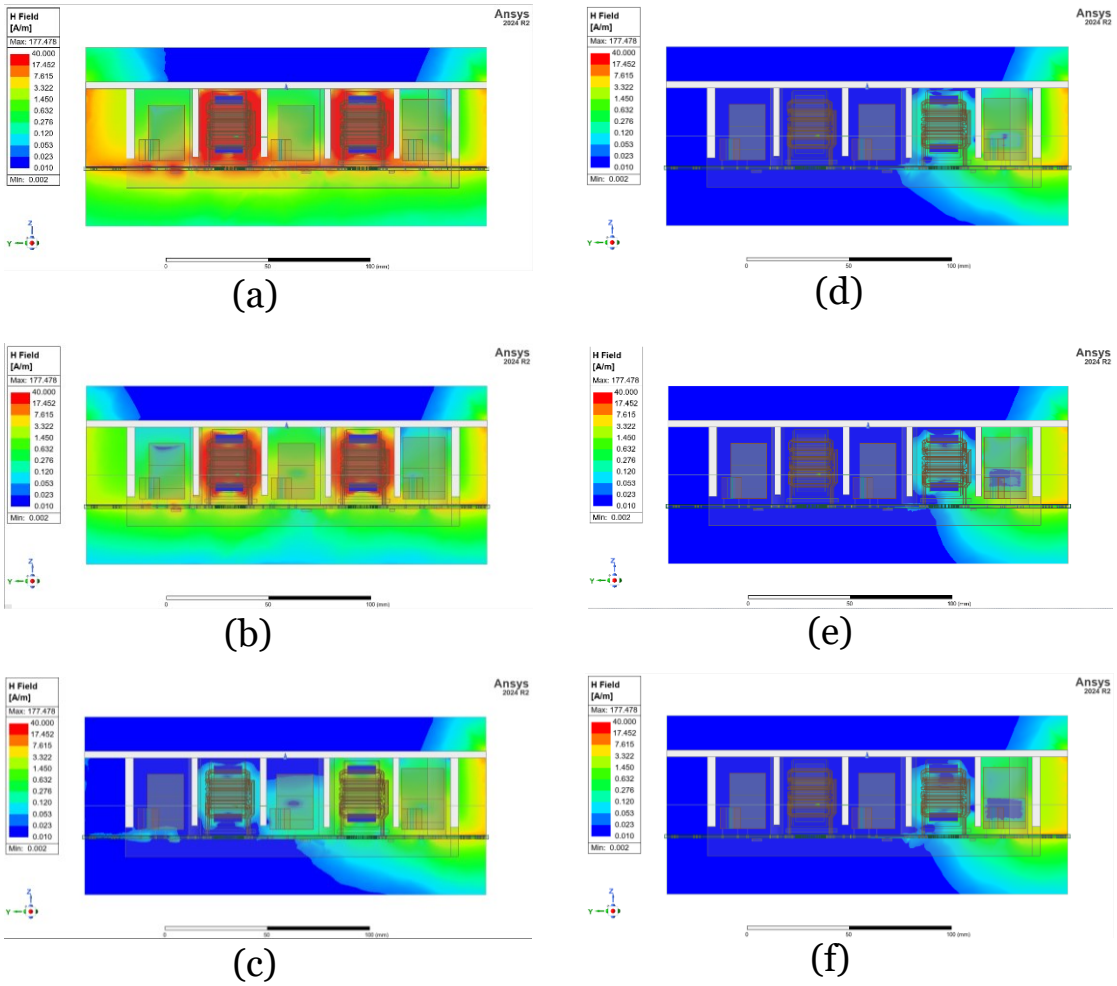

Figure 51: H-field distribution along YZ direction respect frequency: a) 30 kHz b) 100 kHz c) 300 kHz d) 3 MHz e) 30 MHz f) 100 MHz.

7.Conclusion & perspective

General conclusion

In this thesis after a deep introduction of an OBC, starting from its type approval cycle and ending with its own structure, a deep investigation of its HVDC filter and its components has been conducted.

In the first part, a novel SPICE model of CMC has been proposed. The broadband model for two-wires CMCs is suitable for EMI pre-compliance assessment and was developed considering not only the differential and CM impedance, but also other parameters such as phase and inter-winding impedance. Circuital model validity has been validated up to roughly 200 MHz. Furthermore, in this thesis has been showed a new way to fit complex magnetic permeability for nanocrystalline cores, with respect to the conventional Laplace/Debye resonator model, exploiting the introduction of weighted poles and zeros. This allows modelling the CM impedance of CMCs with frequency dependent resistance and inductance building a touchstone model that can be used to evaluate EMI filter performances.

In the second part of this thesis, the complex broadband model of the CMC has been applied for an HVDC filter for a 22 kW OBC. The discrepancies in terms of CM and DM attenuation justify the needs of a full 3D simulation. Full 3D simulation through HFSS of thin film capacitor and CMC has been reported highlighting how, with a precise modelling technique, it is possible to achieve good matching with respect to measure of real system. The overall filter has been simulated considering PCB, Y-cap, X-cap and CMC, showing a good matching between measures. Moreover, the surrounding metal chassis effects have been demonstrated to affects the DM insertion loss of the filter, thus reducing its performance. The CMC DM impedance is affected by the vicinity of metal parts leading to a reduction of attenuation due to a rigid shift of the insertion loss curves, all validated through VNA measurement and replicated at filter level on HFSS.

Perspectives

Since the simulation method is reliable in terms of insertion loss reproducibility, this can be applied to optimize the EMI filter design of complex component like OBCs, extending also this method on different applications such as industrial, household applications etc. The simulative method can be applied on 4 wires CM choke and 3-phase filters. Furthermore, whenever a new HW topology is under development, this simulative method can be inserted inside an iterative analysis which goal is to reach compliance predicting the performance of the filter in an

accurate way just starting from key voltage/current measurement of the first prototype.

Charging Mode Impact on Conducted Emission

Besides studies on EMI filter design and component modeling, numerous problem-solving activities related to OBC were conducted throughout the PhD.

In this section one of the studies conducted is reported. The main problem was related to an unexpected failure in conducted emission on main lines described in [52]. Based on the result from [52], a deep analysis has been conducted and the root cause found. Again, this work shows how combining measures and simulations helps to understand phenomenon and find out solutions.

Starting from the study showed by Camarda et. Al., a radiative coupling has been highlighted between the HV parts, in this case the LLC resonant converter and the LV part that manage the communication between the charging station and the vehicle. This first coupling relies on a second coupling on the main lines throughout Control Pilot and Control Proxy signals. Camarda et. Al. focused on the mitigation of the coupling designing an optimized shield composed by AISI 304 nickel coated. Thanks to the shield, it was possible to reduce the electromagnetic noise by exploiting the absorption and reflection characteristics through the magnetic permeability of the coating.

A step ahead of this job has been conducted since the shield presents high performance variability due to the coating process. The problems arise when the

OBC is tested in Mode 2 using an EVSE to manage the signaling. The results of the conducted emission on main lines is showed in Figure 52, compared with Mode 1.

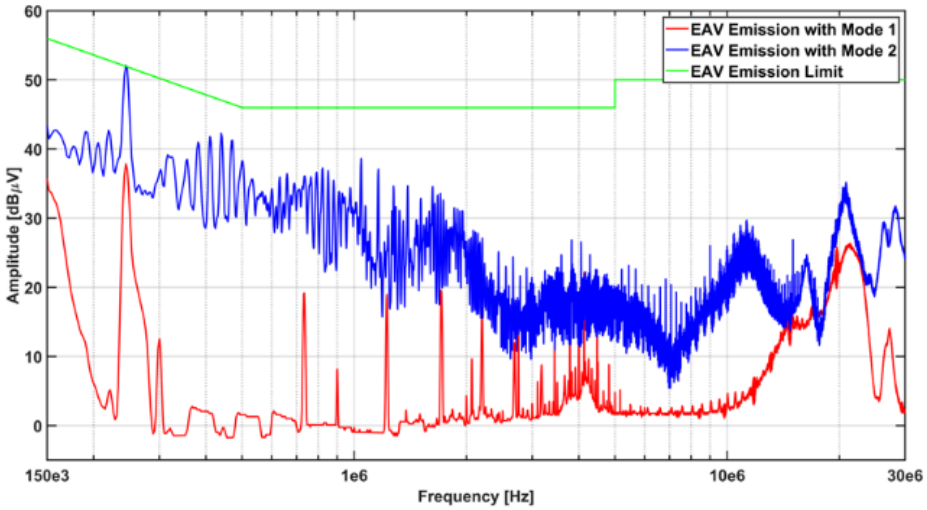

Figure 52: Conducted Emission on Main Lines of a 22kW OBC. Comparison between charging Mode 1 and Mode 2.

From the measures, it is possible to see the LLC frequency “touching” the legal limit around 230 kHz. Also, a variability of the conducted emissions has been highlighted suspecting a problem on the shield. Indeed, the use of electroplating coating deposition relies on a non-uniform thickness of the coating itself due to a non-uniformity of the current during the process. Electroless solutions have also been tested showing bad results. Electroless plating ensures a uniform plating deposition, but it is a technique where the plating is deposited through chemicals and in the case of nickel plating phosphorous is used to manage the reaction. Phosphorous deposit detrimentally reduces the magnetic permeability of the coating, being non-magnetic if its percentage is higher than 8-10%.

Measurements discrepancies suggest that compliance problem is not completely related to ESA but is intrinsically linked with the set-up. Even more, using different AC cables, a correlation between electromagnetic noise and cable length was highlighted. In fact, as reported in Figure 53, using a 3.2 m length cable electromagnetic noise at 240 kHz drops by 8 dBµV.

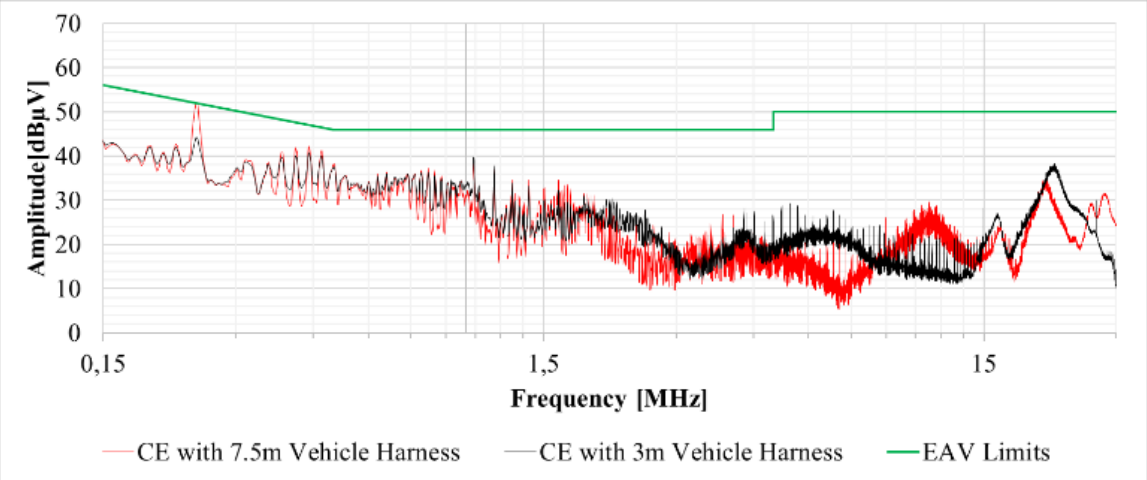

Figure 53: Effect of the length of the AC cable on Conducted Emission on Main lines.

From measurements it is possible to empirically calculate the electromagnetic noise per unit length related to cable length:

$$N_{p.u.l}=\frac{N_{MODE2}(l)-N_{MODE1}}{l}\left[\frac{\text{dBµV}}{\text{m}}\right]$$

Where N_{MODE1} is the electromagnetic noise level measured with MODE 1, independent of cable length (l); N_{MODE2} is the electromagnetic noise level measured with MODE 2 that is length dependent. Table 8 reports the electromagnetic noise per unit length calculated at 240 kHz from the measurements reported in Figure 53.

Table 8: Electromagnetic noise comparison between Charging Mode 1 and 2.

$\mathbf{N_{MODE1}}$ [**dBµV**]	$\mathbf{N_{MODE2}}$ [**dBµV**]	$\mathbf{\Delta N_{7.5\ m}}$ **[dBµV]**	**Cable length [m]**	$\mathbf{N_{p.u.l.}}\left[\frac{\mathbf{dB\mu V}}{\mathbf{m}}\right]$
38	52	14	7.5	1.87

For l =3.2 m, knowing $N_{p.u.l.}$, delta noise value can be calculated as

$$\Delta N_{3.2\ m} = l \cdot N_{p.u.l.} = 5.98 \text{ [dBµV]}$$

N_{MODE2} can be calculated as

$$N_{MODE2} = N_{MODE1} + \Delta N_{3.2\ m} = 43.98 \text{ [dBµV]}$$

close to measured value 44.38 dBµV.

Since the electromagnetic noise increases if the length of the cable increases, the Proxy Pilot signal can be excluded as the source of the coupling. Indeed, PP propagates through the AC harness from the OBC to the vehicle socket which is 1 m long. Instead, the CP line link the OBC with the EVSE throughout the AC harness. The electromagnetic noise coupling path can be re-defined as reported in Figure 54, where the CP filter circuitry is reported as the standard requires.

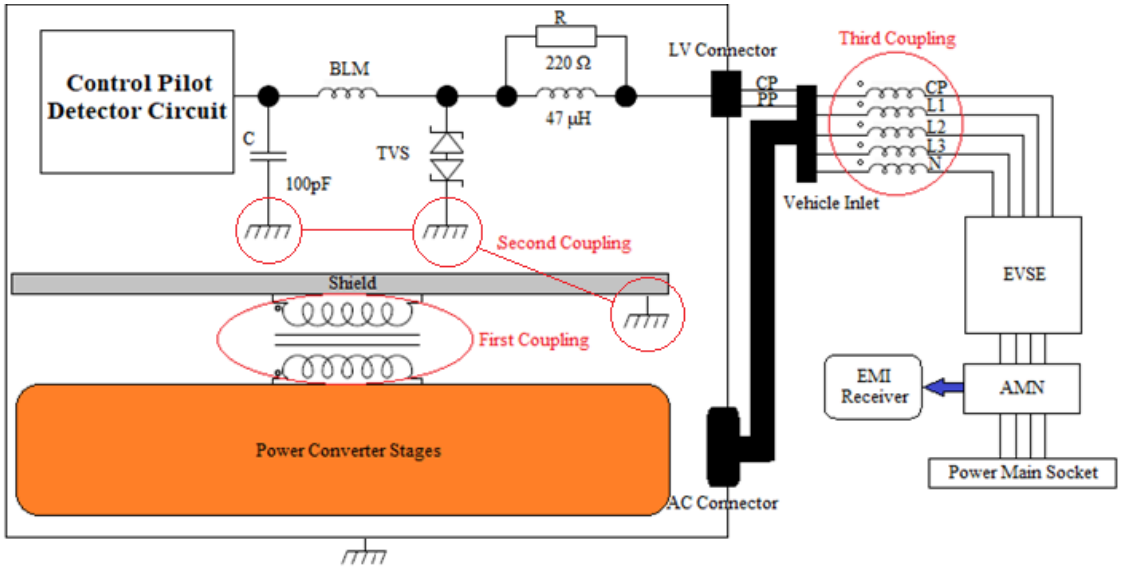

Figure 54: Block scheme of the identification of the coupling mechanism between CP and Main lines.

Three main coupling mechanisms are reported: one from the LLC to the LV board, managed partially by the shield. The second that involves the CP circuitry where filter and protection parts are connected to earth, so connected with the shield itself. The third is related to the presence of the CP on the AC harness.

Since the first coupling path has been studied by Camarda et. Al. focus falls on the second and third coupling paths. Since second and third are strictly linked, the analysis has been splitted in two: firstly, the analysis of the impedance of the CP lines has been evaluated through simulation as well as the AC harness through Ansys Circuit Design and Q2D; secondary, the simulations have been validated through VNA characterization. The results of the simulated and measured CP impedance with respect to earth is reported in Figure 55.

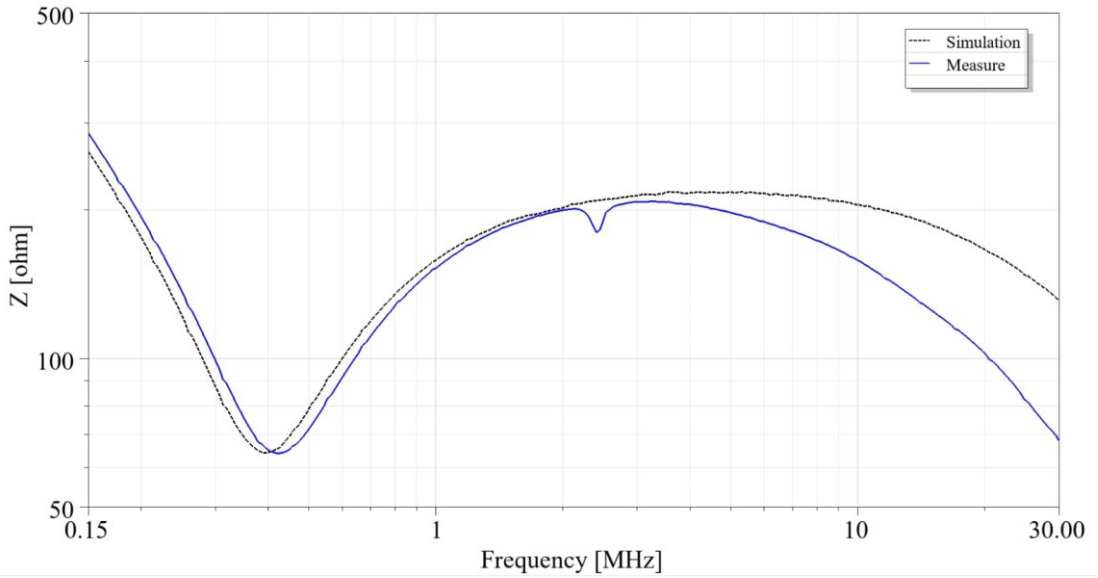

Figure 55: Comparison between CP impedance (respect to earth) measured and modeled by schematic circuit.

Results highlight a drop of impedance around 400 kHz, mismatch of the curves at higher frequency is related to the simplified circuit version using ideal component and the touchstone file of the PCB traces calculated through SIWave ANSYS tool. Despite the mismatch at high frequency, a lack of impedance could justify the amount of electromagnetic noise carried out by the CP, since the electromagnetic noise sees a low impedance path.

Since the CP impedance has been characterized, AC harness cross-section has been replicated through Ansys Q2D, reported in Figure 56, and the coupling between CP and each line has been simulated considering 7.5 m length. The obtained S21, at 230 kHz, parameters are reported in the Table 9 compared with the VNA characterization, showing a good matching between them.

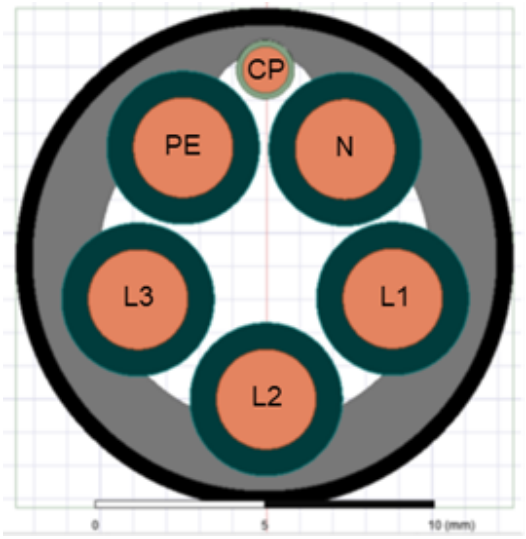

Figure 56: Main line cable cross-section modeled with ANSYS Q2D.

Table 9: Coupling coefficient comparison (S_{21}) between each line and CP.

S21	Simulation [dB]	Measurement [dB]
$S_{21}(CP, L1)$	-35.16	-35.10
$S_{21}(CP, L2)$	-38.04	-38.05
$S_{21}(CP, L3)$	-39.24	-38.94
$S_{21}(CP, N)$	-28.11	-28.83

Since the CP is the main problem and the main circuit on the CP is standardized, the main cause of the lack of impedance is the TVS. As a matter of fact, TVS diodes present a parasitic capacitance that is not negligible, in this case equal to 3.2 nF; TVS impedance has been characterized and reported in Figure 57.

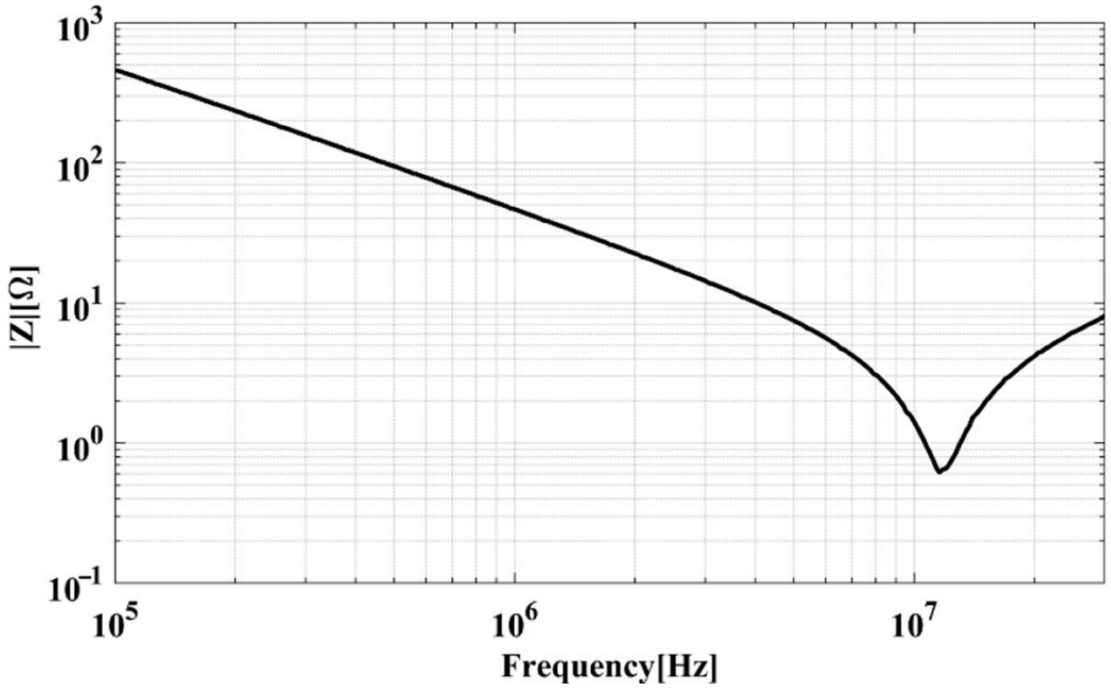

Figure 57: TVS diode impedance without bias voltage applied,[8].

To confirm the hypothesis, the analysis of the CP circuit without the TVS has been conducted: the results, reported in Figure 58, show how the lack of impedance around 400 kHz is no more present when the TVS is not mounted.

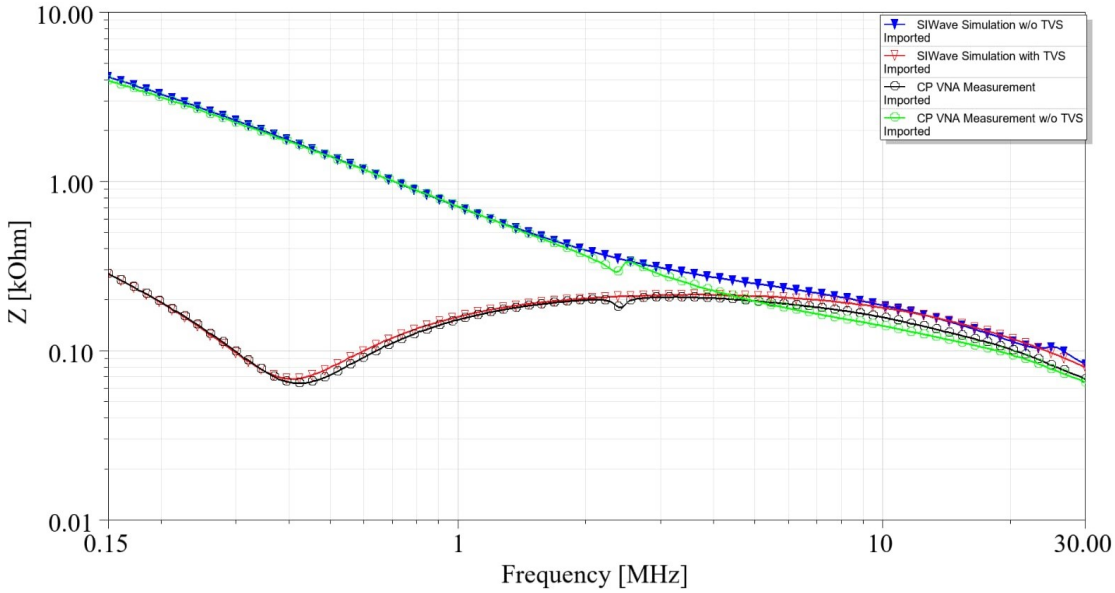

Figure 58: Effect of the TVS diode on the CP line impedance. VNA measures compared with simulation performed considering PCB effects extracted through SIwave.

Since parasitic capacitance is the main problem, a new TVS diode has been selected; indeed, TVS diode must be used since ESD events can occur and the CP line must be protected against them. From an OBC point of view, immunity against ESD is tested reaching values up to 12 kV. New TVS diode selected present a parasitic capacitance of 100 pF.

Repeating the conducted emission on main lines with the new TVS, a reduction of the electromagnetic noise at 240 kHz of 6 dBµV has been highlighted, thus reaching compliance. The comparison between old and new TVS is reported in Figure 59.

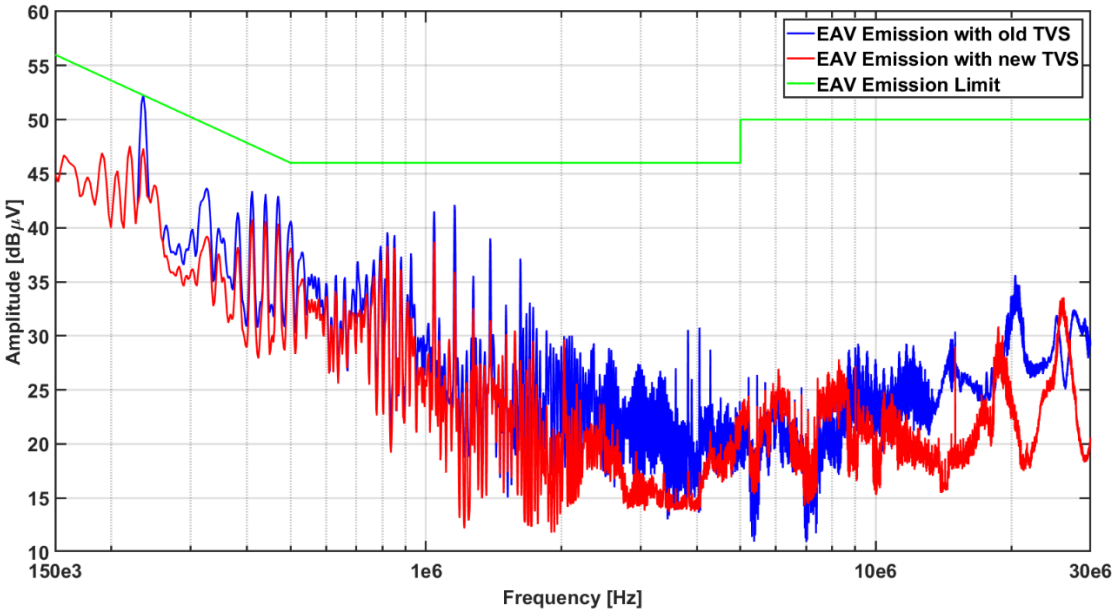

Figure 59: Conducted Emission measure on Main Line, comparison with old TVS and new TVS with reduced parasitic capacitance in Charging Mode 2.

Bibliography

[1] Md. T. Shahed and A. B. M. H. Rashid, 'Battery charging technologies and standards for electric vehicles: A state-of-the-art review, challenges, and future research prospects', *Energy Rep.*, vol. 11, pp. 5978–5998, Jun. 2024, doi: 10.1016/j.egyr.2024.05.062.

[2] UN/ECE, 'ECE R10 Rev.6: Concerning the Adoption of Harmonized Technical United Nations Regulations for Wheeled Vehicles Equipment and Parts which can be Fitted and/or be Used on Wheeled Vehicles and the Conditions for Reciprocal Recognition of Approvals Granted on the Basis of these United Nations Regulations'. 2019.

[3] I. E. Commission, *Electric vehicle conductive charging system. Part 1, General requirements*. International Electrotechnical Commission, 2017.

[4] P. Dini, S. Saponara, and A. Colicelli, 'Overview on Battery Charging Systems for Electric Vehicles', *Electronics (Switzerland)*, vol. 12, no. 20. Multidisciplinary Digital Publishing Institute (MDPI), Oct. 2023. doi: 10.3390/electronics12204295.

[5] M. Yilmaz and P. T. Krein, 'Review of Charging Power Levels and Infrastructure for Plug-In Electric and Hybrid Vehicles'.

[6] *IEC-61851-1:Electric vehicle conductive charging system – Part 1: General requirements*.

[7] 'Charging Modes'. Deltrix. [Online]. Available: https://deltrixchargers.com/about-emobility/charging-modes/

[8] S. Righi, L. Dossi, A. Tacchini, A. Camarda, and L. Vincetti, 'Overview about E-Mobility Conducted Immunity Tests on ESA Communication Lines', *Electronics*, vol. 12, no. 8, p. 1850, Apr. 2023, doi: 10.3390/electronics12081850.

[9] S. Yin, K. J. Tseng, C. F. Tong, R. Simanjorang, C. J. Gajanayake, and A. K. Gupta, 'A 99% efficiency SiC three-phase inverter using synchronous rectification', in *2016 IEEE Applied Power Electronics Conference and Exposition (APEC)*, Long Beach, CA, USA: IEEE, Mar. 2016, pp. 2942–2949. doi: 10.1109/APEC.2016.7468281.

[10] Z. Ye, A. Aguilar, Y. Bolurian, and B. Daugherty, 'GaN FET-Based High CCM Totem-Pole Bridgeless PFC'.

[11] University of Texas at Austin and Q. Huang, 'Review of GaN Totem-Pole Bridgeless PFC', *CPSS Trans. Power Electron. Appl.*, vol. 2, no. 3, pp. 187–196, Sep. 2017, doi: 10.24295/CPSSTPEA.2017.00018.

[12] H. Ademane, R. Attanasio, and G. Vitale, 'A GaN based Totem Pole Bridgeless Power Factor Correction Circuit', in *2024 IEEE Applied Power Electronics Conference and Exposition (APEC)*, Long Beach, CA, USA: IEEE, Feb. 2024, pp. 1968–1972. doi: 10.1109/APEC48139.2024.10509129.

[13] '98.6% Efficiency, 6.6-kW Totem-Pole PFC Reference Design for HEV/EV Onboard Charger'. Texas Instruments.

[14] A. Vetrivelan, Z. Chen, Q. Huang, E. Persson, and A. Q. Huang, 'Design and Implementation of A 5kW 99.2% Efficient High-Density GaN-based Totem Pole Interleaved Bridgeless Bidirectional PFC', in *2021 IEEE Applied Power Electronics Conference and Exposition (APEC)*, Phoenix, AZ, USA: IEEE, Jun. 2021, pp. 1843–1847. doi: 10.1109/APEC42165.2021.9487295.

[15] R. Selders, 'Synchronous rectification in high–performance power converter design'.

[16] X. Gong, G. Wang, and M. Bhardwaj, '6.6kW Three-Phase Interleaved Totem Pole PFC Design with 98.9% Peak Efficiency for HEV/EV Onboard Charger', in *2019 IEEE Applied Power Electronics Conference and*

Exposition (APEC), Anaheim, CA, USA: IEEE, Mar. 2019, pp. 2029–2034. doi: 10.1109/APEC.2019.8722110.

[17] J. Shahsevani and R. Beiranvand, 'Application-Oriented Review of the LLC-Based Resonant Converters', *IEEE Access*, vol. 12, pp. 52687–52726, 2024, doi: 10.1109/ACCESS.2024.3386430.

[18] J. Zeng, G. Zhang, S. S. Yu, B. Zhang, and Y. Zhang, 'LLC resonant converter topologies and industrial applications — A review', *Chin. J. Electr. Eng.*, vol. 6, no. 3, pp. 73–84, Sep. 2020, doi: 10.23919/CJEE.2020.000021.

[19] S. Abdel-Rahman, 'Resonant LLC Converter: Operation and Design', 2012.

[20] P. Rathod, N. Ishraq, A. Chandwani, and A. Mallik, 'Comprehensive Mathematical Modelling and Design of DM EMI Filter for Totem-pole PFC Converter', in *2022 IEEE 1st Industrial Electronics Society Annual On-Line Conference (ONCON)*, kharagpur, India: IEEE, Dec. 2022, pp. 1–6. doi: 10.1109/ONCON56984.2022.10126532.

[21] R. Monteiro, B. Borges, and V. Anunciada, 'EMI reduction by optimizing the output voltage rise time and fail time in high-frequency soft-switching converters', in *2004 IEEE 35th Annual Power Electronics Specialists Conference (IEEE Cat. No.04CH37551)*, Aachen, Germany: IEEE, 2004, pp. 1127–1132. doi: 10.1109/PESC.2004.1355579.

[22] Z. Wang, S. Wang, P. Kong, and F. C. Lee, 'DM EMI noise analysis for critical conduction mode PFC', in *2011 Twenty-Sixth Annual IEEE Applied Power Electronics Conference and Exposition (APEC)*, Fort Worth, TX, USA: IEEE, Mar. 2011, pp. 1475–1481. doi: 10.1109/APEC.2011.5744787.

[23] Ishtiyaq Ahmed Makda, M. Nymand, and U. K. Madawala, 'Common mode noise modeling and its suppression in ultra-high efficiency full bridge boost converter', in *IECON 2013 - 39th Annual Conference of the IEEE Industrial Electronics Society*, Vienna, Austria: IEEE, Nov. 2013, pp. 526–531. doi: 10.1109/IECON.2013.6699190.

[24] Haoyi Ye, Zhihui Yang, Jingya Dai, Chao Yan, Xiaoni Xin, and Jianping Ying, 'Common mode noise modeling and analysis of dual boost PFC circuit', in *2004 10th International Workshop on Computational Electronics (IEEE Cat. No.04EX915)*, Chicago, IL, USA: IEEE, 2004, pp. 575–582. doi: 10.1109/INTLEC.2004.1401526.

[25] F. Jin, A. Nabih, and Q. Li, 'Shielding Technique of Planar Transformers to Suppress Common-Mode EMI Noise for LLC Converter with Full Bridge Rectifier', in *2023 IEEE Applied Power Electronics Conference and Exposition (APEC)*, Orlando, FL, USA: IEEE, Mar. 2023, pp. 1753–1760. doi: 10.1109/APEC43580.2023.10131601.

[26] B. He, Y. Chen, X. Yu, and Y.-F. Liu, 'Common-Mode Noise Reduction in Full-Bridge LLC Resonant Converter with Split Primary Winding Transformer', in *2024 IEEE Applied Power Electronics Conference and Exposition (APEC)*, Long Beach, CA, USA: IEEE, Feb. 2024, pp. 2522–2529. doi: 10.1109/APEC48139.2024.10509045.

[27] Y. Yang, D. Huang, F. C. Lee, and Q. Li, 'Analysis and reduction of common mode EMI noise for resonant converters', in *2014 IEEE Applied Power Electronics Conference and Exposition - APEC 2014*, Fort Worth, TX, USA: IEEE, Mar. 2014, pp. 566–571. doi: 10.1109/APEC.2014.6803365.

[28] Dianbo Fu, P. Kong, S. Wang, F. C. Lee, and Ming Xu, 'Analysis and suppression of conducted EMI emissions for front-end LLC resonant DC/DC converters', in *2008 IEEE Power Electronics Specialists Conference*, Rhodes, Greece: IEEE, Jun. 2008, pp. 1144–1150. doi: 10.1109/PESC.2008.4592084.

[29] P. Curtis and E. Lee, 'EMI Reduction Technique, Dual Random Spread Spectrum', 2020.

[30] J. Song, C.-Y. Chu, Y. Lee, D.-I. Lee, H.-S. Youn, and K.-B. Park, 'Parameter Optimization of Spread Spectrum Modulation to Minimize EMI Filter for Interleaved Totem-Pole PFC Converters', in *2023 11th International Conference on Power Electronics and ECCE Asia (ICPE 2023*

- *ECCE Asia)*, Jeju Island, Korea, Republic of: IEEE, May 2023, pp. 1423–1429. doi: 10.23919/ICPE2023-ECCEAsia54778.2023.10213906.

[31] Y. Wenrong, Z. Haojie, H. Tianchen, L. Junling, Q. Yiwei, and C. Guohang, 'Research on EMI and ripple suppression of LLC Resonant Converter based on symmetric chaotic spread spectrum', in *2022 Asia-Pacific International Symposium on Electromagnetic Compatibility (APEMC)*, Beijing, China: IEEE, Sep. 2022, pp. 296–298. doi: 10.1109/APEMC53576.2022.9888734.

[32] Z. Zhang and A. M. Bazzi, 'Modeling, Design, and Implementation of a Novel Transformer-less Feedforward-controlled Active EMI Filter for AC-DC Power Converters', *ECCE 2020 - IEEE Energy Convers. Congr. Expo.*, pp. 5849–5854, Oct. 2020, doi: 10.1109/ECCE44975.2020.9236198.

[33] B. Narayanasamy, F. Luo, and Y. Chu, 'Modeling and Stability Analysis of Voltage Sensing based Differential Mode Active EMI Filters for AC-DC Power Converters', *2018 IEEE Symp. Electromagn. Compat. Signal Integr. Power Integr. EMC SI PI 2018*, Oct. 2018, doi: 10.1109/EMCSI.2018.8495239.

[34] S. Haensel, J. T. Friedrich-Alexander, and S. Frei, 'Modeling and Stability Analysis of Voltage Sense Current Cancellation Active EMI Filter'.

[35] S. Wang, Y. Y. Maillet, F. Wang, and D. Boroyevich, 'Hybrid EMI filter design for common mode EMI suppression in a motor drive system', *PESC Rec. - IEEE Annu. Power Electron. Spec. Conf.*, pp. 181–187, 2008, doi: 10.1109/PESC.2008.4591922.

[36] Y. Han, Z. Wu, and D. Wu, 'Hybrid Common-mode EMI Filter Design for Electric Vehicle Traction Inverters', *Chin. J. Electr. Eng.*, vol. 8, no. 4, pp. 52–60, Dec. 2022, doi: 10.23919/CJEE.2022.000038.

[37] J. Schmenger, R. Kramer, and M. März, 'Active Hybrid Common Mode Filter for a Highly Integrated On-board Charger for Automotive Applications'.

[38] P. S. Niklaus, 'Design and Experimental Analysis of a Three-Phase Active CM/DM Conducted EMI Noise Separator', *CPSS Trans. Power Electron.*

Appl., vol. 5, no. 3, pp. 273–288, Sep. 2020, doi: 10.24295/CPSSTPEA.2020.00023.

[39] Y. Chu, S. Wang, and Q. Wang, 'Active EMI filters to reduce size and cost of EMI filters in automotive systems', *IEEE Trans. Power Electron.*, vol. 31, no. 9, pp. 6254–6263, Sep. 2016, doi: 10.1109/TPEL.2015.2502218.

[40] T. Hegarty, 'How Active EMI Filter ICs Mitigate Common-Mode Emissions and Increase Power Density in Single- and Three-Phase Power Systems', 2023.

[41] Y. Zhou, Y. Jin, H. Xu, H. Luo, W. Li, and X. He, 'Heterogeneous Integration of Silicon-Based *RC* Snubber in SiC Power Module for Parasitic Oscillation Noise Reduction', *IEEE Trans. Power Electron.*, vol. 38, no. 6, pp. 6902–6906, Jun. 2023, doi: 10.1109/TPEL.2023.3249798.

[42] X. Yang, M. Xu, Q. Li, Z. Wang, and M. He, 'Analytical Method for *RC* Snubber Optimization Design to Eliminate Switching Oscillations of SiC MOSFET', *IEEE Trans. Power Electron.*, vol. 37, no. 4, pp. 4672–4684, Apr. 2022, doi: 10.1109/TPEL.2021.3127516.

[43] W. Ma, Y. Wu, H. Li, and D. Chu, 'Investigation of the Gate Resistance and the RC snubbers on the EMI Suppression in Applying of the SiC MOSFET', in *2019 IEEE International Conference on Mechatronics and Automation (ICMA)*, Tianjin, China: IEEE, Aug. 2019, pp. 2224–2228. doi: 10.1109/ICMA.2019.8816376.

[44] J. Ji, W. Chen, X. Yang, X. Zhang, and N. Zhi, 'A layout method of passive EMI filter', in *2017 IEEE Energy Conversion Congress and Exposition (ECCE)*, Cincinnati, OH: IEEE, Oct. 2017, pp. 2346–2349. doi: 10.1109/ECCE.2017.8096455.

[45] Xiaoning Ye, Geping Liu, and J. L. Drewniak, 'Investigation of PCB layout parasitics in EMI filtering of I/O lines', in *2001 IEEE EMC International Symposium. Symposium Record. International Symposium on Electromagnetic Compatibility (Cat. No.01CH37161)*, Montreal, Que., Canada: IEEE, 2001, pp. 501–504. doi: 10.1109/ISEMC.2001.950692.

[46] M. Ali, J. Friebe, and A. Mertens, 'Design and Optimization of Input and Output EMI Filters under the Influence of Parasitic Couplings', in *2021 23rd European Conference on Power Electronics and Applications (EPE'21 ECCE Europe)*, Ghent, Belgium: IEEE, Sep. 2021, pp. 1–10. doi: 10.23919/EPE21ECCEEurope50061.2021.9570483.

[47] A. Asmanis, G. Asmanis, D. Stepins, and L. Ribickis, 'Modeling of EMI filters with shields placed between the filter components', in *2016 International Symposium on Electromagnetic Compatibility - EMC EUROPE*, Wroclaw, Poland: IEEE, Sep. 2016, pp. 776–779. doi: 10.1109/EMCEurope.2016.7739252.

[48] M. Ali, R. Bushra, J. Friebe, and A. Mertens, 'Improvement of EMI Filter Attenuation Using Shielding'.

[49] M. Ozkok, S. Lamprecht, E. Klusmann, and H. Hubner, 'Adjustable EMI Shielding on Electronic Packages Realized by Electrolytic Plating', in *2019 IEEE CPMT Symposium Japan (ICSJ)*, Kyoto, Japan: IEEE, Nov. 2019, pp. 191–194. doi: 10.1109/ICSJ47124.2019.8998721.

[50] K. Joo *et al.*, 'Evaluation of package-level EMI shielding using conformally coated conductive and magnetic materials in low and high frequency ranges', in *Proceedings - Electronic Components and Technology Conference*, Institute of Electrical and Electronics Engineers Inc., Jun. 2020, pp. 647–652. doi: 10.1109/ECTC32862.2020.00107.

[51] Y.-H. Kim *et al.*, 'The Highly Effective EMI Shielding Materials for Electric and Magnetic Fields Over the Wide Range of Frequency in Near-Field Region', in *2019 IEEE 69th Electronic Components and Technology Conference (ECTC)*, Las Vegas, NV, USA: IEEE, May 2019, pp. 733–739. doi: 10.1109/ECTC.2019.00116.

[52] A. Camarda, F. Calvano, A. M. Khan, M. Balbarani, P. Montanari, and D. Grossi, 'Computer Aided Engineering for optimal EMC design of On-Board Battery Chargers', in *Proceedings of the 2020 International Symposium on Electromagnetic Compatibility - EMC EUROPE : virtual conference, September 23-25, 2020*, IEEE, 2020.

[53] *CISPR25 - Vehicles, boats and internal combustion engines - Radio disturbance characteristics - Limits and methods of measurement for the protection of on-board receivers*, Geneva., 2021.

[54] 'S-parameters for High-frequency Circuit Simulations'. [Online]. Available: https://www.coilcraft.com/getmedia/35dbfd16-8483-4ef7-bb07-9b28a04f6dcc/doc1721_when-to-use-s-parameters.pdf

[55] E. Bogatin, 'S-Parameters for High Speed Digital Engineers: A Beginner's Guide', *IEEE Electromagn. Compat. Mag.*, vol. 12, no. 1, pp. 34–41, 2023, doi: 10.1109/MEMC.2023.10134760.

[56] M. Beley, L. Pace, and A. Bréard, 'An accurate characterization method of passive components for Very High Frequency power conversion applications', in *2024 Energy Conversion Congress & Expo Europe (ECCE Europe)*, Darmstadt, Germany: IEEE, Sep. 2024, pp. 1–8. doi: 10.1109/ECCEEurope62508.2024.10751881.

[57] J. Bacmaga, H. Stimac, and A. Baric, 'Combined Series and Shunt Characterization for Accurate Resonant Frequency Extraction and Circuit Modelling of Surface-Mount Inductors', in *2020 IEEE 24th Workshop on Signal and Power Integrity (SPI)*, Cologne, Germany: IEEE, May 2020, pp. 1–4. doi: 10.1109/SPI48784.2020.9218212.

[58] M. Bosi, A. Miquel Sánchez, F. Javier Pajares, and L. Peretto, 'Three-Phase Modal Noise Analysis and Optimal Three-Phase Power Line Filter Design', *Energies*, vol. 16, no. 14, p. 5461, Jul. 2023, doi: 10.3390/en16145461.

[59] V. Tarateeraseth, 'EMI filter design: Part III: Selection of filter topology for optimal performance', *IEEE Electromagn. Compat. Mag.*, vol. 1, no. 2, pp. 60–73, 2012, doi: 10.1109/MEMC.2012.6244975.

[60] V. Tarateeraseth, 'EMI filter design: Part II: Measurement of noise source impedances', *IEEE Electromagn. Compat. Mag.*, vol. 1, no. 1, pp. 42–49, 2012, doi: 10.1109/MEMC.2012.6244944.

[61] E. Mazzola, F. Grassi, and A. Amaducci, 'Measuring the Noise Impedances of Switched-Mode Power Supplies', in *2019 IEEE International*

Symposium on Electromagnetic Compatibility, Signal & Power Integrity (EMC+SIPI), New Orleans, LA, USA: IEEE, Jul. 2019, pp. 1–6. doi: 10.1109/ISEMC.2019.8825193.

[62] C. Cuellar, N. Idir, A. Benabou, and X. Margueron, 'High frequency current probes for common-mode impedance measurements of power converters under operating conditions', in *2013 15th European Conference on Power Electronics and Applications (EPE)*, Lille, France: IEEE, Sep. 2013, pp. 1–8. doi: 10.1109/EPE.2013.6631983.

[63] K. Y. See and J. Deng, 'Measurement of Noise Source Impedance of SMPS Using a Two Probes Approach', *IEEE Trans. Power Electron.*, vol. 19, no. 3, pp. 862–868, May 2004, doi: 10.1109/TPEL.2004.826520.

[64] *ISO 17409 - Electrically propelled road vehicles - Conductive power transfer - Safety requirements:*, 2020. doi: 10.3403/30359452.

[65] 'Vishay Safety Capacitors: Film, Ceramic Single Disc, and MLCC Technologies and Key Features'. Vishay, Jan. 03, 2020. [Online]. Available: https://www.vishay.com/docs/45023/vishaysafetycapacitors.pdf

[66] A. Camarda *et al.*, 'Broadband Circuit Model of Common Mode Chokes for EMI pre-compliance assessment'.

[67] M. Kovacic, Z. Hanic, S. Stipetic, S. Krishnamurthy, and D. Zarko, 'Analytical wideband model of a common-mode choke', *IEEE Trans. Power Electron.*, vol. 27, no. 7, pp. 3173–3185, 2012, doi: 10.1109/TPEL.2011.2182060.

[68] A. Roc', *Behavioural Models for Common Mode EMI Filters*. 2012.

[69] N. Moonen, R. Vogt-Ardatjew, A. Roc'h, and F. Leferink, '3-D Full-Wave High Frequency Common Mode Choke Modeling', *IEEE Trans. Electromagn. Compat.*, vol. 62, no. 3, pp. 707–714, Jun. 2020, doi: 10.1109/TEMC.2019.2914371.

[70] I. Stevanović, S. Skibin, M. Masti, and M. Laitinen, 'Behavioral modeling of chokes for EMI simulations in power electronics', *IEEE Trans. Power Electron.*, vol. 28, no. 2, pp. 695–705, 2013, doi: 10.1109/TPEL.2012.2203319.

[71] C. Cuellar, W. Tan, X. Margueron, A. Benabou, and N. Idir, 'Measurement method of the complex magnetic permeability of ferrites in high frequency', in *2012 IEEE International Instrumentation and Measurement Technology Conference Proceedings*, Graz, Austria: IEEE, May 2012, pp. 63–68. doi: 10.1109/I2MTC.2012.6229697.

[72] 'Metallized Polypropylene DC-Link Film Capacitor'. Vishay. [Online]. Available: https://www.vishay.com/docs/28164/mkp1848dcl.pdf

[73] 'Interference Suppression Film Capacitor - Class Y2 Radial MKP 300 VAC - Line to Ground Application'. Vishay. [Online]. Available: https://www.mouser.it/datasheet/2/427/mkp3386y2-239692.pdf

[74] T. D. Oliveira, J.-M. Guichon, J.-L. Schanen, and L. Gerbaud, 'PEEC-models for EMC filter layout optimization', 2010.

[75] T. De Oliveira, J.-L. Schanen, J.-M. Guichon, and L. Gerbaud, 'Automatic layout optimization of an EMC filter', in *2010 IEEE Energy Conversion Congress and Exposition*, Atlanta, GA: IEEE, Sep. 2010, pp. 2679–2685. doi: 10.1109/ECCE.2010.5618037.

[76] A. Camarda, M. Balbarani, F. Calvano, S. Righi, L. Dossi, and A. Tacchini, 'Characterization of High Voltage EMC filters for Electric Vehicles charging applications', in *IEEE International Symposium on Electromagnetic Compatibility*, Institute of Electrical and Electronics Engineers Inc., 2023. doi: 10.1109/EMCEurope57790.2023.10274242.

[77] I. F. Kovacevic, T. Friedli, A. Musing, and J. W. Kolar, 'PEEC-based virtual design of EMI input filters', in *2011 IEEE Energy Conversion Congress and Exposition*, Phoenix, AZ, USA: IEEE, Sep. 2011, pp. 1935–1941. doi: 10.1109/ECCE.2011.6064023.

[78] A. Govindankutty *et al.*, 'On the Methodology of Modeling a Parallel Plate Capacitor Using the Partial Element Equivalent Circuit (PEEC) Technique', in *2023 IEEE Research and Applications of Photonics in Defense Conference, RAPID 2023 - Proceedings*, Institute of Electrical and Electronics Engineers Inc., 2023. doi: 10.1109/RAPID54473.2023.10264711.

[79] G. Antonini, M. Sabatini, and G. Miscione, 'PEEC modeling of linear magnetic materials', *IEEE Int. Symp. Electromagn. Compat.*, vol. 1, pp. 93–98, 2006, doi: 10.1109/ISEMC.2006.1706270.

[80] G. Chiqovani, D. Imnadze, A. Demurov, A. Gheonjian, D. Eremyan, and R. Jobava, 'PEEC Solution of EM-Circuit Problems for Combined Metalic and Dielectric Structures Based on the Augmented Integral Equations'.

[81] K. Takahashi, Y. Murata, Y. Tsubaki, T. Fujiwara, H. Maniwa, and N. Uehara, 'Simulation of shielding performance against near field coupling to EMI filter for power electronic converter using FEM', in *2016 International Symposium on Electromagnetic Compatibility - EMC EUROPE*, Wroclaw, Poland: IEEE, Sep. 2016, pp. 716–721. doi: 10.1109/EMCEurope.2016.7739152.

[82] M. Kazimierczuk, *High-Frequency Magnetic Components*, 1st ed. Wiley, 2013. doi: 10.1002/9781118717806.

[83] ANSYS, 'Ansys Launches HFSS Mesh Fusion, Redefines Product Development by Enabling Design of Entire Systems'. [Online]. Available: https://www.ansys.com/news-center/press-releases/01-21-21-ansyslaunches- hfss-mesh-fusion-redefines-product-development-byenabling- design-of-entire-systems.